University of Strathclyde

Department of Electronic and Electrical Engineering

Design and Control of Multiport Isolated DC-DC Converter for Hydrogen Energy Systems

PhD Thesis

Oyedotun E. Oyewole

A thesis submitted in fulfilment of the requirements for the degree of Doctor of Philosophy

November 2025

Copyright

This thesis is the result of the author's original research. It has been composed by the author and has not been previously submitted for examination which has led to the award of a degree.

The copyright of this thesis belongs to the author under the terms of the United Kingdom Copyright Acts as qualified by the University of Strathclyde Regulation 3.50. Due acknowledgement must always be made of the use of any material contained in, or derived from, this thesis.

Signed: *Oyedotun E. Oyewole*

Date: 19/11/2025

Acknowledgments

This has been a journey that demanded every effort, a path marked by highs and lows, and an undertaking filled with both pleasant and challenging surprises. The guidance and tutelage of my supervisor, Prof. Khaled Ahmed, cannot be overemphasised. I am grateful for the constant encouragement, support and valuable insights he provided, which have been vital in shaping this work.

I am also grateful to the Power Electronics, Drives, and Energy Conversion research group at the University of Strathclyde, in particular Prof. Lie Xu, Prof. Agustí Egea and my colleagues Irene Messange, Tesfu Gebremedhin, Dr. Sam Harrison, Mohamed Abouyehia and Oswin Ashwood. I deeply appreciate the insightful discussions during the monthly group meetings. I would like to acknowledge and sincerely appreciate the efforts and assistance of my dear friends Dr. Ali Abdelaziz, Dr. Yousef Abdelaziz and Dr. Isah Jimoh.

My family has always been there for me through thick and thin. Although my parents could not witness this day, they laid a solid foundation for the person I have become. My sisters have always been supportive, and I am grateful for the gift of each of them, Oyetayo Adetunji, Oluwaseun Banye and Tolulope Oladejo. To my wife, Temitope Oyewole, you have just earned a PhD by proxy. Thank you for your love and unwavering support.

I would like to express my sincere appreciation to the Petroleum Technology Development Fund (PTDF) of the Federal Republic of Nigeria for their generous support toward the completion of this programme. I am truly grateful.

Finally, “It is not of him who wills, nor of him who runs, but of Him who shows mercy”. The all-knowing and all-loving God has clearly shown me mercy, and I am grateful to be called His own.

Abstract

Hydrogen energy storage systems (HESS) are vital for sustainable energy, and their performance is heavily influenced by their power electronics converter (PEC) interfaces. Conventional PEC interfaces, which use individually operating converters, often lead to bulky systems with multiple conversion stages and increased circulating currents, resulting in higher losses. This thesis addresses these shortcomings by implementing a multiport-isolated DC-DC converter for HESS, which offers enhanced power density, a reduced component count, and fewer conversion stages. However, this proposed converter introduces its own challenges, primarily the cross-coupling effect caused by the high-frequency multiwinding transformer. This effect results in significant power deviations during step changes, risking hydrogen depletion in fuel cells and instability in electrolysers. Furthermore, the conventional single-phase shift (SPS) modulation used in such converters typically experiences higher circulating currents, reducing overall efficiency.

To mitigate the cross-coupling, the implementation of a decoupling control technique is essential. This study investigates and compares three simple matrix-based decoupling techniques, finding the inverse matrix method to be the best performer, though it still fails to fully decouple the system over a wide operating range. To overcome this limitation, a novel model reference-based decoupling control technique is proposed, which minimises the error between the actual system output and an ideal reference model. This technique is further enhanced into a hybrid decoupling control by integrating a decoupling matrix, ensuring robust performance across a wider operating region by mathematically minimising the cross-coupling term with a proportional-derivative controller. This hybrid technique significantly reduces maximum power deviations compared to the best matrix-based method. Recognizing that these decoupling techniques generally require detailed system knowledge, which complicates implementation due to parameter fluctuations, the thesis also proposes a solution using a linear active disturbance rejection controller (LADRC), which only requires knowledge of the system order. However, as the LADRC is susceptible to estimation errors and requires manual tuning, a particle swarm optimisation (PSO) algorithm is employed to automatically determine the optimal controller gains. This PSO-optimised LADRC effectively suppresses cross-coupling across a wider operating region, performing better than both non-decoupled controllers and a genetic algorithm (GA)-optimised LADRC.

In parallel, to address the efficiency limitations of SPS control, which is limited in its ability to independently regulate inter-port power flow and leads to increased inductor current and circulating power, the thesis also proposes an online adaptive control based on the steepest descent method. This technique dynamically adjusts internal phase shifts in real-time to minimise the error between reference and actual active inter-port power flows under varying conditions, thereby enhancing operational efficiency. A comprehensive mathematical formulation, supported by Lyapunov-based stability analysis, confirms the stability of the adaptive gains in this proposed control. Finally, simulations and experimental validations confirm the effectiveness and robustness of all the proposed control techniques, demonstrating significant improvements in system efficiency and performance across a wider operating region for hydrogen energy storage applications.

List of Abbreviation

ESS	Energy Storage Systems
HESS	Hydrogen Energy Storage Systems
PEC	Power Electronic Converter
CO_2	Carbon dioxide
IRENA	International Renewable Energy Agency
GWEC	The Global Wind Energy Council
CAES	Compressed Air Energy Storage
SMES	Superconducting Magnetic Energy Storage
EL	Electrolyser
FC	Fuel Cell
P2G	Power-to-Gas
LCOH	Levelised Cost of Hydrogen
GHG	Greenhouse Gas
EU	European Union
NO_X	Nitrogen Oxides
DE	Distributed Energy Sources
PEMFC	Proton Exchange Membrane Fuel Cells
SOFC	Solid Oxide Fuel Cells
MCFC	Molten Carbonate Fuel Cells
PAFC	Phosphoric Acid Fuel Cells
AFC	Alkaline Fuel Cells
PEMEL	Proton Exchange Membrane Electrolysers
SOE	Solid Oxide Electrolysers
AEMEL	Anion Exchange Membrane Electrolysers
AEL	Alkaline Electrolysers
SEPIC	Single-Ended Primary Inductor Converter
PWM	Pulse Width Modulation
ZSI	Z-Source Impedance Converters
MISO	Multi-Input Single-Output
CBC	Conventional Buck Converters
QBC	Quadratic Buck Converters
IBC	Interleaved Buck Converters

ISBC	Interleaved Synchronous Buck Converter
SIBC	Stacked Interleaved Buck Converter
EMI	Electromagnetic Interference
VFC	Voltage-Fed Converters
CFC	Current-Fed Converters
SMPS	Switch-Mode Power Supply
PPC	Partial Power Converter
DAB	Dual Active Bridge
RES	Renewable Energy Sources
MIMO	Multiple Input Multiple Output
MPC	Model Predictive Controller
LADRC	Linear Active Disturbance Rejection
SISO	Single-Input, Single-Output
P&O	Perturb-And-Observe
LUT	Look-up Tables
SPS	Single-Phase Shift
DPS	Dual-Phase Shift
TPS	Triple-Phase Shift
PSO	Particle Swarm Optimisation
TAB	Triple Active Bridge
ANN	Artificial Neural Network
EWMA	Exponential Weighted Moving Average
GHA	Generalised Harmonic Approximation
BT	Battery
EMI	Electromagnetic Interference
LESO	Linear Extended State Observers
GA	Genetic Algorithm
NMPC	Non-Linear Model Predictive Control
ML	Marine Loads
PID	Proportional Integral Derivative
DSP	Digital Signal Processor
ADC	Analog Digital Converter

List of Symbols

L_1, L_2', L_3'	Leakage Inductances for 1, 2 and 3 windings of the transformer
u_1, u_2', u_3'	Bridge 1, 2 and 3 bridge midpoint voltages
i_1, i_2', i_3'	Bridge 1, 2 and 3 bridge leakage inductor current
i_{2p}, i_{3p}	Prefiltered output current at port 2 and port 3 respectively
$1: n_2$	Windings 1:2 turns' ratio
$1: n_3$	Windings 1: 3 turns' ratio
$V_{DE}, V_{FC}, V_{EL}, V_{BT}, V_{ML}$	Output voltages of the DE, FC, EL, BT and ML ports respectively
$P_{DE}, P_{FC}, P_{EL}, P_{BT}, P_{ML}$	Active output powers of the DE, FC, EL, BT and ML ports respectively
$I_{DE}, I_{FC}, I_{EL}, I_{BT}, I_{ML}$	Output current flowing towards or outside the DE, FC, EL, BT and ML ports respectively
i_{12}, i_{23}, i_{13}	Current flowing between the 1 to 2 bridge, the current flowing between the 2 to 3 bridge, and the current flowing between the 1 to 3 bridge respectively
P_{12}, P_{23}, P_{13}	Power flowing between 1 to 2 bridge, power flowing between 2 to 3 bridge, and power flowing between 1 to 3 bridge respectively
φ_2	The phase shift between bridge 1 and bridge 2
φ_3	The phase shift between bridge 1 and bridge 3
L_{FC}, C_{FC}	Inductance and capacitance of the LC filter at the FC port
r_{FC}	Lumped FC port parasitic resistance
C_{EL}	Capacitor filter at the EL port
f_{FC}, f_{EL}	Lumped disturbance of both internal dynamics and external disturbance at FC and EL ports respectively
$\beta_1, \beta_2, \beta_3$	Observer gains
w_0	Observer bandwidths
K_p, K_d	Controller gains
w_c	Controller bandwidths
b_0	Critical gain
A_3, B_3, C_3, L_3	First-order state matrices
A_2, B_2, C_2, L_2	Second-order state matrices

V_0	Output voltage
Δi_l	inductor ripple current
Δv_0	Output voltage ripple
R	Resistive load
C	Capacitance
f	Frequency
D	Duty ratio

Table of Contents

Chapter 1

Introduction

For decades, the global power grid has relied heavily on conventional energy sources such as coal, oil, and natural gas (collectively referred to as fossil fuels) to generate electricity, accounting for over 85 % of total primary energy consumption [1]. Although this dependence has driven industrial and societal development, it has resulted in significant environmental and economic drawbacks. According to the Production Gap report, the combustion of these fuels is responsible for approximately 75 % of global greenhouse gas (GHG) emissions and nearly 90 % of all carbon dioxide (CO_2) emissions, substantially contributing to climate change and global warming [2]. Therefore, decarbonising the power system is essential to mitigate the impacts of climate change.

This can be achieved through the deployment of renewable energy (RE) sources, among which wind energy is widely implemented via both onshore and offshore wind farms (OWF). The Global Wind Energy Council (GWEC) reported that the total installed wind power capacity reached 837 GW by the end of 2021, helping the world avoid a total of 1.2 billion tons of CO_2 annually [3]. OWF situated in coastal waters can exploit stronger and more consistent wind speeds than their onshore counterparts. This results in higher capacity factors, often exceeding 50 % [4], and larger turbine sizes, with the current models reaching up to 15 MW per unit [3].

While renewable energy offers economic and environmental benefits, it also poses challenges, mainly due to its intermittent nature. Its output depends heavily on environmental conditions, which vary with time of day and weather. This intermittency can cause energy surpluses or shortages. In favourable conditions, renewables may generate excess energy, leading to curtailment. In unfavourable conditions, output may fall short, requiring backup sources to ensure a stable supply.

To fully harness the potential of REs and ensure a stable, reliable power supply, energy storage solutions (ESS) are essential. Various technologies have been proposed, broadly categorised into mechanical, electromagnetic, and electrochemical storage, as listed in Table 1.1 [5]. Electrochemical storage devices, such as lithium-ion and lead-acid batteries, are widely used owing to their flexibility, scalability, and relatively short deployment times.

Table 1.1: Comparison of energy storage systems [6]

Type	Category	Discharge time	Capacity	Efficiency
HESS	Electrochemical	<1000 h	<1 GW	30 - 45 %
Battery	Electrochemical	<5 h	<100 MW	70 - 85 %
Flywheels	Mechanical	<30 min	<1 MW	85 - 100 %
CAES	Mechanical	<100 h	<10 MW	45 - 70 %
Pumped hydro	Mechanical	<500 h	<0.8 GW	70 - 85 %
SMES	Electromagnetic	< 5 h	<5 MW	85 - 99 %

However, there exists a gap in scalable long duration ESS technologies. Among the electrochemical options, hydrogen energy storage systems (HESS) have gained significant attention for their environmental benefits, scalability, high energy density and large capacity. HESS also offers a long discharge time compared to other electrochemical short-term storage methods (Table 1.1).

Despite the limited overall efficiency of HESS as shown in Table 1.1, compared with other storage technologies, HESS is still viewed as a promising/future energy storage technology due to its long-duration storage capability and its effectiveness in energy sector coupling [7]. Hydrogen can be produced using surplus renewable electricity that might otherwise be curtailed, thereby improving overall system utilisation [8]. It can also be stored for extended periods and transported using dedicated or adapted gas infrastructure [9]. When required, hydrogen may be reconverted into electricity via fuel cells [7]. Hence, hydrogen is widely regarded as a key candidate for future large-scale energy storage systems. With research is ongoing to improve the efficiencies of various elements that makes up the HESS, which is expected to enhance its overall performance.

1.1 Hydrogen: A Long-Term Storage Solution for Multiple Sectors

HESS involve the production of hydrogen via electrolysis, a process that splits water (H_2O) into hydrogen (H_2) and oxygen (O_2) using an electric current. The environmentally friendly nature, scalability, long-duration capability, high energy density, and large storage capacity of HESSs make them a promising solution to mitigate the intermittency of RES, as shown in Table 1.1, an advantage over other ESSs. Literature suggests that HESSs can be powered by RES to produce “green hydrogen.” During favourable periods of renewable energy generation, excess energy can be directed to electrolysers (ELs) to produce green

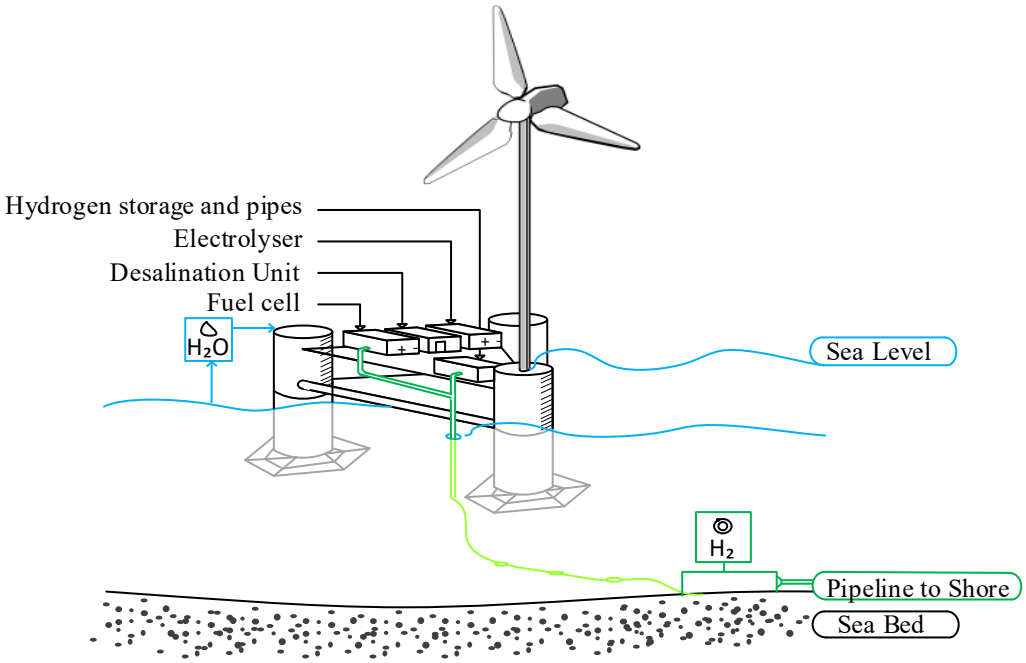

Fig. 1.1. Hydrogen energy storage systems in offshore wind farms.

hydrogen, in a process often referred to as power-to-gas (P2G) technology. In this section, the application of hydrogen as a long-term energy system is discussed.

1.1.1 Offshore Wind farm Hydrogen Energy Storage System

Generating green hydrogen from offshore wind is promising due to rapid development and abundant resources. Since 2020, UK OWF energy generation has surpassed that of onshore, with future projects expected farther offshore, potentially facing limited interconnection points and grid constraints [10]. In such cases, hydrogen production may be prioritised. Offshore wind also has a higher capacity factor than most renewables, allowing EL to operate longer and produce more hydrogen [11]. However, ELs require large amounts of freshwater (up to nine tons per ton of hydrogen) [11], posing challenges in regions with limited freshwater. Desalination units can be installed at offshore wind farms to supply the necessary water for EL operation.

There are different philosophies regarding OWF HESS, which can generally be grouped into three. The first involves onshore hydrogen production via direct connection, where the OWF transmits power through offshore substations and high-voltage cables to shore; however, the high cable cost is a major drawback. The second places the EL offshore, producing hydrogen using desalinated seawater, with hydrogen transport through pipelines being cheaper per kilometer than high-voltage cabling. The third employs a central offshore hydrogen production platform, where power from multiple wind turbines is collected through

Fig. 1.2. Marine Sector Hydrogen Energy System [12].

an array of cables for large-scale hydrogen generation [13]. Among these concepts, the second philosophy, as depicted in Fig. 1.1, appears particularly advantageous, with a lower levelised cost of hydrogen (LCOH).

Several offshore wind farm HESS projects are currently underway across Europe. For instance, the world's largest offshore wind farm, the 1.4 GW Hornsea 2, commissioned in Aug. 2022, is set to be connected to the Gigastack project for green hydrogen production [14]. Another significant initiative is the Dolphyn Hydrogen Project, which aims to achieve a capacity of 4 GW [15].

1.1.2 Hydrogen Energy System in the Marine Sector

The marine sector plays a crucial role in global trade by transporting approximately 90 % of the world's goods [16]. However, it is also a significant contributor to GHG emissions. According to the International Maritime Organization (IMO), the maritime industry is responsible for nearly 3 % of global CO_2 emissions, releasing approximately 940 million metric tons of CO_2 annually [17]. This level of emissions has substantial environmental impacts, including ocean acidification and climate change. By 2050, the IMO aims to reduce CO_2 emissions by at least 50 % compared to the 2008 levels [18]. Achieving these goals requires the adoption of cleaner fuels and advanced propulsion technologies.

Hydrogen is a suitable fuel for marine propulsion and other onboard electrical loads, owing to its clean burning properties and high energy density. It can be stored onboard either through liquid or compressed forms [14]. Hydrogen can then be used in FCs to generate electricity, which powers electric motors for propulsion, as well as other onboard loads.

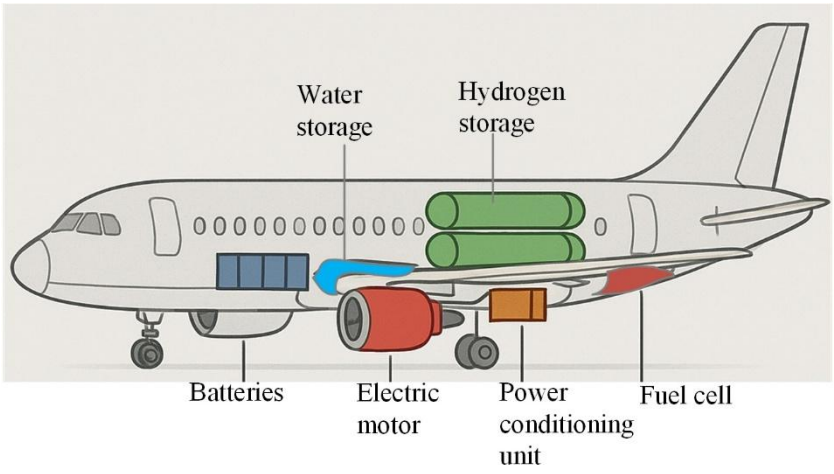

Fig. 1.3: Hydrogen energy system in the aerospace sector [19].

Additionally, the heat generated can be used to heat onboard rooms, and batteries can provide short-term energy storage, as depicted in Fig. 1.2.

Hydrogen-powered FC electric vessels have been developed and tested worldwide. Several projects have been conducted to investigate these applications. An example is the flagship project which uses Ballard FC modules with 1 MW onboard FC power using gaseous and liquid hydrogen [12]. Another project in the UK is the hydrogen-powered vessel Windcat - 57 [20]. These vessels use FCs to convert hydrogen into electricity, which then powers the propulsion system of the ship and other electrical loads.

1.1.3 Hydrogen Energy System in the Aerospace Sector

The aerospace sector is also a significant contributor to global GHG emissions. Aviation alone accounts for approximately 2 – 3 % of global CO_2 emissions, with an estimated 24 % by 2050 [21]. In 2004, commercial aviation emitted over 627 million metric tons of CO_2 and 2019 it increased to 900 million metric tons [22]. Besides CO_2, aviation also emits nitrogen oxides (NO_x), particulate matter, and water vapour, some of which have additional climate warming effects [21].

In response to this issue, the European Union (EU) developed a flight path for 2050 to reduce CO_2 and NO_x emissions by 75 % and 90 %, respectively [23]. Hydrogen offers a promising solution to achieve these goals, as shown in Fig. 1.3. Hydrogen propulsion methods in the aerospace sector can involve either hydrogen combustion, where conventional jet engines are modified to burn hydrogen instead of kerosene, or the conversion of hydrogen to electricity using FCs that drive the propeller or ducted fan [21]. The high energy density of hydrogen makes it an ideal fuel for long-haul flight. However, storing hydrogen for

aviation presents technical challenges, like those in the maritime sector, although with more stringent weight and volume constraints. Liquid hydrogen storage, which offers a higher energy density by volume than compressed hydrogen gas, is widely considered a viable solution.

Leading aerospace companies are testing hydrogen-powered prototypes [19] with plans for commercial deployment by the 2030s. Airbus is at the forefront of this innovative research, envisioning a hydrogen-powered version of Airbus A380 equipped with iron pods capable of producing up to 1.2 MW of power [24].

By integrating hydrogen system solutions into offshore wind farms, the marine sector, and the aerospace industry, the full potential of this renewable energy can be harnessed, while addressing the challenges of intermittency and energy security.

1.2 Research Motivation

The global need to reduce carbon emissions has led to significant growth in RE sources. However, these energy sources are inherently unstable due to their intermittent nature, creating a need to store energy generated under favourable conditions to ensure a stable and reliable power supply. Hydrogen energy systems, that is, the generation and utilisation of hydrogen, have recently gained widespread acceptance because of their environmental friendliness and long-term energy storage capabilities. Despite advances in these hydrogen energy systems, which include critical components such as ELs, FCs, and electrochemical batteries, significant challenges remain. These include the limited availability and high cost of ELs, the slow dynamic response of FCs, and an overall system efficiency typically ranging from 40 % to 50 % [6]. These factors present ongoing hurdles in maximising the efficiency and cost-effectiveness of hydrogen energy systems.

A crucial component in a hydrogen energy system is the power electronic converter (PEC) interfacing system. PECs play a vital role in hydrogen energy systems by enabling high-efficiency energy conversion, precise control across interconnected components, and effective power conditioning. Across the three sectors mentioned in Section 1.1, the PEC configurations can be described as follows:

- Fig. 1.4a: OWF, PEC configuration interfacing with an FC and EL, where hydrogen production is prioritised. For self-sufficiency, the FC powers the desalination unit and other on-turbine electrical needs and occasionally provides a black start for the offshore wind turbine.

- Fig. 1.4b: PEC configuration interfacing with a battery and FC for onboard aerospace or marine applications, supporting green operations within these sectors by utilising hydrogen as fuel.

- Fig. 1.4c: PEC configuration interfacing with an EL and batteries in onshore hydrogen production facilities powered by distributed energy (DE) sources, enabling hydrogen production and storage for subsequent use within a broader hydrogen infrastructure.

However, the PEC interfacing systems account for up to 12 % of the total losses in hydrogen energy systems [25]. In addition, as shown in Fig. 1.4a-c, these PECs (depicted as the converters of interest) interface individually with each main component, which introduces challenges such as increased component count and multiple conversion stages. These factors contributes to the low efficiency results reported in conventional systems. Given these challenges in current PEC configurations, there is a need for improved converter architectures and control techniques.

1.3 Aim and Objectives of Research

This research therefore aims to address these challenges by enhancing the performance, control, and efficiency of the PEC, thereby improving the overall operation of hydrogen energy systems. The focus is on the modeling, design, and control of the PEC interfacing system. The research aim will be achieved via the following objectives:

- Developing a comprehensive state-of-the-art survey of HESS and PEC interfacing topologies to identify operational challenges and shortcomings, proposing a topology to enhance the overall efficiency of hydrogen energy system by reducing component count and enabling centralised control.

- Performing a comprehensive comparative analysis of conventional decoupling control techniques for the proposed PEC interfacing systems reported in the literature, highlighting their relative attributes in terms of their effectiveness in handling cross-coupling issues across a wider operating region, forming a foundation for novel decoupling control techniques.

- Proposing a novel control technique for the proposed PEC interfacing system to address cross-coupling issues, ensuring precise control of multiple ports across a wider operating region in comparison with conventional techniques.

- Designing and validating an enhanced control technique that enables a minimal power flow error in the proposed PEC interfacing system under varying operating conditions.
- Building an experimental prototype of proposed PEC interfacing system in a laboratory setting to validate the new control techniques, thereby bridging the gap between theoretical designs and practical implementation.

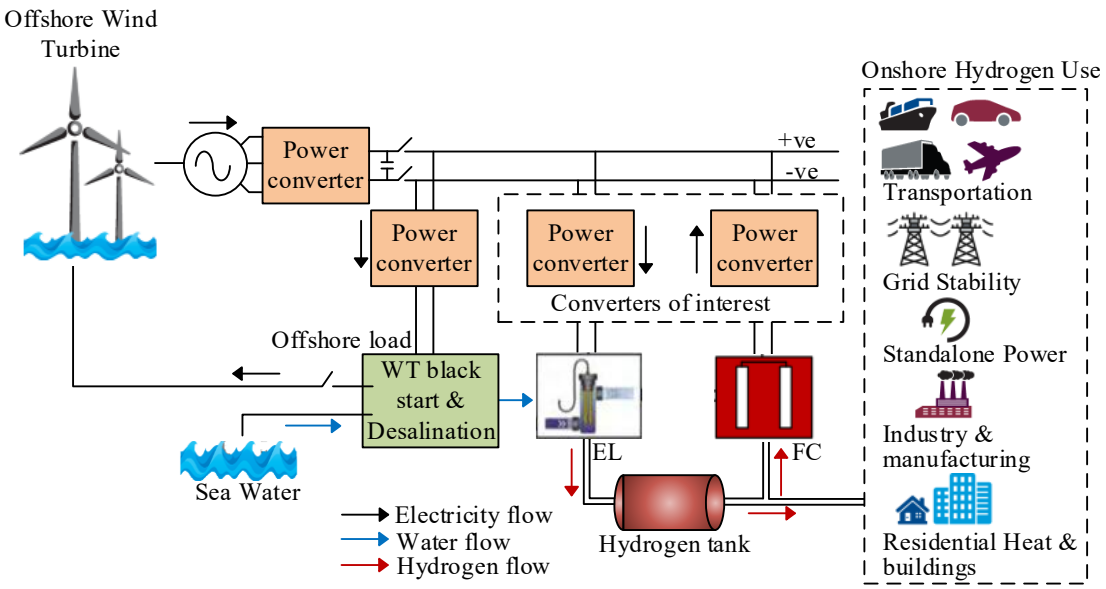

(a)

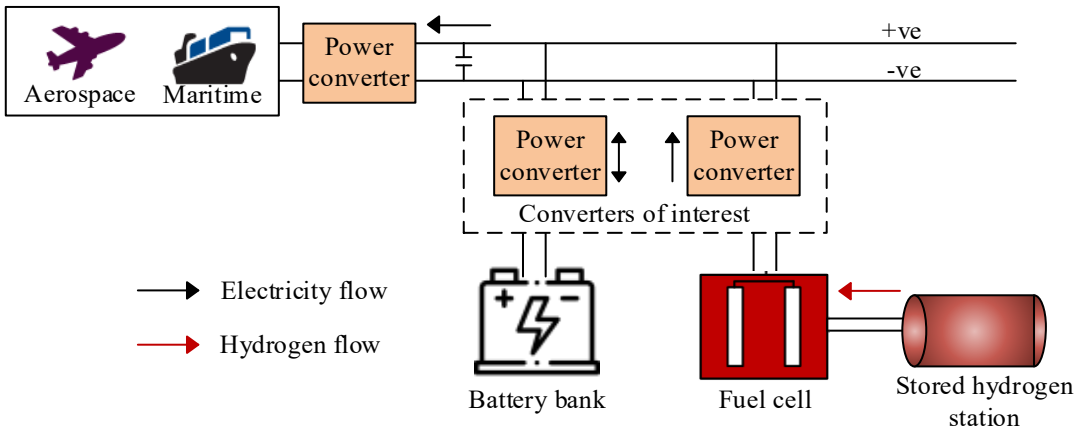

(b)

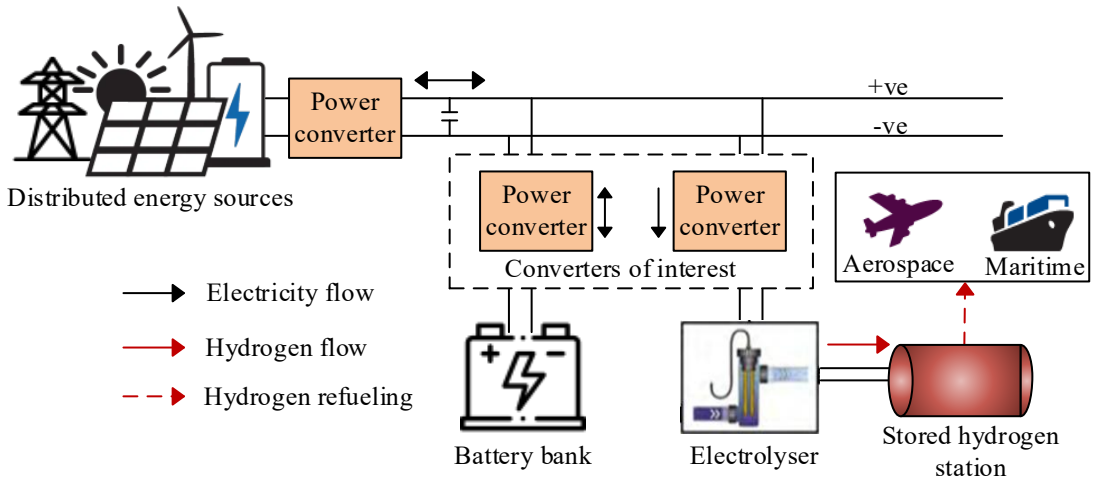

(c)

Fig. 1.4: Detailed hydrogen energy system application with PEC interfacing systems in the (a) offshore wind farm standalone hydrogen production (b) Onboard marine and aerospace sectors, and (c) Onshore hydrogen production with DE connection.

1.4 Publications

I. **O. E. Oyewole** and K. H. Ahmed, "Comparative Analysis of Decoupling Control Methods for Multiport-Isolated Bidirectional DC-DC Converter with Hydrogen Storage System Integration," presented at the 2023 11th International Conference on Smart Grid (icSmartGrid), 2023.

II. **O. E. Oyewole**, A. A. Abdelaziz, I. A. Jimoh, E. Bari, and K. H. Ahmed, "Optimised linear active disturbance rejection control of multiport-isolated DC-DC converter for hydrogen energy storage system integration," *Alexandria Engineering Journal,* vol. 102, pp. 159-168, 2024/09/01/ 2024, doi: https://doi.org/10.1016/j.aej.2024.05.107.

III. **O. E. Oyewole**, A. A. Abdelaziz, I. Abdelsalam, E. Bari, and K. H. Ahmed, "Novel model reference-based hybrid decoupling control of multiport-isolated DC-DC converter for hydrogen energy storage system integration," *Journal of Energy Storage,* vol. 109, p. 115175, 2025/02/15/ 2025, doi: https://doi.org/10.1016/j.est.2024.115175.

IV. **O. E. Oyewole** and K. H. Ahmed, "Software and Hardware-based Decoupling Control Comparison of Multiport-Isolated DC-DC Converters for Hydrogen Energy Storage Systems," presented at the IEEE PES ISGT Europe 2024, Dubrovnik, Croatia, Oct. 14 - 17, 2024.

V. **O. E. Oyewole**, I.A Jimoh, Y.N. Adelaziz, A. A. Abdelaziz and K. H. Ahmed. "Online Power Loss Minimisation of Multiport-Isolated DC-DC Converters for Hydrogen Fuel Cell System Integration", *IEEE Open Journal of Power Electronics* (Under Review).

1.5 Thesis Structure

The thesis is composed of six chapters, which are summarised briefly as follows:

Chapter 1 introduces the background of HESS as a long-term energy storage solution and outlines the contributions of its PEC interfacing systems. Additionally, the chapter details the research motivations, aims, and objectives.

Chapter 2 provides a comprehensive literature review on the developments of FC and EL technologies, which are key components of hydrogen energy systems. Additionally, it briefly explores FC/EL PEC interfacing systems reported in the literature. The review highlights the advancements and challenges associated with individually connected PECs and, consequently, proposes a topology that interfaces with the key components of a hydrogen energy system collectively, thereby reducing component count and enabling centralised control. Furthermore, the chapter presents a comparative analysis of conventional control techniques developed to achieve precise control within converter ports and minimising cross-coupling effects, thereby setting the stage for the proposed contributions in subsequent chapters.

Chapter 3 illustrates a novel decoupling control technique for the proposed PEC interfacing system, beginning with the decoupling control philosophy and the development of a hybridised technique that combines a conventional decoupling control technique. A detailed mathematical formulation of the decoupling control law is presented, along with simulation results obtained from a MATLAB/Simulink model. The proposed decoupling control technique is further validated using an experimental test rig. The chapter then concludes with a comparative analysis of the proposed novel decoupling control technique against benchmarked techniques reported in the literature.

Chapter 4 focuses on second proposed decoupling control technique which enhances the performance of a conventional control technique tailored for the proposed PEC interfacing system to achieve precise control and minimise cross-coupling effects. The chapter analyses the conventional control technique, highlights its limitations, and subsequently presents an optimisation method to improve its performance and ease of design.

Simulation results demonstrating the performance of the proposed decoupling control technique are presented, along with experimental validation.

Chapter 5 details the third proposed control technique, focusing on the minimisation of the power flow errors in the PEC interfacing system. The chapter entails an analysis of the power flow between ports, followed by the introduction of the adaptive control technique. In addition, a mathematical proof of the adaptive gain stability is presented, along with simulation results obtained in MATLAB/Simulink and experimental validation results. A comparative analysis with conventional control technique showcases the performance of the proposed adaptive control technique.

Chapter 6 presents the conclusions of the thesis, summarising the main findings and contributions of the research. Furthermore, suggestions for future work are provided, focusing on areas that could build upon the achievements of this thesis.

Chapter 2

Literature Review

This chapter presents a review of the fundamental components that make up a hydrogen energy system, with particular emphasis on the FC and EL. Over the years, hydrogen energy systems have evolved significantly, driven by the pursuit of higher efficiency and sustainability. Within a typical hydrogen energy system, several subsystems are strongly coupled, among which the PEC plays a contributary role in the overall system performance. Consequently, the ongoing development of advanced PEC topologies that can meet the stringent operational and efficiency requirements of hydrogen-based energy systems remains a key area of research.

2.1 Overview of FC/ EL Technologies

The following subsections give a brief overview of the basic technology and technical description of FC and EL.

2.1.1 Overview of FC Technologies

An FC is an electrochemical device that converts chemical energy from hydrogen directly into electricity with water and heat as a byproduct. FCs are typically classified based on their operating temperature and the type of electrolyte used. Common FC technologies include proton exchange membrane fuel cells (PEMFC), solid oxide fuel cells (SOFC), molten carbonate fuel cells (MCFC), phosphoric acid fuel cells (PAFC), and alkaline fuel cells (AFC). A basic comparison of these technologies is presented in Table 2.1.

As listed in Table 2.1, PEMFCs are the leading FC technology, operating at moderate temperatures that support quick start-up and stable performance under varying loads [26]. Operating at moderate temperature levels allows effective heat recovery and utilisation, improving overall system efficiency and ensuring reliable operation [27].

Furthermore, FCs generally exhibit a slow dynamic response to load changes [28], mainly due to the double-layer capacitance at the electrode-electrolyte interface. This capacitance behaves like a small energy storage element, delaying current adjustment during transients as the double layer charges or discharges. As a result, the FC voltage responds slowly to rapid load variations [29].

Table 2.1: FC Technologies

Technology	Temperature (°C)	Efficiency (%)	Capacity (kW)	Advantages	Disadvantages
PEMFC	60 - 80	40-60	< 250	High power density Quick start-up time Low operating temperature	Sensitive to fuel impurities Expensive catalyst (platinum)
SOFC	800-1000	> 50	1 – 250	Waste heat recovery High efficiency Solid electrolyte	High operating temperature Slow start-up
AFC	50 -200	~ 50	20 - 100	High conversion rate Quick start-up	Sensitive to fuel impurities (CO_2) Maintenance of electrolyte is difficult
MCFC	600-700	> 50	300 - 3000	High efficiency No need for metallic catalysts High capacity	Expensive Slow start-up Corrosion at high temperature
PAFC	~ 200	40	40 -1000	Low fuel quality requirements Generate high grade waste to heat	Low efficiency compared to other high temperature FCs Slow start-up

A single FC cell generates a voltage less than or equal to 1 V [29], requiring multiple cells to be stacked in series to achieve higher voltages. However, this stacking reduces the overall reliability of the FC because the failure of a single weak cell affects the entire stack. Consequently, a balance is often struck between achieving the desired high voltage and maintaining cell reliability, with the output voltage typically limited to approximately 100 V [29] as shown in Table 2.2.

Given the relatively low output voltage of FCs, PECs interfacing with FC systems are often step-up converters, as indicated by the difference between the bus and FC voltages in Table 2.2. In addition to increasing or decreasing the voltage, the PEC for FC applications must provide adequate voltage conditioning. Furthermore, owing to the slow dynamic

Table 2.2: Fuel cells voltages and the corresponding DC bus voltages

Reference	Fuel Cell Voltage (v)	DC Bus Voltage (v)	Field of application
[30]	100	540	Stand alone
[31]	70	350	Stand alone
[32]	30	750	Stand alone
[33]	50	400	Grid connected
[34]	20.2	40	Stand alone
[35]	52-105	36	Stand alone
[36]	26	100	Stand alone
[37]	24	70	Electric Vehicle
[38]	22-50	40-70	Stand alone
[39]	40	200	Grid connected / Stand alone
[40]	24	100	Fuel cell applications

response of FCs, energy storage devices, such as batteries or supercapacitors, are often integrated to handle high transients during sudden load changes.

2.1.2 Overview of EL Technologies

Hydrogen is generated through the splitting of water in a process called electrolysis, where electricity passes through water, producing hydrogen and oxygen as byproducts. The energy source used for this splitting process determines the classification of the hydrogen produced. For instance, green hydrogen is exclusively generated from 100 % renewable energy sources [6].

Four main EL technologies are commonly used for electrolysis: solid oxide electrolysers (SOE), proton exchange membrane electrolysers (PEMEL), anion exchange membrane electrolysers (AEMEL), and alkaline electrolysers (AEL). AEL remains the most commercially mature and cost-effective technology, although its slow dynamic response and low tolerance to water impurities limits its suitability for dynamic load applications. PEMEL, which offers faster response times and high hydrogen purity, is limited by its early maturity and sensitivity to water quality [41], [6]. Recent advancements in SOE suggest its potential for integration into high-temperature processes, although irregular electrode stability and high operational temperatures require further development. Similarly, AEMEL promises cost efficiency due to its inexpensive components, but requires further research to address membrane stability and ion conductivity issues [42], [43]. Table 2.3 compares the primary characteristics of the four technologies.

Table 2.3: Typical Electrolysers Technologies [14], [6], [44]

Technology	Power consumption ($KW.h/m^3$)	Efficiency (%)	Cell voltage (v)	Stack Life (h)	Advantages	Disadvantages
PEMEL	4.0 – 5.5	67 - 82	1.80 – 2.40	<60,000	Fast response High H_2 purity	Early maturity Low tolerance to water impurities
SOE	4.0 – 4.3	100	0.95 – 1.30	<40,000	Lower costs Functional as FC	Experimental stages Irregular electrodes
AEMEL	4.0 -4.6	50 -70	1.85	>10,000	Inexpensive parts High H_2 purity	Low membrane stability Low ion conductivity
AEL	4.0 – 4.3	62 - 84	1.8 - 2.40	<90,000	Mature technology Lower costs	Slow response Low tolerance to water impurities

As shown in Table 2.3, the low cell voltage of ELs requires stacking multiple cells to reach the desired operating voltage. However, increasing the number of stacks can reduce overall system reliability, creating a trade-off between achieving higher voltage and maintaining reliability. Moreover, the dynamic response may be influenced by interactions among auxiliary components within the stack. Hence, direct connection of EL stacks to power sources is often impractical. To address these challenges, PECs are employed to step down and stabilise the voltage and ensure reliable EL operation for hydrogen production.

Furthermore, in the literature, EL modelling approaches are broadly classified into three types: dynamic, static load, and resistive load [45]. Dynamic models capture the time-dependent behaviour and transient responses of ELs, making them suitable for detailed electrochemical and thermal analysis. Static load models, on the other hand, focus on simplified representations under constant load conditions, primarily aimed at steady power demand scenarios. Resistive load models approximate the EL as a resistive load, allowing for the direct assessment of power consumption based on voltage and current inputs. In this work, the resistive load model is chosen owing to its straightforward application and simplicity of analysis.

2.2 Converter Topologies for FC/ EL Interface

ELs and FCs are essential components of hydrogen energy systems. ELs split water into hydrogen and oxygen using electrical energy, while FCs convert the stored hydrogen back into electricity. Hydrogen energy system relies on several auxiliary subsystems to function efficiently, including air and hydrogen supply systems, cooling and heat exchangers, humidification systems, and PECs, which are highly interconnected to optimise overall performance [45], [46].

PECs play a critical role for both EL and FC operation. For ELs, they regulate the electrical input for water splitting, maintain voltage and current levels to maximise efficiency, and prevent component degradation. For FCs, PECs condition the generated electricity and convert it into a form suitable for integration into the final power output.

Given the specific operating characteristics of ELs and FCs, PECs must meet certain functional and performance requirements. As described in [47], [48], [49] candidate PEC topologies should provide a wide voltage conversion range, galvanic isolation, low current ripple, high efficiency, high power density, and compact size.

The PECs for EL/FC systems are summarised in Table 2.4 and Table 2.5, which highlights their advantages and disadvantages. Non-isolated topologies are typically characterised by a simplified design, compact structure, and cost-effectiveness. However, they have several limitations. They often require a high duty ratio, leading to increased current ripple, which lowers efficiency. The lack of galvanic isolation also raises safety concerns in high-power applications and restricts the integration of multiple sources with different voltage levels. Consequently, system stability and control become more complex. Moreover, non-isolated converters are more susceptible to electromagnetic interference (EMI) and tend to exhibit reduced noise immunity [50].

To overcome these drawbacks, isolated converter topologies are employed. These converters use transformers or coupled inductors to provide galvanic isolation, enhancing safety and noise immunity. They are particularly well suited for FC/EL applications that demand high voltage conversion and strong system protection. In addition, the use of isolated converters supports compliance with ISO22734:2020 and ISO19880-1:2020 standards, which emphasise electrical safety and grounding requirements for hydrogen generation and fuelling systems [51].

Table 2.4: EL/FC Non Isolated converters

Topology	Description	Advantages	Disadvantages
Interleaved Buck [52]	Utilises multiple buck phases operating out of phase to share current and reduce input ripple	Reduces input current ripple and distributes thermal stress.	High voltage stresses on the switch and diode terminals increasing complexity
Interleaved Synchronous Buck [53]	Replaces freewheeling diodes in interleaved buck with synchronous switches.	This further reduces conduction losses, improved efficiency, especially at higher load currents.	Higher voltage stress on switches, increase design and control complexities.
Stacked Interleaved Buck [54]	Adds auxiliary capacitors to conventional interleaved topology	Low ripple over wide duty ratio range.	Increased complexity and component count with more phases and higher implementation cost
Switched Inductor Boost[55], [56]	Utilises additional inductors charged in parallel and discharged in series	Improved voltage gain and conversion efficiency.	Requires more passive components, increasing circuit complexity and cost.
Floating Interleaved [57]	Combines the principles of interleaving with a floating configuration	Higher voltage gain, reduced ripple, improved current sharing between phases	Increased component count, higher cost and need for precise current balancing
Floating Interleaved Cascaded Boost [58]	Integrates interleaving, cascading, and floating configurations.	Achieves high voltage gain, ripple reduction, and improved power distribution	Requires large inductors to reduce input current ripple, leading to increased size, weight, and reduced reliability

Table 2.5: FC/EL Isolated Converters

Topology	Description	Advantages	Disadvantages
Forward [59]	Employs a single switch, isolation transformer, output diode(s), and a demagnetising (clamping) circuit.	Continuous energy transfer; relatively simple design and moderate component count	Risk of transformer core saturation due to unbalanced magnetising currents; increased voltage/current stress.
Push-Pull [60]	Adds a second switch to the forward converter, allowing alternated conduction in transformer windings.	Improved voltage gain, continuous power transfer, reduced output ripple.	Limited utilisation of the transformer's primary winding; high voltage stress.
Half-Bridge Isolated [61]	Consists of two power switches, a high-frequency isolation transformer, and a diode rectifier.	Simple and cost-effective, reduced transformer size, moderate component count.	Possibility of higher voltage and current stresses on switches
Full-Bridge Isolated [62]	Builds on half-bridge by adding two more switches, forming a complete H-bridge across the transformer.	Full positive and negative voltage cycles during operation enable bidirectional voltage operation.	Higher switching losses (especially under hard switching), complex gate drive.
Dual Active Bridge [63]	Consists of two full H-bridges on both sides of an HF transformer.	Enables bidirectional power transfer, high power density.	Complex control techniques, high switching losses under hard-switching conditions.
Multiport Isolated DC-DC [64], [65], [66]	Consist of different configuration of converter at a multiple side of the HF transformer	Enables bidirectional power transfer, power flow can be independently controlled, high voltage gain ratio, achieves EMI reduction, low output ripple current	Complex control techniques, high switching losses under hard-switching conditions

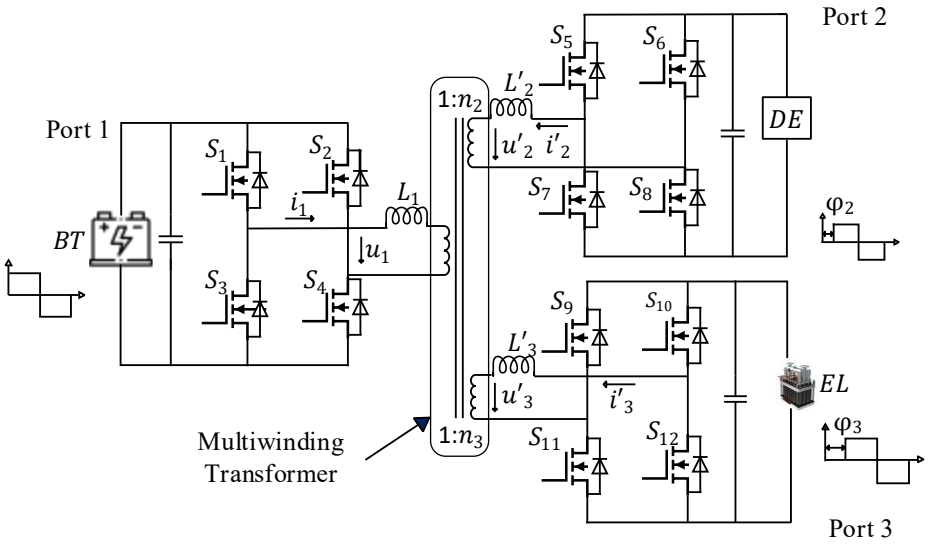

Fig. 2.1: Multiport (three ports) isolated DC-DC converter.

Nevertheless, conventional isolated designs often rely on separate converters operating independently for each subsystem, leading to multiple conversion stages, circulating currents, complex control schemes, and bulky architectures. These limitations reduce efficiency, reliability, and scalability. To address these challenges, multiport-isolated DC–DC converters, especially three-port configurations, have emerged as promising alternatives. They enable simultaneous integration of multiple energy sources within a single architecture, thereby reducing conversion stages and improving transient response, dynamic power sharing, and overall system efficiency. Their compactness, and high power density make them ideal for hydrogen energy systems applications.

Several studies [67], [68] and [64] have investigated three-port converters using a full-bridge circuit for each port, as illustrated in Fig. 2.1. Full-bridge configuration offers distinct advantages that make it highly suitable for hydrogen energy systems. It maximises voltage gain by fully utilising the transformer turns ratio, allowing wide voltage operation ranges. Its structure also enables balanced power flow between ports, enhancing stability under varying load and source conditions. The full-bridge configuration also better handles voltage and current stresses, resulting in lower ripple and improved conversion efficiency, particularly at high power levels.

Table 2.6. Decoupling control techniques in literature

Category	Subcategory	Key Idea	Typical Techniques	Remarks
Hardware Decoupling	Addition-based hardware decoupling	Adding supplementary components or auxiliary circuits that could alter system dynamics and reduce port interaction	Resonant capacitors [69], additional switches [70], relays[71], variable inductors [72] / capacitors [73],	May increase losses, cost, bulkiness and reduce scalability
	Modification-based hardware decoupling	Structurally modifying converter hardware such as redesigning magnetic or winding configurations	Modified transformer windings [74], Inherent decoupling [75]	Increases design complexity
Software Decoupling	Non-linear software-based decoupling	Designed to handle the inherent nonlinear dynamics of the converter	SMC/ESO/ flatness-based [76], MPC [77],[78], ANN [79], [80], frequency domain techniques [81]	Computationally intensive, complex tuning, high processing power
	Linear software-based decoupling	By approximating system dynamics around an operating point and using compensation terms or observers	Feedback linearisation [82], polar coordinate [83], LADRC [84], Adaptive P&O [85], bandwidth selection [86], matrix-based [87]	Easier to implement, but could have estimation errors, limited adaptability, increased storage needs

2.3 Multiport-Isolated (Three Port) DC-DC Converter Interface

Multiport-isolated DC–DC converters function as multiple-input, multiple-output systems, with interconnected power ports separated by a multiwinding transformer. This architecture enables the simultaneous integration of multiple energy sources and load. Its efficient power sharing makes it suitable for hydrogen energy systems.

However, despite their advantages, multiport converters present two key areas for improvement. Firstly, the multiwinding transformer in a multiport-isolated converter

inherently exhibits cross-coupling due to electromagnetic interactions between the coils. As a result, the converter behaves like a Multiple Input Multiple Output (MIMO) system with coupled control loops, which makes it difficult to control [81]. These cross-coupling effects affects optimal performance by disturbing the intended power flow, introducing voltage and current distortions, and increasing control complexity [68]. In essence, when the output characteristics of one port change, they indirectly affect the output of the other ports. For example, a load step at one port requires a change in the phase shift of that port. However, due to magnetic coupling, the power transfer of the other load port is also affected, requiring a readjustment of its phase shift [88]. These cross-coupling effects thus manifest as DC port current disturbances that are undesirable for converter operation [89] To mitigate this, decoupling controls have been developed in the literature from both software-based (linear and nonlinear) and hardware-based perspectives. Table 2.6 briefly presents various decoupling controls, the key ideas behind each decoupling philosophy, and a general overview remark. While hardware decoupling introduces the addition or modification of physical components, which increases cost and bulkiness, nonlinear software-based methods are more computationally intensive and require complex tuning. Linear software-based techniques, though easier to implement, can be susceptible to estimation errors, have limited adaptability, and often require increased storage for look-up tables (LUTs).

Furthermore, conventional solutions to address the cross-coupling effects in multiport converters often rely on single-phase shift (SPS). This technique provides only two degrees of freedom: the phase shift between the origin port (typically port 1) and port 2, and the phase shift between the origin port and port 3 [90]. These limited degrees of freedom have been shown to result in higher rms currents in the inductors, which increases losses [91]. To overcome these limitations, researchers have introduced additional degrees of freedom through advanced control schemes, such as dual-phase shift (DPS) and triple-phase shift (TPS). By exploiting these additional phase shifts, power flow can be more precisely controlled, reducing rms current and associated losses. Nevertheless, achieving optimal phase shift values remains crucial. Table 2.7 illustrates these control schemes, including typical methods employed in the literature and their general overview.

Table 2.7: Typical techniques for control schemes

Control scheme	Degrees of freedom	Typical techniques	Remarks
SPS	Two external phase shifts	Basic TAB control without internal phase shifts [84],[83],[75]	High rms current leading to conduction, switching loses
DPS	Two external phase shifts plus an equal number or a single internal phase shift	Simplified high frequency chain current [92], Genetic algorithm with LUT storage [93], generalised harmonic modelling with optimisation technique [94]	Increased storage requirement, does not fully exploit all degrees of freedom
TPS	Two external phase shifts plus distinct internal phase shift values	Offline PSO [95], PSO with exponential weighted moving average [96], ANN-based optimisation [97, 98], Offline gradient descent with ripple correlation control and ANN [99], GHA with polynomial regression [100], adaptive perturb and observe [85], advanced model predictive control [90], gradient descent optimisation [101]	Reduces rms current and power losses but is computationally intensive, relies on static tuning mechanisms, requires large look-up tables, and is challenging for practical digital implementation

2.4 Multiport-Isolated (Three Port) DC-DC Converter Principles of Operation

Multiport-isolated DC-DC converters are derived from the principles of dual active bridge (DAB) with the addition of more legs to either side of the transformer. This can result in either symmetric or asymmetric configurations. A 1:2 triple-active bridge converter configuration is analysed in the following subsection.

2.4.1 Equivalent Circuit

The topology is shown in Fig. 2.1 and is composed of full-bridge converters with port 1 labelled as the BT port, port 2 as the DE, and port 3 labelled as the EL (represented by a resistive load). Negative power is the power supplied by a port, whereas positive power is the power absorbed by the port. The integrated multiwinding transformer has turns ratios of

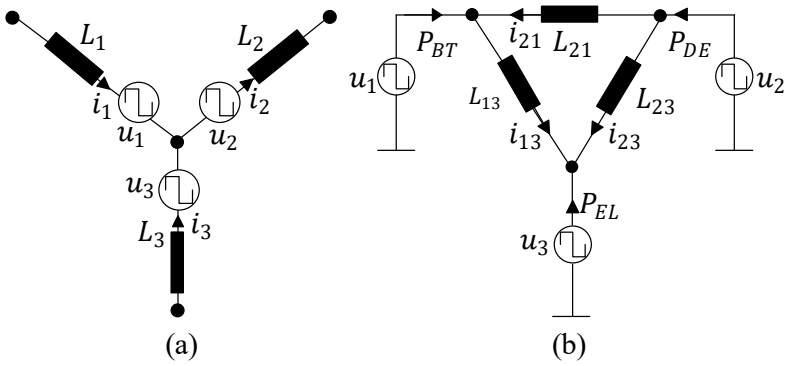

Fig.2.2: (a) TAB star connection and (b) TAB delta connection.

$1:n_2$ and $1:n_3$, respectively. Power transfer is influenced by the leakage inductance of the high-frequency multiwinding transformer, which is determined by the phase shift of each full-bridge control signal. In this topology, external inductances are used, because the leakage inductance of the transformer may be low. L_1 is the port 1 bridge leakage inductance, L'_2 is the port 2 leakage inductance, and L'_3 is the port 3 leakage inductance [102].

The parameters are defined as follows: The output signals of each bridge's midpoint square-wave voltage are presented as u'_1, u'_2 ,u'_3, respectively with a duty ratio of 0.5 [103], [104]. The midpoint AC voltages, output DC voltage, leakage inductances, and leakage inductance currents, all referred to the primary side, are calculated as given by (2.1) and (2.2), respectively.

$$u_2 = \frac{u'_2}{n_2},\ V_2 = \frac{V'_2}{n_2},\ L_2 = \frac{L'_2}{n_2^2}, i_2 = i'_2 n_2 \tag{2.1}$$

$$u_3 = \frac{u'_3}{n_3},\ V_3 = \frac{V'_3}{n_3},\ L_3 = \frac{L'_3}{n_3^2}, i_3 = i'_3 n_3 \tag{2.2}$$

To facilitate power flow analysis, as described in [68] and [105], it is necessary to calculate the equivalent inductances between each port. The equivalent inductances are calculated by transforming the star equivalent (Fig.2.2a) to the delta equivalent (Fig.2.2b), referring all circuit parameters to the primary side [95]. The leakage inductances of the delta model L_{12} , L_{13}, and L_{23} , as shown in [106] can be expressed as :

$$L_{12} = \frac{A}{L_3}\ , L_{13} = \frac{A}{L_2}\ , L_{23} = \frac{A}{L_1} \tag{2.3}$$

$$A = L_1 L_2 + L_2 L_3 + L_1 L_3 \tag{2.4}$$

2.4.2 Power Flow of the Converter

The midpoint voltages of each bridge are generated by alternately driving the gate signals of switches S_1 and S_4, S_2 and S_3 in the BT port. Similarly, in the DE and EL ports, the gate signals for S_5 and S_8, S_6 and S_7, as well as S_9 and S_{12}, S_{10} and S_{11}, respectively are operated in complementary switching patterns. The phase shift between the control signals u_1 and u_2', denoted as φ_2, and between u_1 and u_3', denoted as φ_3, governs the power transfer between bridges.

The phase shifts φ_2 and φ_3 can be positive or negative, depending on whether the corresponding bridge square-wave voltages lead or lag relative to each other. A positive phase shift ($\varphi_2 > 0$) indicates u_1 leads u_2', whereas a negative phase shift ($\varphi_2 < 0$) indicates u_1 lags u_2'. Similarly, the sign of φ_3 reflects the phase relationship between u_1 and u_3'. The BT port is used as a reference, maintaining its phase shift at zero. The maximum power transfer occurs at $\frac{\pi}{2}$. To ensure stable operation, the phase shifts are constrained to the range $-\frac{\pi}{2}, \frac{\pi}{2}$. This control technique, commonly referred to as SPS control, extends the phase-shifting approach used in DAB to a multiport active bridge topology, thereby enabling efficient power transfer across multiple ports.

As calculated in [105], using cycle-by-cycle averaging, the power between any two ports can be expressed as:

$$P_{xy} = \frac{\varphi(\pi - \varphi)V_x V_y}{2\pi^2 f_s L_{xy}} \tag{2.5}$$

where, x and y represent 1, 2 or 3, indicating port numbers, V_x and V_y are the voltages of the two ports, f_s denotes the switching frequency, φ is the phase difference between the operating points, and L_{xy} is the inductance between the two ports in delta transformation.

The power flow in each port P_{BT}, P_{DE}, P_{EL} represents the total active output powers which are defined as:

$$\begin{aligned} P_{BT} &= -P_{12} - P_{13} \\ P_{DE} &= P_{12} - P_{23} \\ P_{EL} &= P_{13} + P_{23} \end{aligned} \tag{2.6}$$

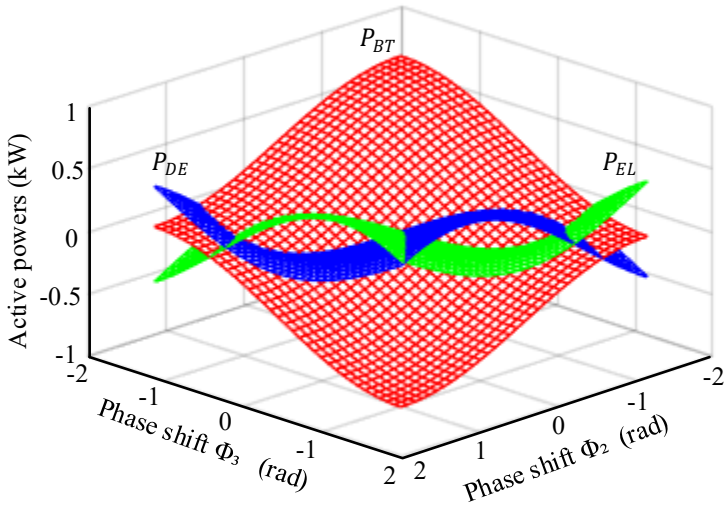

Fig.2.3: Power transfer vs phase shift showing cross-coupling.

This can be further expressed as:

$$P_{BT} = \frac{\varphi_2(\varphi_2 - \pi)V_1V_2L_3 + \varphi_3(\varphi_3 - \pi)V_1V_3L_2}{2\pi^2 f_s A}$$
$$P_{DE} = \frac{\varphi_2(\varphi_2 - \pi)V_1V_2L_3 + (\varphi_3 - \varphi_2)(\varphi_2 - \varphi_3 - \pi)V_2V_3L_1}{2\pi^2 f_s A} \quad (2.7)$$
$$P_{EL} = \frac{\varphi_3(\pi - \varphi_3)V_1V_3L_2 + (\varphi_3 - \varphi_2)(\pi - \varphi_2 + \varphi_3)V_2V_3L_1}{2\pi^2 f_s A}$$

where, $A = (L_1L_2 + L_2L_3 + L_1L_3)$

It can be clearly seen from (2.7) that a non-linear relationship exists between the power of each port and the phase shifts. The phase shifts exhibit a coupling relationship with each other.

The relationship between the port's active output power flow and the phase shifts is as illustrated in Fig.2.3 based on (2.7). Fig.2.3 demonstrates that each port's transferred power is a function of multiple phase-shifts. The overlap of the P_{BT}, P_{DE}, and P_{EL} surfaces show that adjusting one phase shift simultaneously alters the powers of other ports. This shows the inherent power cross-coupling in TAB converters.

2.4.3 Cross-Coupling Analysis

As in (2.7), the cross-coupling effect of the phase shifts (which are the control variables) on the power equation must be eliminated to allow precise control of the system.

The control objective is to derive a feedback control system to regulate the power in the output ports. However, the power equations of (2.7) are non-linear with phase shift ratios φ_2 and φ_3.

State-space averaging is commonly used to estimate the dynamics of DC-DC converters. However, applying this technique to isolated converters, such as the multiport-isolated DC-DC converter, can be challenging. One of the state variables in the converter is the transformer current, which does not satisfy the small ripple approximation. Since power flow coupling can be analysed using low-frequency dynamics, the impact of the high frequency dynamics of the transformer leakage inductance can be neglected [107]. Following the steps illustrated in Fig.2.4, the obtained non-linear model must be linearised.

To derive the linearised model from (2.7), without considering the different magnitudes of the phase shifts, a sinusoidal approximation, as seen in (2.8) and (2.9), is applied:

$$(\pi - |\varphi|) \approx X \sin \varphi \tag{2.8}$$

where X is the Fourier coefficient.

$$X = \frac{1}{\pi}\int_{-\pi}^{\pi} \varphi(\pi - |\varphi|) \sin \varphi \, d\varphi = \frac{8}{\pi} \tag{2.9}$$

Hence, the basic equations of the converter's control objectives are expressed in (2.10) and (2.11).

$$I_{DE} = \frac{P_{DE}}{V_{DE}} = \frac{4(V_{BT}L_3 sin\varphi_2 + V_{EL}L_1 sin(\varphi_2 - \varphi_3)}{\pi^3 f_s A} \tag{2.10}$$

$$I_{EL} = \frac{P_{EL}}{V_{EL}} = \frac{4(V_{BT}L_2 sin\varphi_3 + V_{DE}L_1 sin(\varphi_3 - \varphi_2)}{\pi^3 f_s A} \tag{2.11}$$

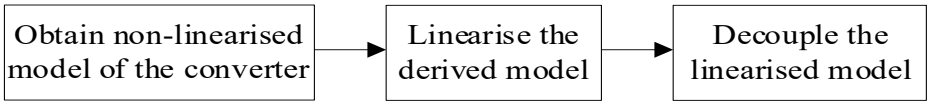

Fig.2.4: Steps for the linear decoupling control technique.

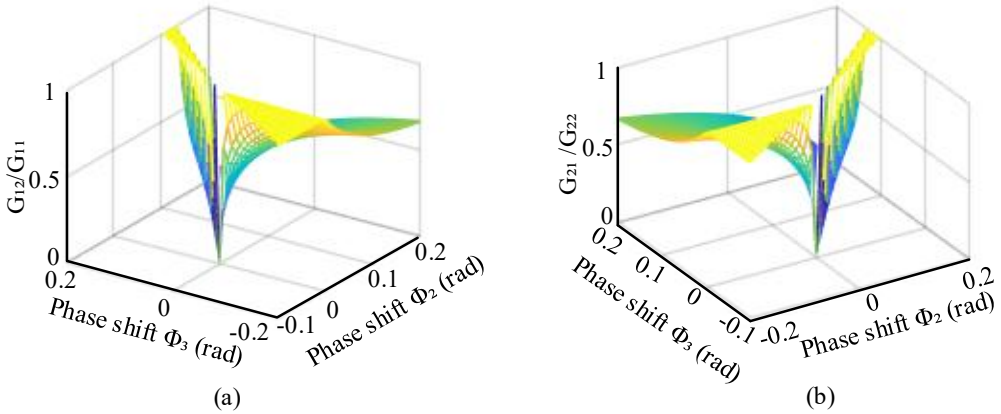

Fig.2.5: Degrees of cross-coupling with control inputs linearised around the origin (a) interaction in the DE port (b) interaction in the EL port.

The operating point of the converter is selected based on the phase shifts φ_2 and φ_3, with the possibility of minimal conduction and switching losses. According to [68], the operating point corresponding to the lowest phase shift results in the least loss. To simplify analysis, the converter can be linearised by approximating φ_2 and φ_3 near the origin. The Taylor series of (2.10) and (2.11) around a certain operating region closest to the origin can be expressed as follows:

$$\begin{bmatrix} I_{DE} \\ I_{EL} \end{bmatrix} = \begin{bmatrix} \frac{4(V_{EL}L_1 + V_{BT}L_3)}{\pi^3 f_s A} & \frac{-4V_{EL}L_1}{\pi^3 f_s A} \\ \frac{-4V_{DE}L_1}{\pi^3 f_s A} & \frac{4(V_{DE}L_1 + V_{BT}L_2)}{\pi^3 f_s A} \end{bmatrix} \begin{bmatrix} \varphi_2 \\ \varphi_3 \end{bmatrix} \tag{2.12}$$

Therefore, the plant transfer matrix G can be simply represented as:

$$\begin{bmatrix} I_{DE} \\ I_{EL} \end{bmatrix} = G \begin{bmatrix} \varphi_2 \\ \varphi_3 \end{bmatrix} \tag{2.13}$$

Equation (2.13) forms a two-input, two-output model with a plant transfer matrix G. The output currents interfere with each other because the non-diagonal elements are non-zero. The degree of cross-coupling is quantified by the ratio of the non-diagonal elements to

the corresponding diagonal elements of the gain matrix. The surface plots, as seen in Fig.2.5, tilts in two directions for both loops, indicating that each control output is influenced by both control inputs. The coupling ratio ranges between 0 and 1, where values close to 0 indicate weak/negligible coupling and values approaching 1 indicate strong coupling. When the non-diagonal elements are zero, the system becomes fully decoupled [89]. Matrix-based decoupling control eliminates interference by systematically choosing a matrix that limits or cancels out the effect of this interference. The chosen matrix is referred to as the decoupling matrix (DM).

2.4.4 Cross-Coupling Effects

The following sub section briefly outlines the cross-coupling effects in a hydrogen energy system application.

2.4.4.1 Fuel Utilisation and Reduced System Performance

The power generation/consumption process of the FC/EL is not only a relationship between voltage and current, but also the fuel utilisation, temperature, and pressure, which affect the output voltage. The relationship between these parameters [108] is depicted in (2.14):

$$q_{in}^{H_2} = \frac{2(N_0/2F)I_{FC}}{UC_v}$$

$$V_{FC} = N_0\left(E_0 + \frac{RT}{2F}\left(In\frac{P_{H_2}\sqrt{P_{O_2}}}{P_{H_2O}}\right)\right), \quad P_{FC} = I_{FC}V_{FC} \tag{2.14}$$

where, U is the fuel utilisation, $q_{in}^{H_2}$ is the hydrogen gas in, N_0 is the number of series cells in a stack, F is Faraday's constant, P_{H_2}, P_{H_2O}, and P_{O_2} are the pressures of hydrogen, water, and oxygen, respectively; V_{FC} is the FC output voltage; and I_{FC} and P_{FC} are the FC output current and power, respectively. The transients in the sudden change in current or voltage affect fuel utilisation in the FC and, by implication, hydrogen production in the EL. This leads to reduced system performance, producing less hydrogen in the EL or consuming more hydrogen in the FC than is necessary [46].

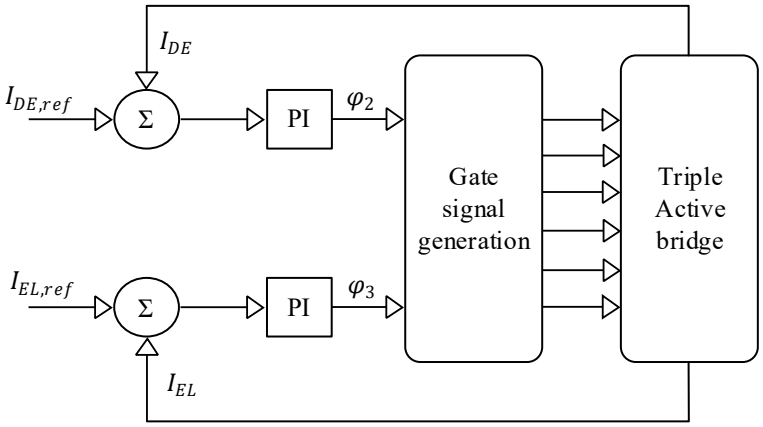

Fig.2.6: Triple active bridge converter control.

2.4.4.2 Impact on Lifespan

The lifespans of the EL and FC are critical issues, particularly considering the various coupled parameters and operating conditions in the hydrogen energy systems. For example, the lifespan of a typical proton exchange membrane (PEM) is 10,000 − 60,000 h [43]. Sudden changes in the electrical load (such as increased power demand) affect hydrogen energy systems operation, straining the system owing to transients [43].

2.5 TAB Control and Comparative Analysis of Matrix-based Decoupling Control Techniques

The proportional integral (PI) - based control scheme of the converter without any decoupling control technique is illustrated in Fig.2.6. The system is depicted as a two-input two-output control system. Based on PI control laws, φ_2 can be calculated as follows:

$$\varphi_2 = K_P\left(I_{DE,ref} - I_{DE}\right) + \frac{K_I}{s}\left(I_{DE,ref} - I_{DE}\right) \tag{2.15}$$

where, K_P is the proportional gain and K_I is the integral gain of the PI controller. The second PI control loop followed the same principle as the DE control loop. Thus, its equation is given as:

$$\varphi_3 = K_P\left(I_{EL,ref} - I_{EL}\right) + \frac{K_I}{s}\left(I_{EL,ref} - I_{EL}\right) \tag{2.16}$$

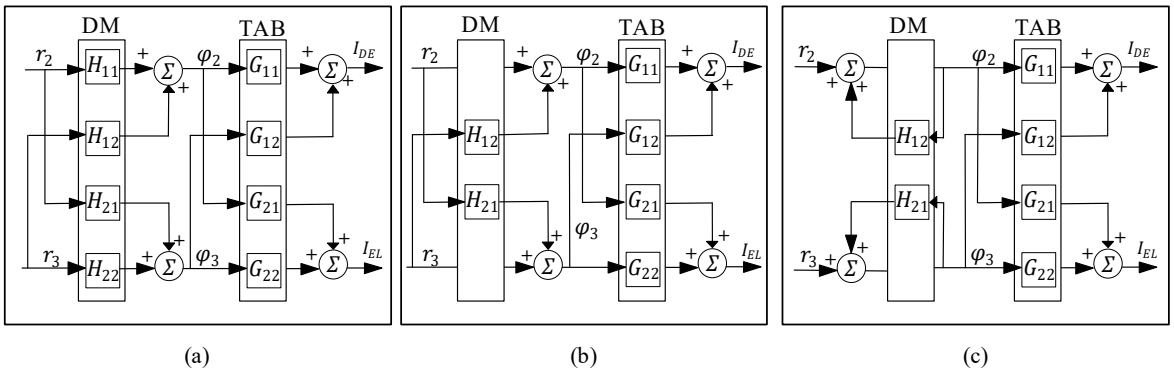

Fig.2.7: (a) Inverse matrix-based decoupling control technique, (b) Simplified matrix-based decoupling control technique. (a) Inverted matrix-based decoupling control technique.

In these control schemes, the energy delivered by BT is not controlled directly. It is allowed to freely sink or source the power difference between the EL and the DE. This is similar to a self-directed system that matches EL power demand variations while maintaining a constant DE power supply.

However, this basic control technique does not solve the pressing issue of cross-coupling inherent in multiport-isolated DC-DC converters. Three matrix-based decoupling control techniques are commonly implemented in the literature: inverse matrix decoupling control, simplified decoupling control, and inverted decoupling control. The following sections briefly describe each of these techniques.

2.5.1 Inverse Matrix Decoupling Control Technique

In this technique, the cross-coupling effect is eliminated by choosing a decoupling matrix that is the inverse of the plant transfer matrix. This technique has no negative effects on ideal plant properties. As shown in Fig.2.7a, if an inverse of matrix G is introduced into (2.12), the diagonal input-output matrix is derived as in (2.17)

$$\begin{bmatrix}\varphi_2\\ \varphi_3\end{bmatrix} = H\begin{bmatrix}r_2\\ r_3\end{bmatrix} = G^{-1}\begin{bmatrix}r_2\\ r_3\end{bmatrix} \tag{2.17}$$

where, H can be expressed as:

$$H = \frac{1}{4KV_1}\begin{bmatrix}\pi^3 f_s A(V_1L_2 + V_2L_1) & \pi^3 f_s AV_3L_1\\ \pi^3 f_s AV_2L_1 & \pi^3 f_s A(V_1L_3 + V_3L_1)\end{bmatrix} \tag{2.18}$$

with $K = V_3L_1L_2 + V_1L_2L_3 + V_2L_1L_3$.

Substituting (2.18) and (2.19) into (2.13) yields

$$\begin{bmatrix} I_{DE} \\ I_{EL} \end{bmatrix} = \begin{vmatrix} G_{11} & G_{12} \\ G_{21} & G_{22} \end{vmatrix} \begin{vmatrix} H_{11} & H_{12} \\ H_{21} & H_{22} \end{vmatrix} \begin{bmatrix} r_2 \\ r_3 \end{bmatrix} \tag{2.19}$$

The product of the plant matrix and the inverse matrix, gives rise to matrix M, which is a fully decoupled system.

$$M = \begin{vmatrix} G_{11} & G_{12} \\ G_{21} & G_{22} \end{vmatrix} \begin{vmatrix} H_{11} & H_{12} \\ H_{21} & H_{22} \end{vmatrix} \tag{2.20}$$

Elaborating on matrix M gives:

$$M = \begin{vmatrix} G_{11}H_{11} + G_{12}H_{21} & G_{11}H_{12} + G_{12}H_{22} \\ G_{21}H_{11} + G_{22}H_{21} & G_{21}H_{12} + G_{22}G_{22} \end{vmatrix} \tag{2.21}$$

Following the control diagram illustrated in Fig.2.7a, the control outputs are given by

$$I_{DE} = (G_{11}H_{11} + G_{12}H_{21})r_2 + (G_{11}H_{12} + G_{12}H_{22})r_3 \tag{2.22}$$

$$I_{EL} = (G_{21}H_{11} + G_{22}H_{21})r_2 + (G_{21}H_{12} + G_{22}H_{22})r_3 \tag{2.23}$$

Evaluating this matrix results in the cross-coupling terms $(G_{11}H_{12} + G_{12}H_{22})$ and $(G_{21}H_{11} + G_{22}H_{21})$ becoming zero, indicating a decoupled system. The resulting input output matrix therefore reduces to the identity matrix, with the remaining dynamics determined by the DC-side energy storage elements [89].

2.5.2 Simplified Decoupling Control Technique

In the simplified decoupling technique, only two elements in the decoupling matrix must be generated compared with the four elements generated by the inverse decoupling technique. This sets two elements in the diagonal of the decoupling matrix to one, such that matrix H is $[1\ \mathrm{H}_{12}; \mathrm{H}_{21}\ 1]$. Therefore, matrix H can be expressed in terms of the transfer matrix of the plant, as given by (2.24).

$$H = \begin{bmatrix} 1 & -\frac{\mathrm{G}_{12}}{G_{11}} \\ -\frac{\mathrm{G}_{21}}{G_{22}} & 1 \end{bmatrix} \tag{2.24}$$

Although it is simple to implement in practice, there are some summation elements in the decoupling matrix, which makes tuning the controller difficult. A schematic of the simplified decoupling technique is shown in Fig.2.7b

2.5.3 Inverted Decoupling Technique

The inverted decoupling control technique is the third examined matrix-based decoupling control technique for suppressing the cross-coupling effects. Here, H_{12} and H_{21} are set such that,

$$H_{12} = -\frac{G_{12}}{G_{11}}$$
$$H_{21} = -\frac{G_{21}}{G_{22}} \quad (2.25)$$

As stated in [109] and [110], inverted decoupling has the same required compensation elements as simplified decoupling does. However, as shown in Fig.2.7c, the direction of the flow through the decoupling elements and the position of the summation are reversed compared to the simplified decoupling. It has a simple implementation and can always be configured such that its decoupling element is realisable.

The decoupling matrices are typically pre-calculated offline to simplify the real-time implementation. The pre-calculated values are stored in the LUT, allowing the system to efficiently retrieve and apply the appropriate matrix based on the current operating conditions. This technique ensures ease of implementation. However, a notable challenge arises when dealing with dynamic equations in the system model. Computing the inverse of the transfer function may lead to an improper transfer function (i.e. when the numerator's degree exceeds the denominator's). Such transfer functions are unrealisable in practice without additional techniques such as filtering or approximation. In addition, the implementation of LUT can also result in quantisation errors, computational delays, and memory constraints which could negatively impact system performance.

2.6 Simulation Results

The designed topology is a 1 kW bi-directional triple active bridge DC-DC converter with circuit parameters given in Table 2.8, following [111], with slight adjustments to the main parameters. The circuit in Fig. 2.1, is implemented in the MATLAB/SIMULINK software environment along with the PI-based control schemes shown in Fig.2.6 and

Fig.2.7a-c. The controller gains are tuned and selected for both the current and voltage loops, as listed in Table 2.9 . The components are all referred to the primary side.

The cross-coupling effect can be seen as a disturbance on a port when there is an intended or unintended change at the other corresponding ports. Firstly, the graph in Fig.2.8 shows the measured steady-state operation results of the midpoint square-wave voltages and inductor currents at each port. The shapes of i_3 and i_2 are trapezoidal following the same analogy as a DAB converter. However, the main supply port i_1 is not trapezoidal because it complements the trapezoidal-shaped currents of the other ports. Furthermore, two scenarios are created to test the performance of the decoupling techniques. Three step changes are introduced to the current control loop at specific times to create scenario 1. There is a change in the power supplied by the DE port from -200 W to -1000 W, -1000 W to -600 W, and -600 W to -750 W as shown in Fig.2.9 . In Scenario 2, an increase in the power absorbed in the EL from 0 W to 1000 W is introduced, and a drop in the load demand is made from 1000 W to 350 W and 350 W to 100 W, as shown in Fig.2.10.

Table 2.8: Circuit design parameters

Description	Parameter
DE Voltage	46 V
EL Voltage	73 V
BT Voltage	560 V
Leakage Inductance 1	0.75 mH
Leakage Inductance 2	1 µH
Leakage Inductance 3	24 µH
Switching frequency	15 kHz
Transformer Turns Ratio (1)	0.08
Transformer Turns Ratio (2)	0.13

Table 2.9: Selected proportional and integral gains

	Proportional gain	Integral gain
PI control without decoupling technique	0.05	2000
Inverse Matrix decoupling technique	5	8000
Simplified decoupling technique	1	1200
Inverted decoupling technique	0.8	800

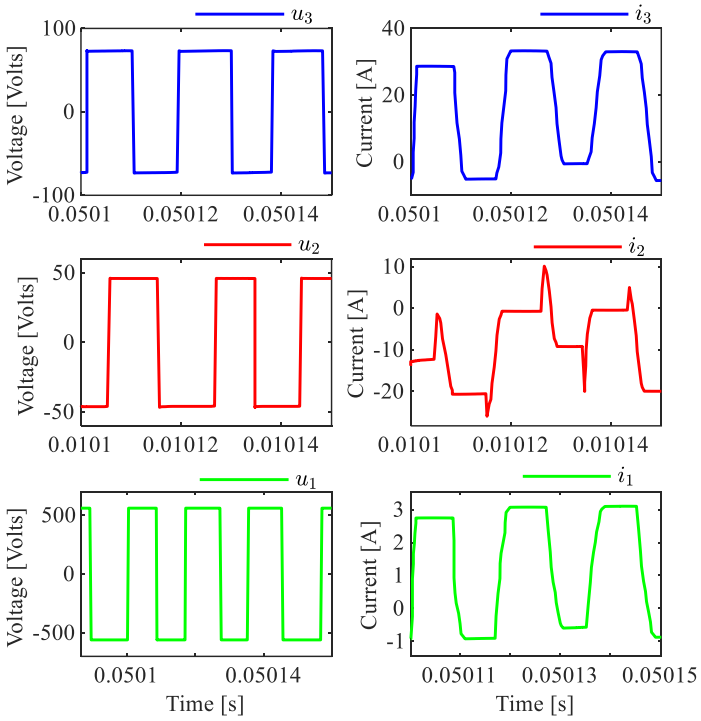

Fig.2.8: Bridge voltages and leakage inductance currents at steady state.

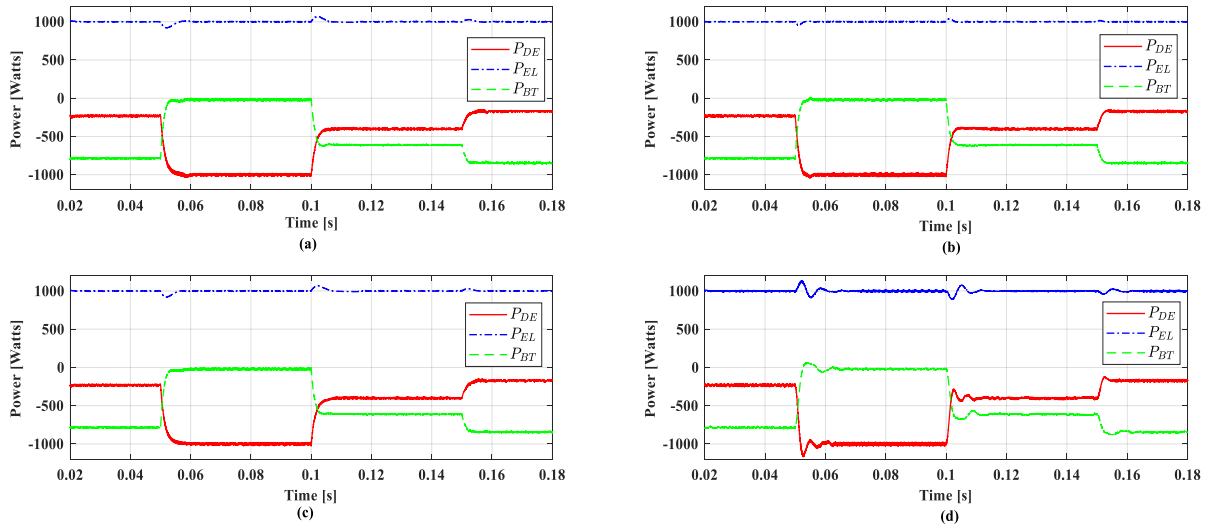

Fig.2.9: Power flow plots showing deviations on P_{EL} at step changes of P_{DE} at 0.05s, 0.1s and 0.15s: (a) Simplified decoupling technique (b) Inverse decoupling technique (c) Inverted decoupling technique and (d) Without decoupling control technique.

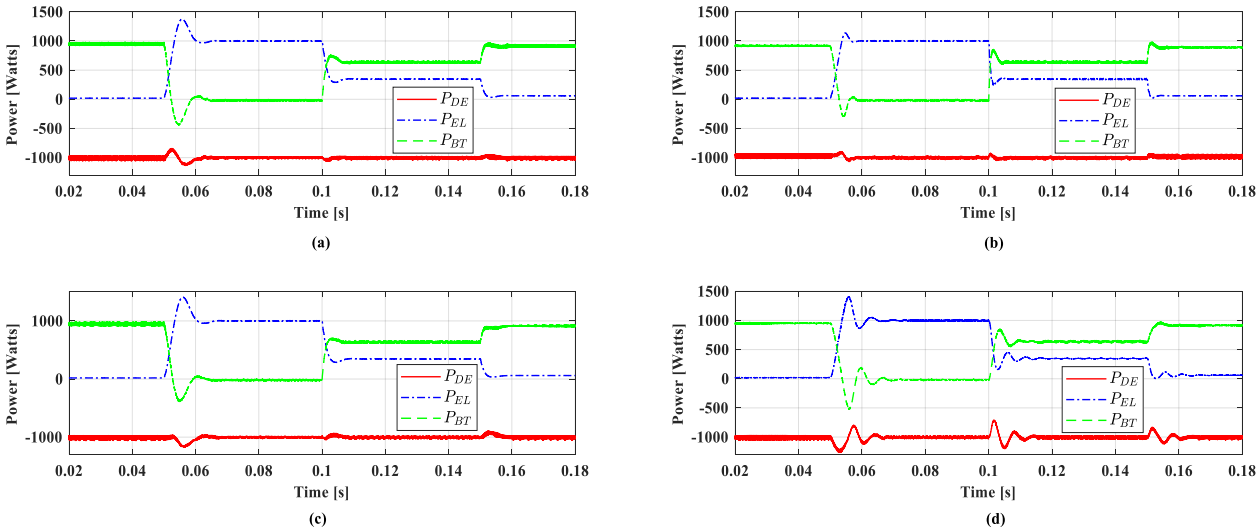

Fig.2.10: Power flow plots showing deviations on P_{DE} at step changes of P_{EL} at 0.05s, 0.1s and 0.15s: (a) Simplified decoupling technique (b) Inverse decoupling technique (c) Inverted decoupling technique and (d) Without decoupling control technique.

In each scenario, the peak power deviations are measured to ascertain the influence of the cross-coupling effect on each controlled port. The lower the peak power deviation from the nominal values at each control point, the better the decoupling performance.

With the implemented matrix-based decoupling control techniques, the peak power deviations (either overshoot or undershoot) are limited in each control technique compared

with the converter without decoupling control, as listed in Table 2.10. This shows that implementing decoupling control improves the dynamic performance of the system. The system stability and adequate power balancing can also be achieved, as shown in Fig.2.9 and Fig.2.10. In each scenario, the BT port acts as a slack port and is allowed to sink or source, thereby maintaining an adequate balance in the system. With this, better system performance can be achieved while also protecting the lifespan of the DE and EL and preventing false triggering of protective devices that are sensitive to overshoot and undershoot currents.

The average peak power deviation from the nominal operating value for the three step changes were calculated, as shown in Fig.2.11. The inverse decoupling matrix technique has a reduced peak power deviation compared with simplified and inverted decoupling control techniques in both scenarios.

Table 2.10: Peak power deviations considering different decoupling techniques

Technique	Time (s)	Scenario 1	Scenario 2
		Power Deviation (W)	Power Deviation (W)
Simplified	0.05	80	124
	0.1	64	59
	0.15	28	52
Inverse	0.05	45	93
	0.1	34	64
	0.15	16	56
Inverted	0.05	80	156
	0.1	68	59
	0.15	29	71
No decoupling	0.05	136	193
	0.1	77	276
	0.15	29	157

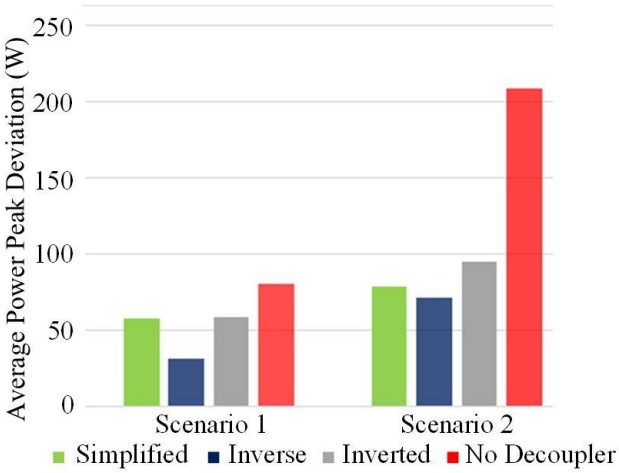

Fig.2.11: Peak power deviation.

2.7 Summary

This chapter presented an overview of FC and EL technologies in terms of their efficiencies, capacities, and operational voltages. The advantages and disadvantages of each technology were discussed. Among the various tightly coupled subsystems that constitute a hydrogen energy system, the role of the PEC was emphasised, as it governs the electrical interface and overall energy management between the FC, EL, and other system components. Based on the stringent and specific requirements that a suitable PEC topology must satisfy, such as low power ripple, high conversion ratio, and a need for galvanic isolation, a multiport isolated DC-DC converter was recommended. Two main areas of improvement were identified in the proposed topology, the cross-coupling effects and loss minimisation. A mathematical framework for analysing the cross-coupling effect was discussed, highlighting the influence of non-zero, non-diagonal elements in the system matrix. Matrix-based decoupling control techniques are widely recognised in the literature for their simplicity and ease of implementation. A detailed comparative analysis was carried out among three conventional matrix-based decoupling control techniques, namely, the inverse, simplified, and inverted matrix-based controls, against a PI control without decoupling. The results show that the inverse matrix-based decoupling control outperforms the others in terms of maximum power deviation from the nominal operating point during step changes in power flow. Under the two scenarios considered, the inverse matrix-based method exhibited a maximum power deviation of 5 % compared with 8 %, 8 %, and 14 % for the simplified, inverted, and no-decoupling techniques, respectively, in Scenario 1, and 10 % compared with 13 %, 16 %, and 27 % for the same methods in Scenario 2.

Chapter 3
Novel Model Reference-based Hybrid Decoupling Control Technique

As discussed in Chapter 2, Section 2.3, the multiport-isolated DC-DC converter has been identified as a suitable topology for the PEC interfacing system in a hydrogen energy system. The cross-coupling effects inherent in this topology pose a significant challenge to achieving optimal system performance. The previous chapter identifies the inverse matrix-based decoupling control to be more effective among the conventional matrix-based techniques. However, while the inverse matrix-based decoupling control is effective to a certain operating point, its decoupling effect remains incomplete. In this chapter, a novel model reference-based hybrid decoupling control technique is proposed, which combines the principles of matrix- and model reference-based decoupling to achieve improved system decoupling. The proposed method is validated through MATLAB/Simulink modelling and experimental results, and its performance is compared with other conventional decoupling control techniques in literature to highlight its advantages.

3.1 Background

The converter behaves as a Multi-Input Multi-Output (MIMO) system with coupled control loops. As discussed in Section 2.3 and in Table 2.6, decoupling approaches are broadly classified into hardware and software solutions (nonlinear and linear). In [112], [75] a multiport converter with inherent decoupling capability was proposed using low primary leakage inductance. However, its scalability to larger systems remains unproven, and implementation requires complex transformer design. A resonant capacitor on the transformer primary side, was introduced in [69], which reduced computational burden but failed to achieve effective decoupling across all operating regions. In [70] an addition of two switches to control coupling and force the converter to behave like a Single-Input Single-Output (SISO) system was made, although this increased switching losses. A varying winding configuration was designed in [74] to reduce coupling and ensure adequate power transfer, but analysing and restructuring transformer windings is challenging. Variable inductors [72] and electronic capacitors were also introduced in the resonant circuit to achieve decoupling while maintaining bidirectional operation. Hence, these hardware-based

approaches rely on additional components or structural modifications, which can increase cost, reduce power density, and add design complexity.

Nonlinear software-based decoupling control techniques have been proposed as alternatives to hardware modifications. For instance, a power decoupling configurable model predictive controller (MPC) was developed in [77], employing binary search and Newton iteration to predict DC currents. Decoupling was achieved by linking each virtual branch of the converter to its phase shifts. However, this technique is computationally intensive due to partial derivatives and Jacobi matrix inversions. A magnetically linked multiport converter controlled via MPC was introduced in [78], achieving good decoupling performance, although its steady state error exceeded that of simpler PI control. Similarly, flatness based decoupling control was applied to an FC hybrid source in [76], transforming the nonlinear problem into trajectory planning and tracking by leveraging system flatness to design feedforward and feedback control laws. However, model discrepancies may lead to instability. In addition, metaheuristic approaches such as artificial neural network based decoupling control have been explored in [79], [80], and [113] although their performance depends heavily on the quality and range of training data. Frequency domain techniques such as Fourier series expansion were proposed in [81]. Although effective, they require accurate measurement of AC components in multiwinding transformers, posing practical implementation challenges. Overall, these nonlinear approaches remain computationally intensive and difficult to implement in practice.

Consequently, linear software techniques for decoupling control have been extensively studied to address the limitations of non-linear software-based decoupling techniques. For example, a feedback linearisation-based controller was implemented in [82], [114], to suppress cross-coupling effects, nevertheless, improper handling of the non-linear inversion in the control loop may lead to performance degradation. A polar coordinate-based decoupling control technique was developed in [83]. The polar coordinate technique determines the phase shifts using the sum and difference of the transmission powers to suppress the cross-coupling. However, its operating region is constrained and requires a conditional branching strategy for expansion. An adaptive perturb-and-observe (P&O) controller, proposed to track the minimum point current, was developed in [85]. Although this controller shows promising results, the P&O algorithm introduces an additional computational burden on the system. Similarly, a single-input, single-output (SISO) system

with different bandwidth selections was examined in [86], where high-bandwidth loops enhance transient phase detection, aiding decoupling, and lower-bandwidth loops exhibit poor anti-interference properties. Decoupling matrices are another common approach. A frequency domain modelling technique was applied in [115] to develop a decoupling matrix-based PI controller, yielding three lower-order AC equivalents; however, these AC equivalents may reintroduce measurement and control complexities, limiting practical implementation. A plant transfer matrix with a decoupling matrix, pre-calculated and stored in lookup tables (LUTs), was introduced in [87], [68], and [107], and a comparative analysis of three of these decoupling matrices was conducted in [116], identifying the inverse decoupling matrix as superior in performance compared to others. Furthermore, hybrid approaches that combine multiple strategies have been proposed. For example, in [117], a decoupling control technique using a proportional-derivative controller, MPC, and fuzzy compensation control achieved a reduced cross-coupling effect; however, the combination's high computational demands may hinder real-time performance and increase implementation costs. In [118], an approach combining decoupling matrices, bandwidth selection, and feedforward current achieved effective decoupling, however, its effectiveness was limited under asymmetrical loading across ports.

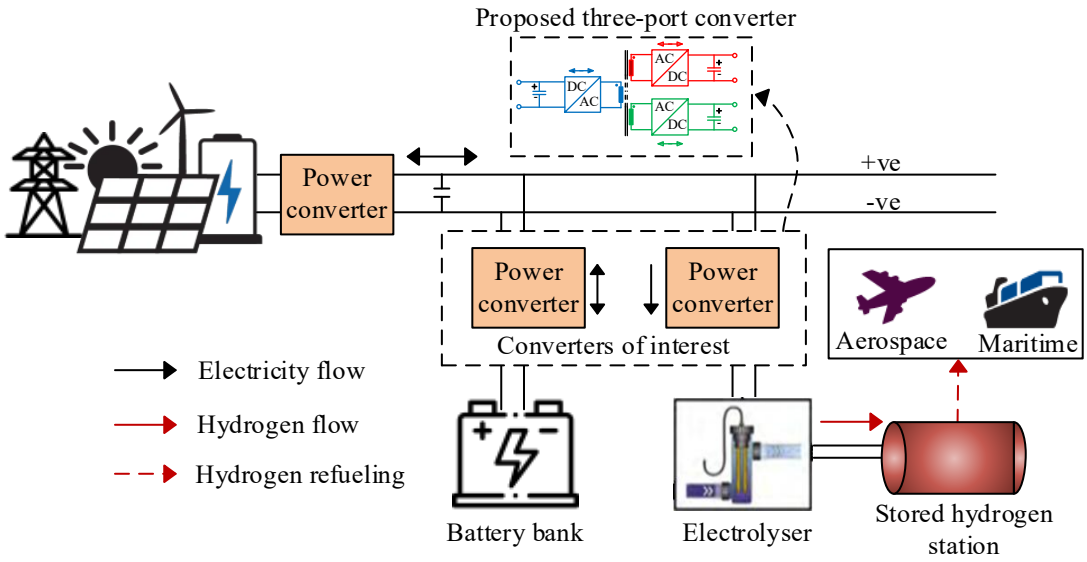

Fig.3.1: Onshore hydrogen production with DE connection.

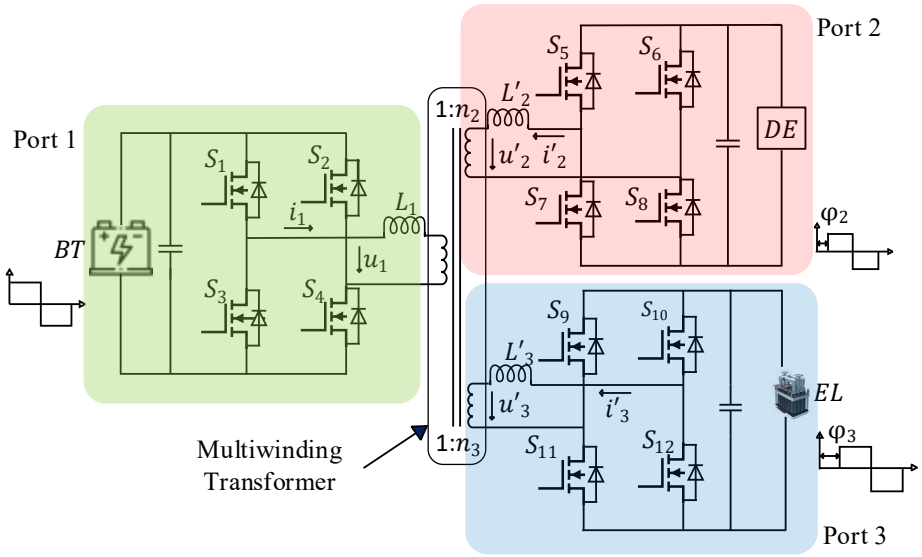

Fig.3.2: Topology of multiport-isolated DC-DC converter.

Fig.3.1 illustrates the "converters of interest" within the hydrogen energy system configuration, which are to be replaced by the multiport-isolated DC-DC converter as seen in Fig.3.2. This converter is deployed in an onshore hydrogen production facility with a distributed energy (DE) source connection.

3.2 Novel Model Reference-based Hybrid Decoupling Control Technique

As discussed, while these software approaches, matrix-based decoupling control techniques, demonstrate some success in mitigating cross-coupling effects; they often involve complex computations, particularly in larger systems. The conventional matrix-based decoupling control relies on a plant matrix derived at a particular operating point. Since the TAB parameters vary with operating conditions, a fixed matrix may not perfectly represent the system over the entire operating region, leading to incomplete decoupling. Multiple matrices are often pre-calculated and stored in LUTs, which increases memory and implementation complexity.

Hence, a novel software-based decoupling control technique is proposed to address these challenges. The proposed technique features a model reference-based decoupling control and hybrid decoupling control (which combines the strengths of both model reference-based decoupling control and a decoupling matrix). The technique is designed to

achieve excellent decoupling performance across a wider operating region. The main contributions of this technique are summarised as follows:

- Proposing a novel software-based decoupling control technique that eliminates the reliance on LUTs, thereby significantly reducing memory requirements.
- Developing a model reference-based decoupling control technique that minimises the error between the output of an ideal decoupling reference model and the actual plant, thereby enhancing control accuracy.
- Proposing a hybrid decoupling control structure that integrates a decoupling matrix into the model reference-based framework, synergises their strengths to achieve robust decoupling and mitigates cross-coupling effects across a wider operating region.

The proposed decoupling control is explained in this section, which includes a novel model reference-based decoupling control technique. The novel model reference-based decoupling control is modified to a hybrid decoupling control which incorporates a decoupling matrix H in the decoupling control structure.

3.2.1 Proposed Model Reference-based Decoupling Control

The degree of TAB coupling is determined by the ratio of non-diagonal elements (coupling terms) to diagonal elements. For complete decoupling, the coupling terms are equal to zero. However, this cannot be achieved practically. Hence, it is desirable to ensure that the TAB operates such that the non-diagonal elements approach zero.

$$\begin{bmatrix} I_{DE,ideal} \\ I_{EL,ideal} \end{bmatrix} = \begin{bmatrix} G_{11} & 0 \\ 0 & G_{22} \end{bmatrix} \begin{bmatrix} \varphi_2 \\ \varphi_3 \end{bmatrix} \tag{3.1}$$

Equation (3.1) shows a diagonal matrix comprising the uncoupling terms, which is equivalent to an ideal decoupling model. This model is subsequently employed as a reference model for decoupling control. Thus, the deviation of the TAB outputs from the ideal decoupling reference model (3.1) is used to mitigate the cross-coupling effect. The proposed model reference-based decoupling control scheme is illustrated in Fig.3.3. Following (2.12)-

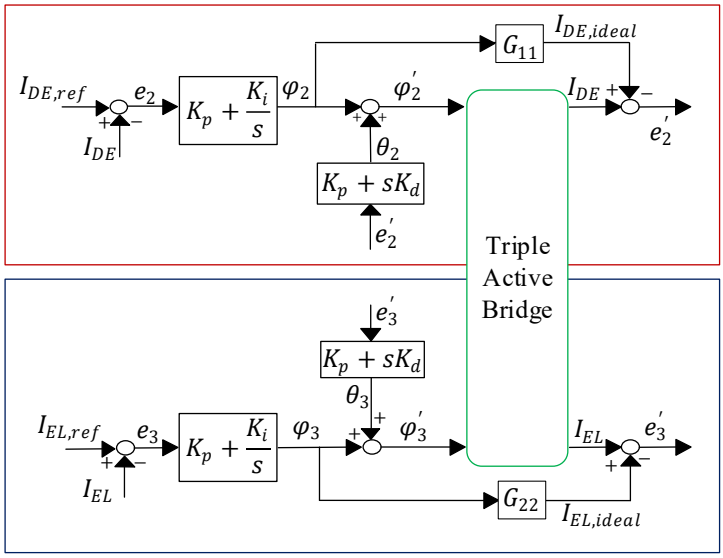

Fig.3.3: Proposed model reference-based decoupling control scheme.

(2.13) and (2.14)-(2.15), a proportional integral (PI) controller is implemented to generate the intermediate control inputs as follows:

$$\varphi_2 = K_P e_2 + \frac{K_I}{s} e_2 \tag{3.2}$$

$$\varphi_3 = K_P e_3 + \frac{K_I}{s} e_3 \tag{3.3}$$

where,

$$e_2 = I_{DE,ref} - I_{DE} \tag{3.4}$$

$$e_3 = I_{EL,ref} - I_{EL} \tag{3.5}$$

where, $I_{DE,ref}$ is the current reference in the DE port, which is represented by a voltage source, and $I_{EL,ref}$ is the current reference in the EL port, which is represented by a resistive load, for simplicity of analysis. Applying (2.13), (3.2) and (3.3) yields the actual current outputs from ports 2 and 3, respectively, as follows in (3.6) and (3.7):

$$I_{DE} = G_{11}\left(K_P e_2 + \frac{K_I}{s} e_2\right) + G_{12}\varphi_3 \tag{3.6}$$

$$I_{EL} = G_{21}\varphi_2 + G_{22}\left(K_P e_3 + \frac{K_I}{s} e_3\right) \tag{3.7}$$

As shown in Fig.3.3, the errors, e_2 and e_3, in (3.4) and (3.5) represent the error between the desired set-point value of the system and the output of the plant in each port.

This error is kept minimal by using a simple PI controller. However, the ideal decoupling reference model will evolve based on the PI control laws (3.1) − (3.3) to yield:

$$\mathrm{I_{DE,ideal}} = \mathrm{G_{11}}\left(\mathrm{K_P e_2} + \frac{\mathrm{K_I}}{\mathrm{s}}\mathrm{e_2}\right) \tag{3.8}$$

$$\mathrm{I_{EL,ideal}} = \mathrm{G_{22}}\left(\mathrm{K_P e_3} + \frac{\mathrm{K_I}}{\mathrm{s}}\mathrm{e_3}\right) \tag{3.9}$$

The outputs of the ideal decoupling reference model are compared with the actual current outputs of the TAB at each port. From (3.6)− (3.9), the difference between the ideal decoupling reference model output and plant output is related to the coupling terms.

The errors, e_2' and e_3', as seen in (3.10), (3.11) and Fig.3.3 are used to suppress the coupling terms in the system, which is similar to an internal disturbance that affects the precise independent control of each loop.

$$e_2' = I_{DE} - I_{DE,ideal} \tag{3.10}$$

$$e_3' = I_{EL} - I_{EL,ideal} \tag{3.11}$$

Consequently, a simple proportional (P) or proportional-derivative (PD) controller is sufficient for the control. A PD is used for the error, e_2' and e_3' to mitigate the sensitivity of the system to internal disturbances, and to enhance the robustness of the control system. However, an excessive derivative gain can render the system sensitive to the measurement noise. Therefore, a proper and careful tuning of the controller is necessary.

Based on the deviation of the TAB output from the ideal decoupling reference model, additional control signals θ_2 and θ_3 are generated, as given by (3.12) and (3.13) respectively.

$$\theta_2 = e_2'\,(K_p + sK_d) \tag{3.12}$$

$$\theta_3 = e_3'\,(K_p + sK_d) \tag{3.13}$$

This limits the influence of the coupling terms on the intermediate control inputs φ_2 and φ_3. By driving the system to be as close as possible to the ideal decoupling reference model, the intermediate control inputs are modified to an actual control input. The resulting actual control inputs are given as:

$$\varphi_2' = \varphi_2 + \theta_2 \tag{3.14}$$

$$\varphi_3' = \varphi_3 + \theta_3 \tag{3.15}$$

Therefore, the actual control inputs (3.14) and (3.15) not only help achieve tracking control but also ensure mitigation of the cross-coupling effect.

3.2.2 Proposed Hybrid Decoupling Control

To ensure a more robust system, a decoupling matrix H is incorporated into the model reference-based decoupling control technique, as shown in Fig.3.4. The implemented decoupling matrix is the inverse of matrix G, is as shown in (3.16):

$$H = \begin{bmatrix} H_{11} & H_{12} \\ H_{21} & H_{22} \end{bmatrix} \tag{3.16}$$

Hence, considering the decoupling matrix, the modified ideal decoupling reference model with uncoupling terms is given in (3.17).

$$\begin{bmatrix} I_{DE,ideal} \\ I_{EL,ideal} \end{bmatrix} = \begin{bmatrix} G_{11}H_{11} & 0 \\ 0 & G_{22}H_{22} \end{bmatrix} \begin{bmatrix} r_2 \\ r_3 \end{bmatrix} \tag{3.17}$$

A PI controller is implemented to derive the medium variations r_2 and r_3 , as depicted in Fig.3.4, calculated by (3.18) and (3.19):

$$r_2 = K_P e_2 + \frac{K_I}{s} e_2 \tag{3.18}$$

$$r_3 = K_P e_3 + \frac{K_I}{s} e_3 \tag{3.19}$$

where, e_2 and e_3 follows from the same expression (3.4) and (3.5).

Consequently, the modified intermediate control inputs φ_2 and φ_3, are generated as follows in (3.20) and (3.21), respectively:

$$\varphi_2 = H_{11} r_2 + H_{12} r_3 \tag{3.20}$$

$$\varphi_3 = H_{21} r_2 + H_{22} r_3 \tag{3.21}$$

Thus, the modified control-output relationship after simplification is expressed as in (3.22) and (3.23):

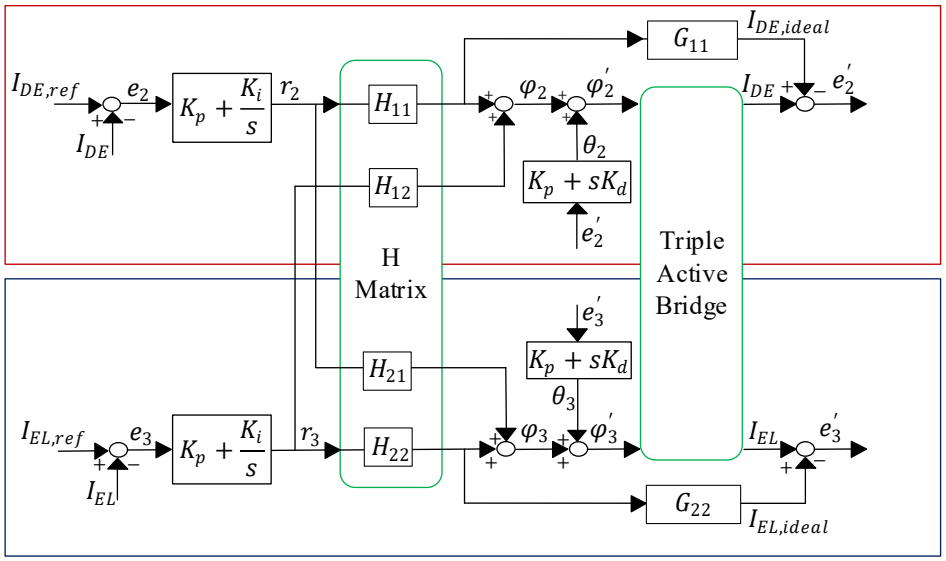

Fig.3.4: Proposed hybrid decoupling control scheme.

$$I_{DE} = G_{11}H_{11}\left(K_P e_2 + \frac{K_I}{s}e_2\right) + (G_{11}H_{12}r_3 + G_{12}\varphi_3) \tag{3.22}$$

$$I_{EL} = (G_{21}\varphi_2 + G_{22}H_{21}r_2) + G_{22}H_{22}\left(K_P e_3 + \frac{K_I}{s}e_3\right) \tag{3.23}$$

The modified ideal decoupling reference model evolves based on medium variations by substituting (3.18) and (3.19) into (3.17) yielding (3.24) and (3.25).

$$I_{DE,ideal} = G_{11}H_{11}\left(K_P e_2 + \frac{K_I}{s}e_2\right) \tag{3.24}$$

$$I_{EL,ideal} = G_{22}H_{22}\left(K_P e_3 + \frac{K_I}{s}e_3\right) \tag{3.25}$$

Following mathematically (3.10) − (3.13) and as shown in Fig.3.4, implementing a PD controller, the actual control inputs that will achieve set point tracking and ensure mitigation of cross-coupling effect are given as follows in (3.26) and (3.27).

$$\varphi'_2 = \varphi_2 + \theta_2 \tag{3.26}$$

$$\varphi'_3 = \varphi_3 + \theta_3 \tag{3.27}$$

The theoretical analysis of the proposed decoupling controller highlights its effectiveness in mitigating the cross-coupling effects. However, practical implementation

requires attention to a few key aspects. Namely, this decoupling control technique introduces additional controller gains, which, while beneficial for increased flexibility, require precise tuning to achieve an optimal performance. Tuning the PD controller, particularly the derivative gain, can influence electromagnetic interference (EMI). To balance the improved control performance with noise suppression, cautious tuning of the derivative term is recommended to minimise any high-frequency noise that could contribute to EMI. Additionally, the converter employs MOSFETs as switching devices, which are selected for their faster switching speeds and lower switching losses compared with IGBTs. In terms of thermal management, appropriately sized heat sinks are integrated to ensure efficient heat dissipation and reliable operation of MOSFETs. These considerations collectively enhance the practical feasibility and robustness of the proposed decoupling controller, making it a reliable solution for mitigating cross-coupling effects in multiport isolated DC-DC converters.

3.3 Simulation Results

Simulations are conducted using the specifications listed in Table 3.1 to verify the effectiveness of the proposed decoupling control technique. The circuit is modelled in the SIMULINK/MATLAB software environment, with the control schematics implemented, as shown in Fig.3.3 and Fig.3.4. The controller gains were selected with trial-and-error.

Table 3.1: Circuit design parameters

Description	Symbol	Unit	Ports		
			#1	#2	#3
Voltage Rating	V_{BT}, V'_{DE}, V'_{EL}	V	560	46	73
Leakage Inductance	L_1, L'_2, L'_3	µH	780	4.992	13.18
Switching frequency	f_s	kHz	15	15	15
Transformer Turns Ratio	n_2, n_3	-	1	0.08	0.13
Controller Gains (Model reference-based decoupling control, hybrid decoupling control, inverse matrix decoupling control, and control without decoupling methodology)	K_p	-	-	15	10
	K_i	-	-	6000	8000
Model reference-based decoupling control, hybrid decoupling control	K_d	-	-	0.001	0.00085
	K_p	-	-	0.01	0.001

The performance of the proposed model reference-based decoupling control and hybrid decoupling control techniques are shown in Fig.3.5 and Fig.3.6, respectively. These figures highlight the effectiveness of the controllers in mitigating cross-coupling effects, observed as disturbances in the form of power deviations (overshoot or undershoot) at the corresponding port in response to intended or unintended changes in the power supply or power absorbed by other ports, and in maintaining a stable power transfer across different ports under worst case conditions. Two scenarios are simulated to illustrate the controller performance under step changes in the power transfer:

1. Scenario 1 (Fig.3.5a and Fig.3.6a) examines changes in the power supply at the DE port (P_{DE}). Step changes are applied at 0.05 s, 0.1 s, and 0.15 s, with transitions from -200 W to -1000 W, -1000 W to -600 W, and -600 W to -750 W, respectively, while maintaining a constant power absorption of 1000 W at the EL port (P_{EL}). The BT port (P_{BT}) acts as a slack bus, adjusting to balance power transfer.
2. Scenario 2 (Fig.3.5b and Fig.3.6b) examines changes in the power absorbed at the EL port (P_{EL}). Step changes occur at the same time intervals, with the power absorbed by P_{EL} transitioning from 0 W to 1000 W, then from 1000 W to 350 W, and finally from 350 W to 100 W, while maintaining a constant power supply of 1000 W at the DE port (P_{DE}). The BT port (P_{BT}) continues to act as the slack bus in this scenario.

Using the model reference-based decoupling control shown in Fig.3.3, the controller minimises the cross-coupling effect by comparing the output of the decoupling reference model with the plant output. This comparison allows the controller to interpret the error as a coupling term and to suppress it. As shown in Fig.3.5a (scenario 1), this technique results in negligible power overshoot from the nominal value at the EL port. In scenario 2 (Fig.3.5b), the model reference-based control reduces the cross-coupling effect, with a maximum undershoot of 6 % from the nominal value occurring at the 0.05 s step change.

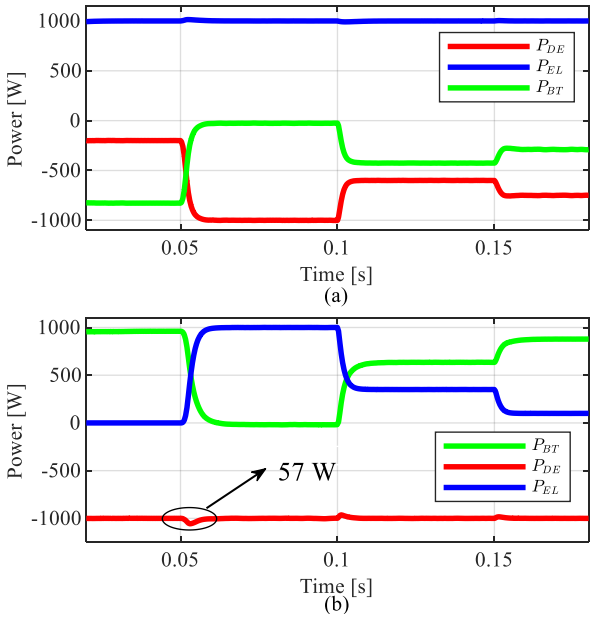

Fig.3.5: Power transfer between ports using the proposed model reference-based decoupling control: (a) power absorbed by the EL when step changes are applied to the power supply by the DE and BT ports, and (b) power supply by the DE ports when step changes are applied to the power absorbed in the EL and BT ports.

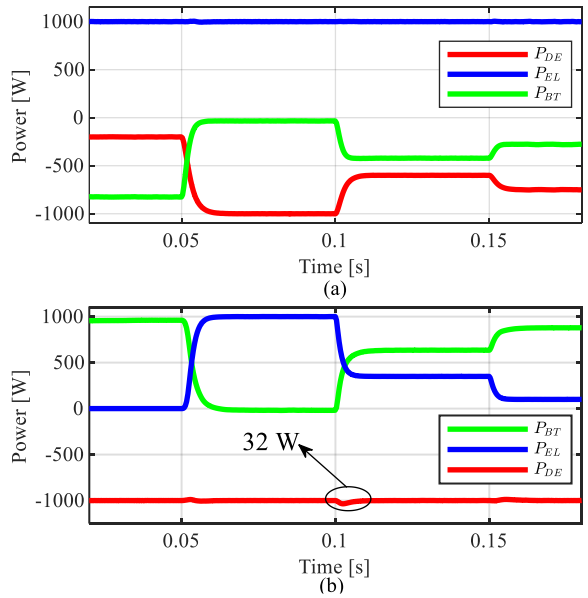

Fig.3.6: Power transfer between ports using the proposed hybrid decoupling control: (a) power absorbed by the EL when step changes are applied to the power supply by the DE and BT ports, and (b) power supply by the DE ports when step changes are applied to the power absorbed in the EL and BT ports.

In comparison, the proposed hybrid decoupling control in Fig.3.4 further improves the performance with a negligible power overshoot or undershoot in scenario 1 (Fig.3.6a). In scenario 2 (Fig.3.6b), the hybrid decoupling control shows enhanced robustness, with the worst case power undershoot reduced to 3 % at the 0.1 s step change.

Table 3.2 provides a qualitative comparative overview of decoupling control techniques for multiport-isolated DC-DC converters from both software and hardware perspectives, highlighting the key improvements offered by the proposed hybrid decoupling control. To further demonstrate the superiority of the proposed technique, it is evaluated through simulations alongside a matrix-based decoupling control, the conventional inverse matrix-based decoupling control illustrated in [68] and a control without decoupling. The results are as shown in Fig.3.7 and Fig.3.8 for each scenario, respectively. Fig.3.7 and Fig.3.8 specifically extract the response of the ports susceptible to power overshoot and undershoot due to step changes on other ports, as illustrated in Fig.3.5 and Fig.3.6, for each controller type, providing a clearer view.

In scenario 1, the proposed hybrid decoupling control exhibits excellent decoupling, with negligible power overshoot/undershoot, as shown in Fig.3.7a. In contrast, the inverse matrix decoupling control experiences a worst-case power undershoot of 3 % from the nominal value at the 0.05 s step change, as shown in Fig.3.7b. Meanwhile, the control without decoupling methodology demonstrates a worst-case power overshoot of 8 % at the 0.05 s step change, as seen in Fig.3.7c.

Furthermore, in scenario 2, the performance difference is even more pronounced. The proposed hybrid decoupling control technique more effectively suppresses the cross-coupling effect, with a reduced power undershoot of only 3 % at the 0.1 s step change, as depicted in Fig.3.8a. Whereas, as shown in Fig.3.8b and Fig.3.8c, the inverse matrix decoupling control and the control without decoupling methodology experience worst-case power undershoots of 8 % and 9 %, respectively.

Table 3.2: Overview of multiport-isolated DC-DC converter decoupling techniques

Details of operation	Hardware solution		Software solution		
	[70]	[69]	[84]	[68]	Proposed technique
Additional component	Two switches /low primary inductance	Resonant Capacitor	None	None	None
Estimation error	None	None	Yes	None	None
Ease of implementation	Medium	Low	High	Medium	Medium
Extra data storage	Low	Low	Medium	High	Low
Power operational region	Medium	Narrow	Medium	Narrow	Wide
Hardware Complexity	High	Medium	Low	Low	Low
Converter Configuration	Symmetric	Asymmetric	Symmetric/ Asymmetric	Asymmetric	Asymmetric

In terms of efficiency, the conduction losses in the system are calculated using $P_c = I_{rms}^2 R_{on}$ where, R_{on} represents the on-state resistance of each switch. These losses are directly influenced by the root-mean-square current through the switches. With the proposed hybrid decoupling control, the system achieves an end-to-end efficiency of 91.80 %, compared with 89.75 % for the conventional inverse matrix decoupling control and 88 % for the control without decoupling. These results were obtained under a constant 1000 W power supply with step changes applied to the EL port, as shown in Fig.3.6b, and replicated across all decoupling controllers under investigation. This scenario represents the worst-case operating condition, highlighting the robustness of the proposed control technique.

These results demonstrate the superior performance of the hybrid decoupling control technique in reducing the cross-coupling effects and maintaining stable power levels across ports under varying conditions.

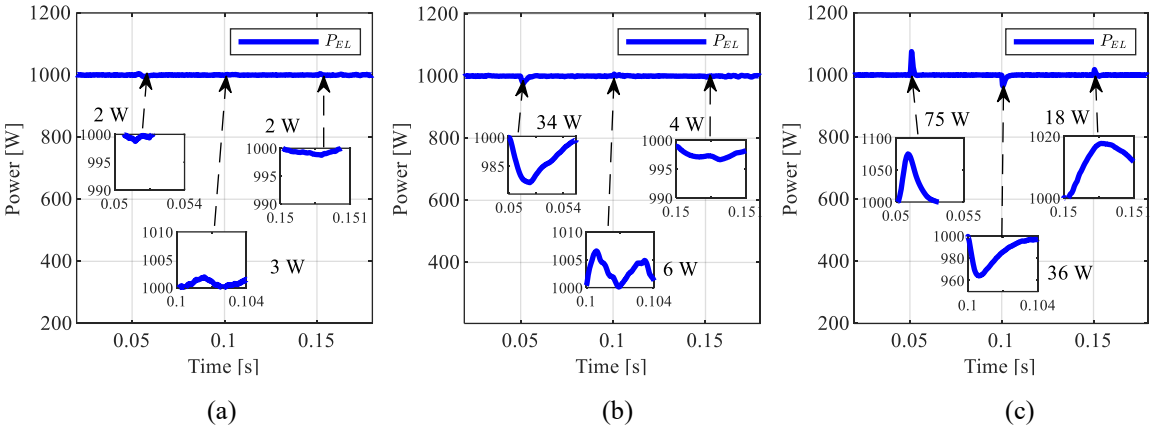

Fig.3.7: Power absorbed by EL when step changes are applied to power supply in DE and BT ports for (a) proposed hybrid decoupling control, (b) inverse matrix decoupling control, and (c) control without decoupling methodology.

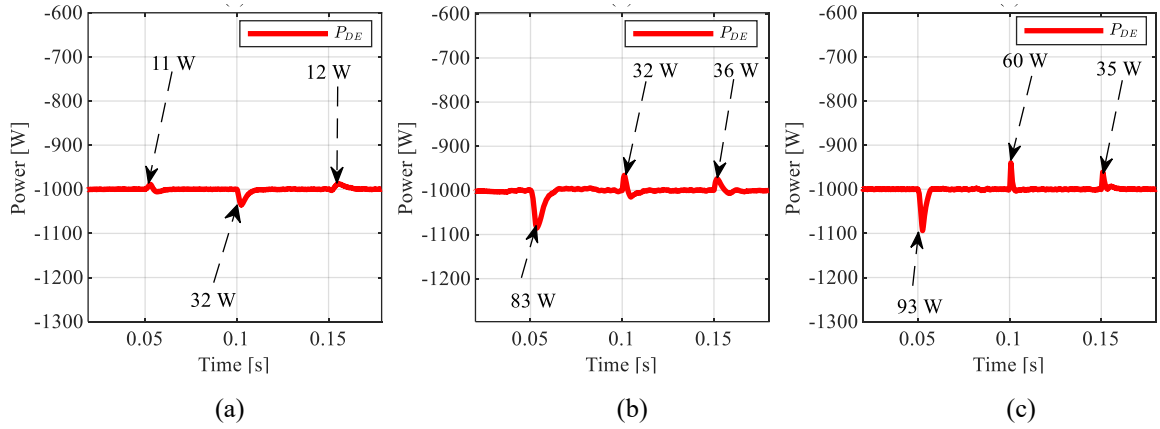

Fig.3.8: Power supply from DE port when step changes are applied to power absorbed in EL and BT ports for (a) hybrid decoupling control, (b) inverse matrix decoupling control, and (c) control without decoupling methodology.

3.4 Experimental Validation

To further validate the proposed controller and align the theoretical analysis with the experimental results, a proof-of-concept circuit, as depicted in Fig.3.9 is developed. The parameters of the experimental circuit are scaled down from those used in simulations. The rated power for this experimental setup is 380 W, operating at a switching frequency of 20 kHz. The leakage inductances of L_1, L_2 and L_3 are 50 µH, 48 µH and 49 µH respectively. The transformer core material utilised is N87, with dimensions R 50/30/20, with turns ratios of 17:15:11.

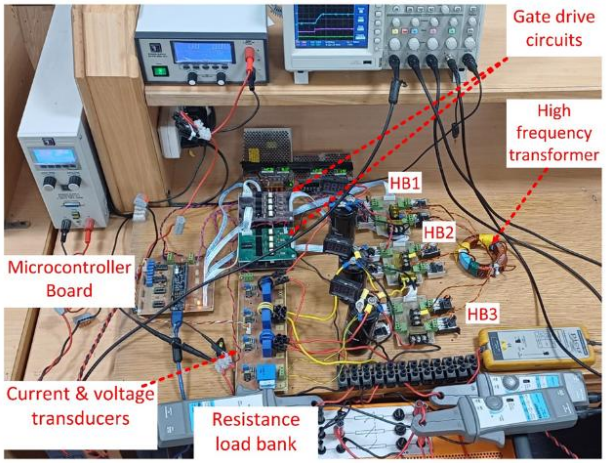

Fig.3.9: Experimental test rig.

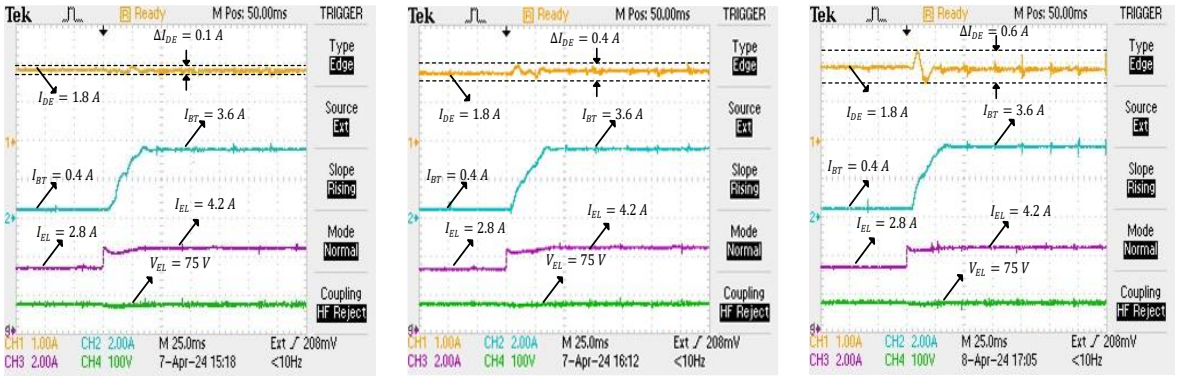

Fig.3.10: Experimental results showing power supply from the DE port when there is an EL port change from 2.8 A to 4.2 A (a) hybrid decoupling control, (b) inverse matrix decoupling control, and (c) control without decoupling.

The experiment was conducted to simulate scenario 2 by observing the impact of the EL port variation while keeping the DE port supplying a steady current and the BT port serving as the slack bus to compensate for the changes and maintain the system balance. Fig.3.10 illustrates the experiment conducted using three control techniques: the proposed hybrid decoupling control, the conventional inverse matrix decoupling control, as illustrated in [68], and the control without decoupling methodology. The current in the EL varied from 2.8 A to 4.2 A, marking a 50 % increase in load demand. This variation led to a proportional change in the BT current, stepping it from 0.4 A to 3.6 A. Fig.3.10a, indicates a deviation of 0.1 A in the DE port, representing a 5 % deviation from the nominal value with the hybrid decoupling control technique. In contrast, with the inverse matrix decoupling control and control without decoupling methodology shown in Fig.3.10b and Fig.3.10c, respectively,

there are deviations of 0.4 A and 0.6 A, corresponding to 22 % and 33 % deviations from the nominal value.

3.5 Summary

To further mitigate the cross-coupling effects in a multiport-isolated DC-DC converter, a model reference-based decoupling control has been proposed. Using an ideal decoupling reference model, a mathematical formulation was developed that addresses and suppresses cross-coupling effects by minimising the error between the output of the model and the actual plant. Additionally, a hybrid model reference-based decoupling control technique that integrates a decoupling matrix into the model reference-based decoupling structure showed superior decoupling control performance across the two simulated scenarios, with a consistent response under variable load conditions. Compared with conventional inverse matrix-based decoupling control and control without decoupling methodology, the proposed technique performs well in a wider operating region, achieving a worst-case power deviation of only 3 %, whereas conventional techniques have power deviations of approximately 8 – 10 %. Furthermore, the proposed technique achieved a 2.05 % efficiency improvement over conventional inverse matrix decoupling control in the worst-case scenario. A 380 W proof-of-concept validates the efficacy of the proposed decoupling control technique, demonstrating its practical feasibility. These results underscore the potential of the proposed technique for improving decoupling control in HESS applications by improving on the limitations associated with conventional decoupling control techniques.

Chapter 4

Optimised Linear Active Disturbance Rejection Control

The previous chapter introduced a novel model reference-based hybrid decoupling control technique to mitigate cross-coupling effects in a multiport-isolated DC-DC converter. Building on that foundation, this chapter examines a conventional control approach that reduces dependence on specific system parameters for decoupling. However, this controller is susceptible to estimation errors. To address this limitation, an improved version of the controller is proposed to minimise estimation errors and simplify the overall control design. A detailed mathematical formulation of the proposed method is presented, followed by simulation and experimental validation to demonstrate its effectiveness in suppressing cross-coupling effects.

4.1 Background

The previous decoupling controls relies on a well-defined knowledge of system parameters during the design of the decoupling matrices and reference model. However, system parameters may fluctuate during operation. Therefore, it is desirable to develop decoupling control techniques that minimise reliance on detailed system parameter information, reduce control complexity, and account for the internal dynamic characteristics of the converter.

To achieve effective decoupling control in this application, linear active disturbance rejection controller (LADRC) is explored. LADRC is recognised as a promising controller due to its ability to estimate and reject both external and internal disturbances effectively. It operates with minimal system parameter information, typically requiring knowledge of only the plant order, and involves low computational requirements [119], [120]. These characteristics make LADRC an ideal choice for achieving decoupling control.

In the field of power electronics, LADRC has demonstrated effectiveness across a variety of converter topologies as seen in [121], [122] and [123]. Applications include T-type three-level converters, three-phase voltage source rectifiers, and multilevel interleaved bidirectional DC-DC converters. For instance, LADRC was successfully employed in buck converters to mitigate disturbances and ensure robust performance [124], [125]. In isolated

converter applications, LADRC has shown significant promise. Decoupling control technique based on LADRC was developed for LLC resonant converters in electric vehicle systems, effectively enhancing dynamic performance and disturbance rejection [126]. Similarly, in dual active bridge (DAB) converters, LADRC with a linear extemded state observer was implemented to achieve real-time decoupling control, mitigating both internal and external disturbances [127].

To further enhance LADRC's capabilities, integration with linear extended state observers (LESO) has been explored. For multiport-isolated DC-DC converters, a LESO-based LADRC technique incorporating input matrix diagonalisation was developed for decoupling control in quad-active bridge converters [84]. This technique yielded robust system performance with improved decoupling characteristics. Additionally, a high-bandwidth LESO was used to design a decentralised, model-independent LADRC for multiport converters, achieving significant improvements in control performance [128].

Despite these advancements, challenges remain. The effectiveness of LADRC-based control is highly dependent on accurate estimation by the LESO. Estimation errors in the observers can lead to suboptimal performance, particularly in multiport-isolated DC-DC converters. Furthermore, gain tuning for LADRC remains a critical issue. Existing literature offers various manual gain-tuning techniques as seen in [129], [130] and [131], but these are often subjective and require considerable design effort. As a result, they may fail to achieve optimal decoupling control. Selecting appropriate controller gains is crucial for ensuring effective decoupling control, particularly in multiport-isolated converters. Properly tuned gains not only enhance control signal accuracy but also ensure robust performance across varying operating conditions.

Hence, an LADRC gain auto-tuning mechanism is essential for simplifying the decoupling control design. This chapter proposes utilising particle swarm optimisation (PSO) to determine the optimum gains of LADRC. The main contributions are as follows.

- Introduction of an offline PSO to determine the optimal gains of the controller without imposing additional computational burden on the controller.
- The identified optimal gains simplify the controller design process, bypassing the subjective nature of manual tuning techniques.

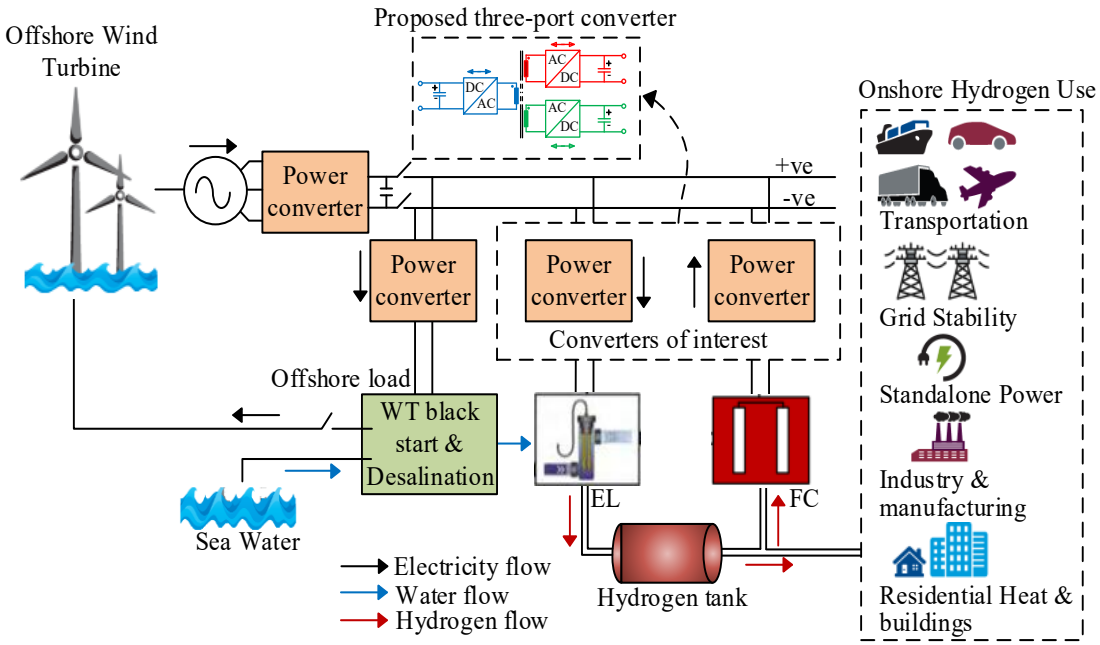

Fig. 4.1: Offshore wind farm hydrogen energy storage system. Inset: Triple active bridge topology.

- The determined gains are optimised to minimise the observer's estimation error, ensuring effective decoupling control performance and maintaining minimal estimation inaccuracies.

The optimised gain LADRC consists of a controller with a high-bandwidth LESO, and gain optimisation based on PSO.

In this chapter, the practical application of the proposed converter is demonstrated in an offshore wind farm-based hydrogen energy storage system, as illustrated in Fig. 4.1. In this configuration, the FC serves as a backup power source to meet on-turbine electricity demands, such as desalination units and wind turbine black-start operations, ensuring self-sufficiency. The hydrogen produced offshore is transported through buried pipelines to onshore facilities, thereby reducing the need for export power cables. Onshore, the hydrogen can be utilised for a wide range of applications, including grid stability support, transportation, standalone power generation, industrial and manufacturing processes, and residential heating. This arrangement enables an integrated and comprehensive approach to hydrogen utilisation. In this context, the “converters of interest” are replaced with a multiport-isolated DC-DC converter that interfaces the wind turbine (WT), electrolyser (EL), and fuel cell (FC).

4.2 Decoupling Control using LADRC

LADRC is a relatively new control algorithm designed as an alternative to the conventional proportional integral derivative (PID) control. It follows the fundamental principle of PID control, which is basically error driven rather than model-based control law [120]. However, it seeks to address the limitations of PID in handling system uncertainties, improving disturbance estimation, and enhancing disturbance rejection [120], [128]. Cross-coupling effects are internal interactions/dynamics which can be treated as disturbances. Thus, LADRC can be implemented in multivariable decoupling controls [132]. While the foundational principles of LADRC have been documented in the literature [128], [132] and [133], it is emphasised here to highlight the significance of its fundamental design gains essential for ensuring reliable control performance. Additionally, a mathematical representation of the gains tailored to the specific application of the TAB is derived. The TAB topology is as shown in Fig. 4.2 for reference.

4.2.1 Fundamental Principles of LADRC

A conventional second-order plant expressed in the following form (4.1) is built up to the LADRC second-order control process in (4.2).

$$\ddot{y} = -a_1\dot{y} - a_2 y + d + bu \tag{4.1}$$

where, y is the system output, a_1 and a_2 are unknown constants, d is a disturbance, b is the critical gain, and u is the plant control input. Equation (4.1) can be further expressed as (4.2):

$$\ddot{y} = f(t, y, \dot{y}, d) + b_0 u \tag{4.2}$$

where, $f(t, y, \dot{y}, d) = -a_1\dot{y} - a_2 y + d + (b - b_0)u$ is an unknown lumped term which represents the total external disturbance and internal dynamics, and b_0 is the nominal value of the critical gain which can be estimated from the nominal values of the energy storage elements of the system. If the lumped term value can be determined, it can be compensated for in real time. This is the basic concept of LADRC. Hence, a LESO can be used to observe both the state of the system and lumped term.

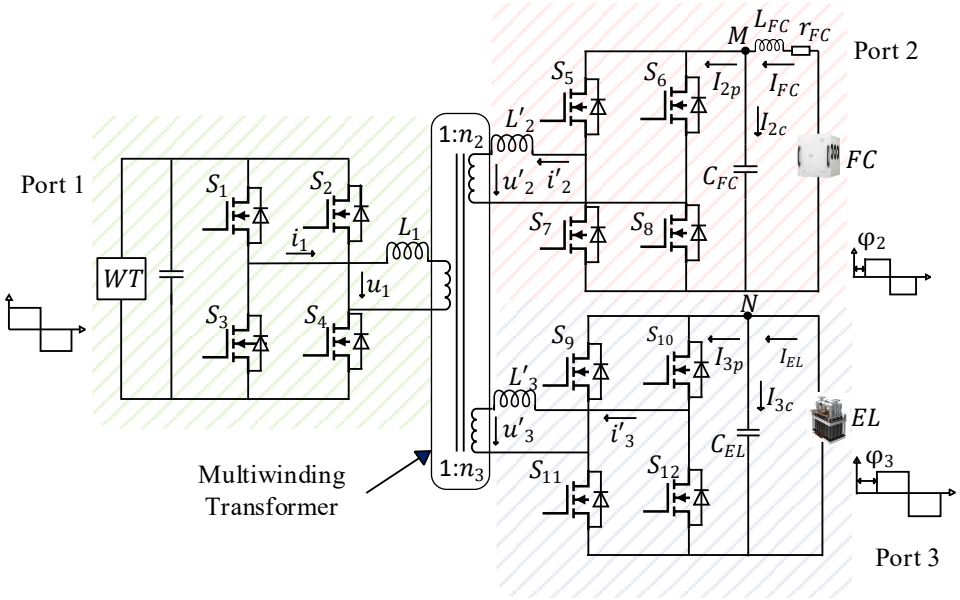

Fig. 4.2: Triple active bridge converter topology.

The states of the second-order plant are defined in (4.3):

$$x_1 = y \qquad x_2 = \dot{y} \qquad x_3 = f(t, y, \dot{y}, d) \tag{4.3}$$

where, x_3 denotes the extended state. Subsequently, (4.3) can be expressed into a matrix form (4.4),

$$\dot{x} = Ax + Bu + E\dot{f} \qquad y = Cx$$
$$A = \begin{bmatrix} 0 & 1 & 0 \\ 0 & 0 & 1 \\ 0 & 0 & 0 \end{bmatrix}, B = \begin{bmatrix} 0 \\ b_0 \\ 0 \end{bmatrix}, C = \begin{bmatrix} 1 \\ 0 \\ 0 \end{bmatrix}^T, E = \begin{bmatrix} 0 \\ 0 \\ 1 \end{bmatrix} \tag{4.4}$$

and $\dot{f}$ represent the dynamics of the lumped term which is assumed to be bounded. Designing an extended observer for the system yields (4.5).

$$\dot{z} = Az + Bu + Le \qquad \hat{y} = Cz \tag{4.5}$$

where, L is a matrix containing β_1, β_2, and β_3 which are the observer gains, $e = (y - \hat{y})$ is the error between the estimated output and system output (observer's estimation error), and z is the observer estimate of the system state. The observer gains are chosen as a function of the observer bandwidth, using bandwidth parameterisation [133], given by (4.6):

$$\beta_1 = 3w_0 \quad \beta_2 = 3w_0^2 \quad \beta_3 = w_0^3 \tag{4.6}$$

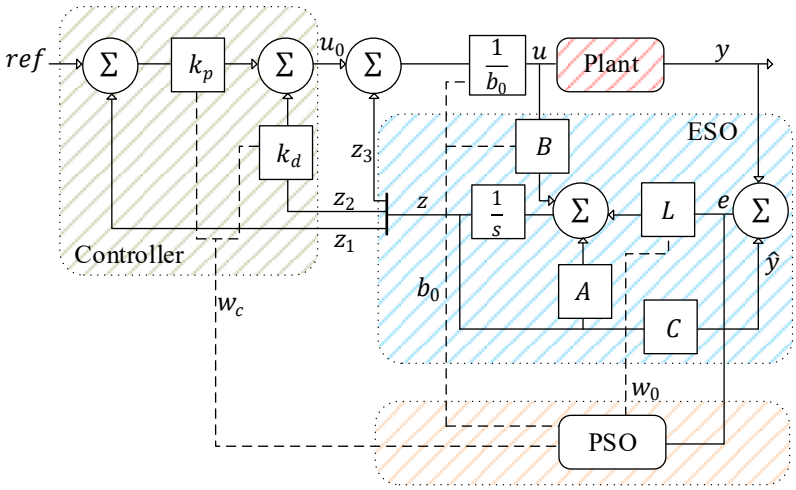

Fig. 4.3 Typical LADRC schematic for second-order plant. (The controller is shown in the green shaded box, the LESO in the blue shaded box, PSO in the orange shaded box while the dashed lines represent the PSO outputs used to determine the critical gain, controller gains and observer gains).

A well-tuned observer can track $y, \dot{y}$ and $\dot{f}$ through z_1, z_2, and z_3. Subsequently, the LADRC can compensate for the cross-coupling effects by eliminating the third state z_3, which can be obtained by (4.7):

$$u = \frac{u_0 - z_3}{b_0} \tag{4.7}$$

Applying (4.7) to (4.2) yields the following relation (4.8):

$$\ddot{y} = u_0 \tag{4.8}$$

This can be easily achieved using a simple proportional derivative controller, given by (4.9).

$$u_0 = k_p(ref - z_1) - k_d z_2 \tag{4.9}$$

where, u_0 denotes the system control input. The controller gains k_p and k_d can be derived from the controller bandwidth [133], as in (4.10).

$$k_p = w_c^2 \quad k_d = 2w_c \tag{4.10}$$

The introduction of bandwidth parameterisation [133] notably reduces the number of LADRC gains that require tuning. This leaves three crucial gains to be tuned for second-order LADRC, as illustrated by the dotted lines in Fig. 4.3. This scenario is analogous to a

first-order plant except for $\dot{y}$ in the lumped term [132], [134]. The critical gain b_0 dictates the controller's sensitivity to disturbances, with higher values indicating greater sensitivity. Observer gains determined by the observer bandwidth w_0 influence the disturbance estimation of the system. Higher values lead to faster disturbance estimation and error tracking. The controller gains, derived from the controller bandwidth w_c, dictate the intensity of control actions in response to estimated disturbances and tracking errors. Extreme values, whether too high or too low, tend to result in noisy, oscillating, or inadequate tracking signals.

4.2.2 Lumped Term and Gains Expression for TAB

The system consists of two control loops: the current control loop at the FC port with an LC filter is analysed as a second-order plant, and the voltage control loop at the EL port is modelled as a first-order plant. Kirchoff's voltage and current laws are applied at node M as shown in Fig. 4.2. Considering the dynamics of the LC filter and combining it with linearised system matrix previously defined in (3.12) in chapter three, modified in (4.11)for the present application, yields the second-order equation in (4.12):

$$\begin{bmatrix} I_{FC} \\ I_{EL} \end{bmatrix} = \begin{bmatrix} \frac{4(V_{EL}L_1 + V_{DE}L_3)}{\pi^3 f_s A} & \frac{-4V_{EL}L_1}{\pi^3 f_s A} \\ \frac{-4V_{DE}L_1}{\pi^3 f_s A} & \frac{4(V_{DE}L_1 + V_{DE}L_2)}{\pi^3 f_s A} \end{bmatrix} \begin{bmatrix} \varphi_2 \\ \varphi_3 \end{bmatrix} = G \begin{bmatrix} \varphi_2 \\ \varphi_3 \end{bmatrix} \tag{4.11}$$

where, $A = (L_1L_2 + L_2L_3 + L_1L_3)$

$$I''_{FC} = \frac{-I_{FC}}{L_{FC}C_{FC}} - \frac{r_{FC}}{L_{FC}} I'_{FC} + \frac{G_{11}\varphi_2}{L_{FC}C_{FC}} + \frac{G_{12}\varphi_3}{L_{FC}C_{FC}} \tag{4.12}$$

Rewriting (4.12) in the form of (4.2), yields (4.13):

$$I''_{FC} = f_{FC}(t, I_{FC}, I'_{FC}, d) + b_{0,FC}\varphi_2 \tag{4.13}$$

where,

$$f_{FC}(t, I_{FC}, I'_{FC}, d) = \frac{-I_{FC}}{L_{FC}C_{FC}} - \frac{r_{FC}}{L_{FC}} I'_{FC} + \frac{G_{12}\varphi_3}{L_{FC}C_{FC}} + \left(\frac{G_{11}}{L_{FC}C_{FC}} - \frac{G_{11,0}}{L_{FC,0}C_{FC,0}}\right)\varphi_2 \tag{4.14}$$

$$b_{0,FC} = \frac{G_{11,0}}{L_{FC,0}C_{FC,0}} \tag{4.15}$$

where, f_{FC} in (4.15) represents the lumped term, $b_{0,FC}$ in (4.15) is the critical gain, r_{FC} is the lumped parasitic resistance of the LC filter, and $G_{11,0}$, $L_{FC,0}$, $C_{FC,0}$ are the nominal values of G_{11}, L_{FC} , and C_{FC} respectively.

To observe f_{FC}, a LESO is designed based on (4.5) −(4.7), as given in (4.16) and (4.17)

$$\dot{z}_{FC} = [A_2 - L_2C_2]z_{FC} + [B_2 \;\; L_2]u_2 \tag{4.16}$$

$$y_2 = z_{FC} \tag{4.17}$$

where, z_{FC} is the output of the observer tracking I_{FC}, I'_{FC}, and f_{FC}. The state-space matrices A_2, B_2, C_2, and L_2 follow the expression given in (4.4) and an input vector u_2 is $[\varphi_2 \;\; I_{FC}]^T$.

Following the same principle, applying Kirchoff's voltage and current laws at node N yields the following first-order equation:

$$V'_{EL} = \frac{V_{EL}}{C_{EL}} + \frac{G_{21}\varphi_2}{C_{EL}} + \frac{G_{22}\varphi_3}{C_{EL}} \tag{4.18}$$

Rewriting (4.18) in the form of (4.2), gives (4.19):

$$V'_{EL} = f_{FC}(t, V_{EL}, d) - b_{0,EL}\varphi_3 \tag{4.19}$$

where,

$$f_{EL}(t, V_{EL}, d) = \frac{V_{EL}}{C_{EL}} + \frac{G_{21}\varphi_2}{C_{EL}} + \left(\frac{G_{22}}{C_{EL}} - \frac{G_{22,0}}{C_{EL,0}}\right)\varphi_3 \tag{4.20}$$

$$b_{0,EL} = \frac{G_{22,0}}{C_{EL,0}} \tag{4.21}$$

where, f_{EL} in (4.20) represents the lumped term, $b_{0,EL}$ in (4.21) is the critical gain, and $G_{22,0}, C_{EL,0}$ are nominal values of G_{22} and C_{EL}.

To observe f_{EL}, a LESO is designed based on (4.5) − (4.7), to derive (4.22) and (4.23)

$$\dot{z}_{EL} = [A_3 - L_3C_3]z_{EL} + [B_3 \;\; L_3]u_3 \tag{4.22}$$

$$y_3 = z_{EL} \tag{4.23}$$

where, z_{EL} is the output of the observer tracking V_{EL} and f_{EL}. The state-space matrices A_3, B_3, C_3, and L_3 follow the expression given in (4.4), modified for a first-order plant, and the input vector u_3 is $[\varphi_3 \ V_{EL}]^T$.

Similarly, in a stable open-loop system, each loop $w_{0,EL}$ and $w_{0,FC}$ can be derived from the open-loop order response approximation. For second and first-order plants (4.24),

$$w_{0,FC} = \frac{5Q_{FC}}{t} \ , \qquad w_{0,EL} = \frac{8Q_{EL}}{t} \tag{4.24}$$

where, t is the settling duration and $Q_{FC} \geq 1$ and $Q_{EL} \geq 1$.
The controller bandwidths are related to the observer bandwidths as (4.25)

$$w_{c,FC} = \frac{w_{o,FC}}{Q_{FC}} \ , w_{c,EL} = \frac{w_{o,EL}}{Q_{EL}} \tag{4.25}$$

4.3 LADRC Gain Optimisation

Three tuning parameters are necessary for the LADRC design, as shown in Fig. 4.3. Conventionally, these gains are manually tuned which could be subjective and increase design complexity, particularly in multiport-isolated converters with multiple control loops. Consequently, there is a need for a more systematic way to determine the optimal gains of LADRC. Utilising the potential estimation error within the observer, mathematically depicted in (4.5), as an input for determining the optimum gains promises to enhance the performance of the controller. The optimisation problem formulation and technique are discussed based on the aforementioned models, respectively.

4.3.1 Optimisation Problem Formulation

For a TAB-based LADRC, the objective is to minimise the observer's estimation error. This error represents the disparity between the estimated output and system output for both first- and second-order plants.

The state matrices, controller, and observer gains, for a second-order and first-order plant, following (4.4), (4.6), (4.10), and (4.25), respectively, are given as (4.26)−(4.29):

$$L_2 = \left[3w_{0,FC} \ , 3{w_{0,FC}}^3 \ , {w_{0,FC}}^2 \ \right]^T \ B_2 = \left[0, b_{0,FC}, 0 \ \right]^T, \qquad w_{c,FC} = \frac{w_{0,FC}}{Q_{FC}} \tag{4.26}$$

$$A_2 = \begin{bmatrix} 0 & 1 & 0 \\ 0 & 0 & 1 \\ 0 & 0 & 0 \end{bmatrix} \quad C_2 = [1 \quad 0 \quad 0] \tag{4.27}$$

$$L_3 = \left[2w_{0,EL},\ \ {w_{0,EL}}^2\right]^T \quad B_3 = \left[b_{0,EL}, 0\right]^T \quad w_{c,EL} = \frac{w_{0,EL}}{Q_{EL}} \tag{4.28}$$

$$A_3 = \begin{bmatrix} 0 & 1 \\ 0 & 0 \end{bmatrix} \quad C_3 = [1 \quad 0] \tag{4.29}$$

where all terms were previously defined. Consequently, the estimated current and voltage are calculated as in (4.30)−(4.33)

$$I_{e,FC} = C_2(A_2 z_{FC} + B_2 \varphi_2) + C_2 L_2\left(I_{ei,FC} - I_{i,FC}\right) \tag{4.30}$$

$$e_{FC} = I_{e,FC} - I_{FC} \tag{4.31}$$

$$V_{e,EL} = C_3(A_3 z_{EL} + B_3 \varphi_3) + C_3 L_3\left(V_{ei,EL} - V_{i,EL}\right) \tag{4.32}$$

$$e_{EL} = V_{e,EL} - V_{EL} \tag{4.33}$$

where, $I_{i,FC}$ and $I_{ei,FC}$ are the initial current output and initial estimated current, respectively; $I_{FC}, and\ I_{e,FC}$ are the current output and estimated current of the second-order plant, respectively. Furthermore, $V_{i,EL}$ and $V_{ei,EL}$ are the initial voltage output and initial estimated voltage, respectively, while V_{EL} and $V_{e,EL}$ are the voltage output and estimated voltage of the first-order plant, respectively. The errors generated in the FC and EL ports are denoted as e_{FC} and e_{EL}, respectively.

The mean square error is implemented as the objective function as follows in (4.34):

$$J_{FC} = \underset{q,FC}{Min}\left(\frac{1}{n}\sum e_{FC}^2\right), J_{EL} = \underset{q,EL}{Min}\left(\frac{1}{n}\sum e_{EL}^2\right) \tag{4.34}$$

where, $q_{,FC} = \left[w_{0,FC}\ , b_{0,FC}\right]^T$ and $q_{,EL} = \left[w_{0,EL}\ , b_{0,EL}\right]^T$ are the optimisation variables, i.e. the critical gain b_0 and the observer bandwidth w_0 for each control loop and n denotes the number of data points or samples. The controller bandwidth w_c is calculated together with the observer bandwidth by the bandwidth parameterisation rule as illustrated in (4.26). Minimising J as depicted in (4.34) directly improves observer accuracy and, consequently, decoupling quality (since the LESO's estimate is utilised in the process of cancelling out in real time the lumped term).

It must be noted however, that controller gains are limited by sampling frequency and sensor noise [132]. Hence, as illustrated in [135] and [136] the observer bandwidth w_0 should be lower than the sampling frequency to avoid amplification of sensor noise. Therefore, the observer bandwidth is limited to a conservative margin of $0 < w_0 < \epsilon f_s$, $\epsilon \approx 0.1 – 0.5$. The critical gain b_0 as discussed in Section Fundamental Principles of LADRC4.2.1 is constrained around the nominal values of the energy storage elements of the system. The optimisation will subsequently terminate when the maximum iteration is reached.

4.3.2 Optimisation Algorithm

The choice of the optimisation technique is not fixed, provided it can handle non-linear problems. Nevertheless, PSO is chosen for its simplicity in implementation and versatility. Its effective memory capability allows potential solutions to recall past best solutions and compare them with neighbouring best solutions, fostering the generation of even better solutions. In essence, PSO efficiently performs global searches. In this study, an alternative algorithm, the genetic algorithm (GA), is employed to benchmark the PSO. The GA implementation is based on standard binary coding and stochastic universal sampling as typified in [137]. Both algorithms are population-based search techniques that rely on information sharing among populations to improve their search processes through a blend of deterministic and probabilistic rules. Both can be applied to a wide range of optimisation problems without the need for problem specific knowledge. However, they differ in search strategies and mechanisms.

As illustrated in Table 4.1, which summarises the key characteristics of the two algorithms, PSO generally converges faster than GA [138, 139]. This is mainly because PSO updates each particle's position using information from its personal best and the best position found by neighbouring particles or the entire swarm. This information sharing mechanism enables efficient global search with relatively few control parameters and provides good memory capability. In contrast, GA relies on genetic operators such as selection, crossover, and mutation, which introduce additional computational steps and may lead to slower convergence. However, these genetic operations help maintain population diversity, allowing GA to explore complex search spaces and locate good solutions even for difficult optimisation problems [140],[141].

Table 4.1: Comparison between PSO and GA

	PSO	GA
Computational Efficiency	Higher	Lower
Ease of Implementation	Easier	Easy
Convergence Speed	Faster	Slower
Iteration	Fewer	More

PSO imitates the swarm behaviour. Each particle in the sample space represents a potential solution to the optimisation problem. The initial velocity, V and position, X of each particle within the defined ranges of the decision variables are calculated using the basic equations given in [140], as illustrated in (4.35).

$$V_j^{n+1} = \omega V_j^n + c_1 r_1\left(Pbest_j^n - X_j^n\right) + c_2 r_2\left(Gbest^{\,n} - X_j^n\right) \tag{4.35}$$
$$X_j^{n+1} = X_j^n + V_j^{n+1}$$

where, n is the iteration index, c_1 and c_2 are constants set to 1.4962 [142]. Additionally, r_1 and r_2 are two randomly generated numbers between 0 and 1 and ω, inertia constant, taken as 0.7298 [142]. This yields Gbest (global best position) and Pbest (personal best position). The fitness of each particle at the initial position is evaluated iteratively using the optimisation objective. An update of each particle's position and velocity is then evaluated based on the initial best-known position and global best-known positions. The process is repeated until a position that fits the control objective is derived or the maximum number of iterations is reached.

The PSO algorithm follows the flow chart depicted in Fig. 4.4, and MATLAB software is used for offline gain calculations. Initially, a vector representing particle positions, X (comprising the critical gain, observer bandwidths, and controller bandwidths) is generated randomly. The following steps are executed in each iteration:

1. At iteration n , each particle X_j^n is evaluated. This evaluation yields estimated current and voltage (evaluated at X_j^n) along with the objective function J_{FC} or J_{EL} (depending on the system's order)

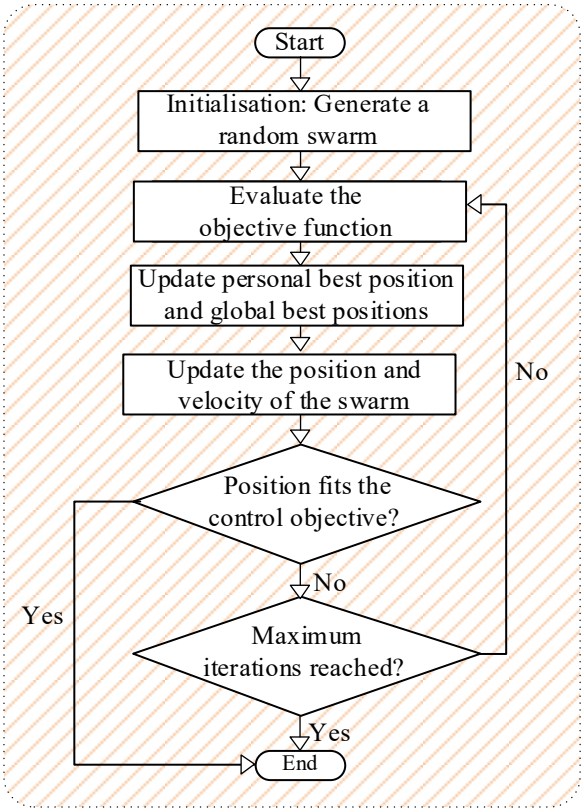

Fig. 4.4: PSO flow chart.

2. The evaluation of the objective function J_{FC} or J_{EL} (evaluated at X_j^n) for each individual X_j^n is compared with its evaluation in the previous iteration. Thus, the particle position X_j^n that achieves the minimum best value is defined as Pbest_j^n.
3. This comparison in step 2 is made with respect to equations (4.30) or (4.31) depending on the order of the system.
4. The Pbest that achieves the minimum e_{FC}^2 or e_{EL}^2 value within the entire swarm is defined as Gbest.
5. Utilising the basic equations of PSO (4.35), the velocity and position of the individuals are updated accordingly.
6. Upon completion of all iterations, gbest is identified, comprising the optimal bandwidths with minimum e_{FC}^2 or e_{EL}^2.

Finally, according to the formulations provided, the optimised gain LADRC decoupling control with PSO schematics is depicted in Fig. 4.5.

The system control inputs are implemented as (4.36) and (4.37):

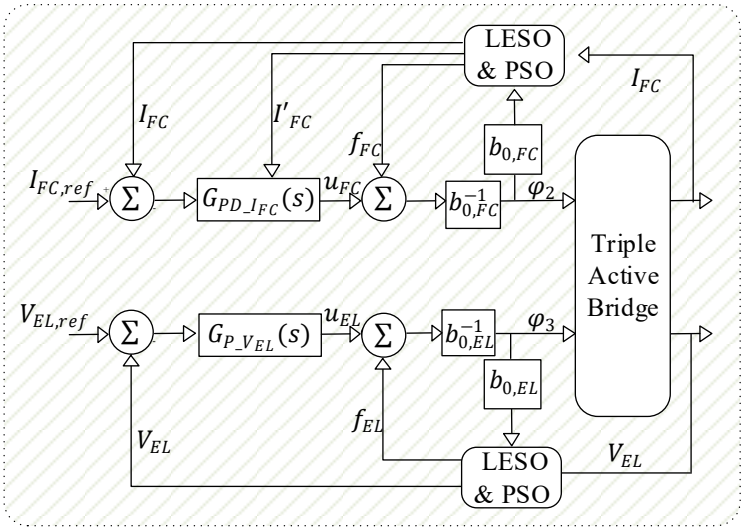

Fig. 4.5: Optimised gain LADRC decoupling control with PSO schematic.

$$u_{FC} = k_p\left(I_{FC,ref} - I_{FC}\right) - k_d I'_{FC} \tag{4.36}$$

$$u_{EL} = k_p\left(V_{EL,ref} - V_{EL}\right) \tag{4.37}$$

While the actual plant control inputs are depicted in (4.38) and (4.39):

$$\varphi_2 = \frac{u_{FC} - f_{FC}}{b_{0,FC}} \tag{4.38}$$

$$\varphi_3 = \frac{u_{EL} - f_{EL}}{b_{0,EL}} \tag{4.39}$$

The actual plant control inputs φ_2 and φ_3 can deliver a decoupled control while ensuring adequate set point tracking.

4.4 Simulation Results

Simulations are performed to substantiate the effectiveness of the optimised gain LADRC. The circuit is modelled using the SIMULINK/MATLAB simulation package, as illustrated in Fig. 4.2. The control schematic is implemented as shown in Fig. 4.5. Table 4.2: lists the electrical specifications of the TAB DC-DC converter.

Two scenarios covering the worst-case conditions are considered in the simulations to validate the performance of the optimised gain LADRC. In the first scenario, the reaction

Table 4.2: TAB Converter and Controller Specifications

Description	Symbol	Unit	Ports		
			#1	#2	#3
Voltage Rating	V_{WT}, V'_{FC}, V'_{EL}	V	560	46	73
Leakage Inductance	L_1, L'_2, L'_3	µH	780	4.992	13.18
Switching frequency	f_s	kHz	15	15	15
Transformer Turns Ratio	n_2, n_3	-	1	0.08	0.13
Optimised gain LADRC with PSO	w_0	rad/s	-	6.20e3	7.81e3
	w_c	rad/s	-	3.10e3	1.56e3
	b_0	-	-	6.94e7	4.71e3
Optimised gain LADRC with GA	w_0	rad/s	-	7.51e3	5.82e3
	w_c	rad/s	-	1.87e3	1.16e3
	b_0	-	-	5.26e7	5.42e3
PI controller	K_i	-	-	6000	8000
	K_p	-	-	15	10

of the corresponding ports is observed when the power supplied by the FC is varied. Hence, step changes are applied to P_{FC} at 0.05 s, 0.1 s and 0.15 s with -200 W to -1000 W, -1000 W to – 600 W and -600 W to -750 W respectively. During this process, the power absorbed by the EL port is maintained at 1000 W and the WT port acts as the slack port. The results of this scenario are shown in Fig. 4.6a. In the second scenario, the FC port maintains a constant power supply of 1000 W, while step changes are made to the power absorbed by the EL port within the same time intervals as in scenario 1, with variations from no power to 1000 W, 1000 W to 350 W, and 350 W to 100 W. The WT port serves as a slack bus, and the results are demonstrated in Fig. 4.6b.

Cross-coupling effects are the internal interactions which manifest as disturbances. This can be quantified as the percentage of the power deviation (undershoot or overshoot) relative to the nominal value in response to intentional or unintentional modifications in the power supplied or absorbed by other ports. The lower this value, the better the decoupling control. The LADRC is designed to eliminate the lumped term, which is a combination of internal dynamics and external disturbances, to compensate for the cross-coupling effect. In this study, the optimum gains of the LADRC are determined using PSO.

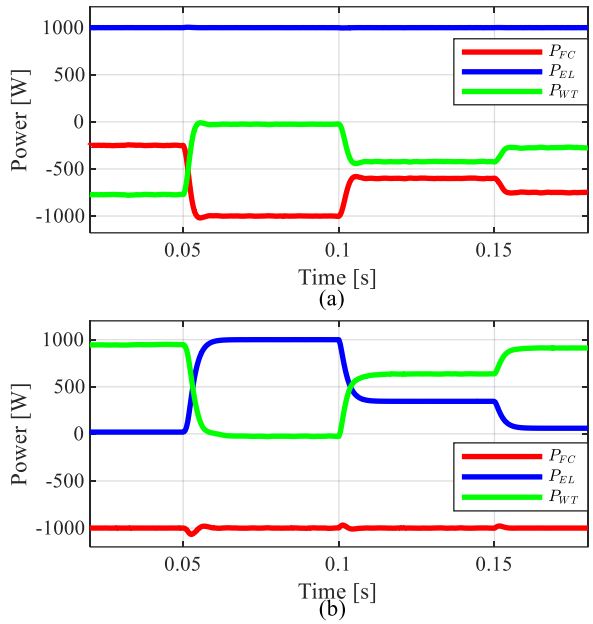

Fig. 4.6: Power transfer between ports using the optimised gain LADRC decoupling control with PSO: (a) Power absorbed by the EL when step changes are applied to the power supplied by the FC and E ports, and (b) Power supplied by the FC port when step changes are applied to the power absorbed by the EL and WT ports.

First, the performance of the optimised gain LADRC with PSO is evaluated, as shown in Fig. 4.6. In the first scenario, the optimised gain LADRC with PSO exhibits a negligible power undershoot or overshoot from the nominal value at the EL port, as shown in Fig. 4.6a. While there are deviations in scenario 2, as depicted in Fig. 4.6b, these deviations are maintained at a minimum power undershoot and overshoot at the three applied step changes. Furthermore, a good power flow response is observed at the corresponding ports in each scenario.

In addition, simulations are carried out with optimised gain LADRC with GA, LADRC with no optimisation and PI without decoupling control, as shown in Fig. 4.7 and Fig. 4.8 to ascertain the superiority of the optimised gain LADRC with PSO. For adequate comparison, the simulation utilises the average gains obtained from an equal number of runs of each optimisation technique, as seen in Table 4.2. In scenario 1, the optimised gain LADRC with GA demonstrates a similar outcome of negligible power deviation with the optimised gain LADRC with PSO, as illustrated in Fig. 4.7a and Fig. 4.7b, respectively. On the other hand, the LADRC with no optimisation shows a 3 % overshoot, 2 % undershoot

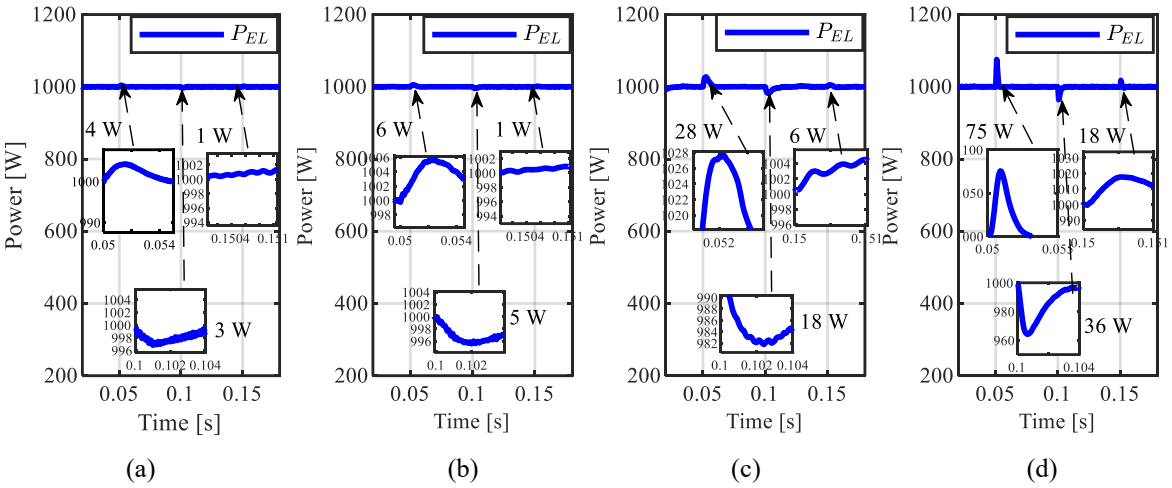

Fig. 4.7: The power absorbed by the EL when step changes are applied to the power supplied by the FC and WT ports for (a) Optimised gain LADRC decoupling control with PSO, (b) Optimised gain LADRC decoupling control with GA,(c) LADRC with no optimisation and (d) PI without decoupling control.

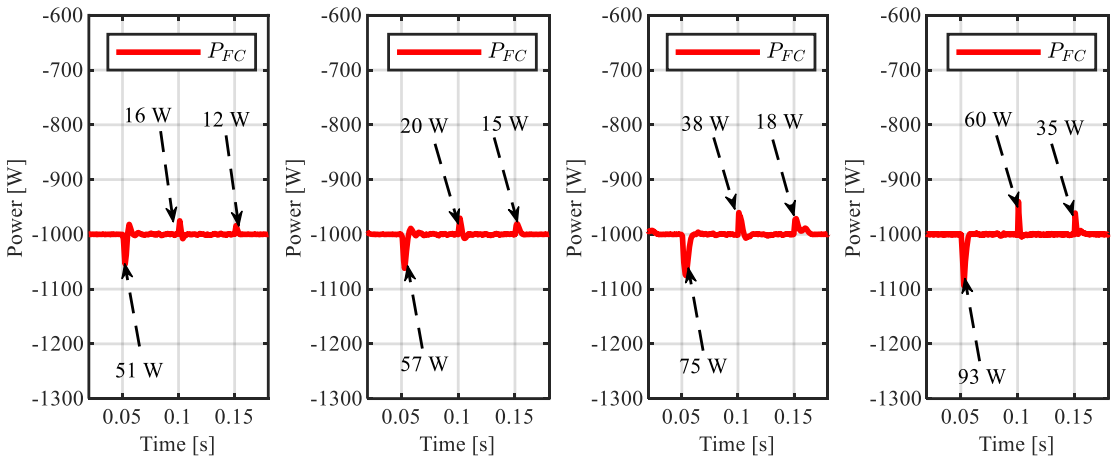

Fig. 4.8: Power supplied by the FC port when step changes are applied to the power absorbed in the EL and WT ports for (a) Optimised gain LADRC decoupling control with PSO, (b) Optimised gain LADRC decoupling control with GA,(c) LADRC with no optimisation and (d) PI without decoupling control.

and a negligible overshoot at the last step change while, the PI without decoupling control exhibits an 8 % overshoot, a 4 % undershoot, and a 2 % overshoot, as illustrated in Fig. 4.7c and Fig. 4.7d respectively. This shows that the choice of the optimisation algorithm is not fixed if the optimisation objective is met.

Similarly, in scenario 2, The PI without decoupling exhibits 9 % undershoot, 6 % overshoot, and 4 % overshoot, with the LADRC with no optimisation exhibiting a 7 % undershoot, 4 % overshoot and 2 % overshoot , as illustrated in Fig. 4.8c and Fig. 4.8d respectively. On the other hand, the optimised gain LADRC with GA displays 6 % undershoot, 2 % overshoot, and negligible overshoot at the third step change, as depicted in Fig. 4.8b. In contrast, the optimised gain LADRC with PSO shows a 5 % undershoot, 2 % overshoot, and negligible power deviation at the third step change in this scenario, as observed in Fig. 4.8a. In this scenario, very similar results in the optimised gain LADRC with GA and the optimised gain LADRC with PSO can also be observed. However, a slightly improved result can be seen in the optimised gain LADRC with PSO, because of the specific characteristics of PSO. The summary of the results is shown in Table 4.3, a significant decoupling performance improvement can be seen with optimised gain LADRC with PSO and GA as compared to the PI without decoupling control.

Table 4.3: Summary of results

Technique	Step time (s)	Scenario 1			Scenario 2		
		Power deviation (W)	% deviation	% improvement	Power deviation (W)	% deviation	% improvement
PI without decoupling control	0.05	75	8	-	93	9	-
	0.1	36	4	-	60	6	-
	0.15	18	2	-	35	4	-
LADRC with no optimisation	0.05	28	3	62	75	7	19
	0.1	18	2	50	38	3	37
	0.15	6	~ 0	67	18	2	49
Optimised gain LADRC with GA	0.05	6	~ 0	92	57	6	38
	0.1	5	~ 0	86	20	2	66
	0.15	1	~ 0	94	15	2	57
Optimised gain LADRC with PSO	0.05	4	~ 0	95	51	5	45
	0.1	3	~ 0	91	16	2	73
	0.15	1	~ 0	94	12	~ 0	65

4.5 Experimental Validation

To validate the proposed LADRC gain auto-tuning mechanism, where LADRC gains are optimised using PSO with the objective of minimising estimation errors, a proof-of-concept experimental setup is developed as displayed in Fig. 4.9. The system, rated at 100

W, is operated at a switching frequency of 20 kHz. Key parameters include leakage inductances of $L_1 = 11$ µH, $L_2 = 12$ µH and $L_3 = 17$ µH . The transformer core material (N87) with turns ratios (16:10:15) are selected.

The experiment is conducted to replicate the worst-case scenario (scenario 2) from the simulation results. The converter is designed as a system comprising two voltage sources and a load: the WT and FC are represented as voltage sources supplying power, while the EL is represented as a load that sinks power. The voltage sources are configured as follows:

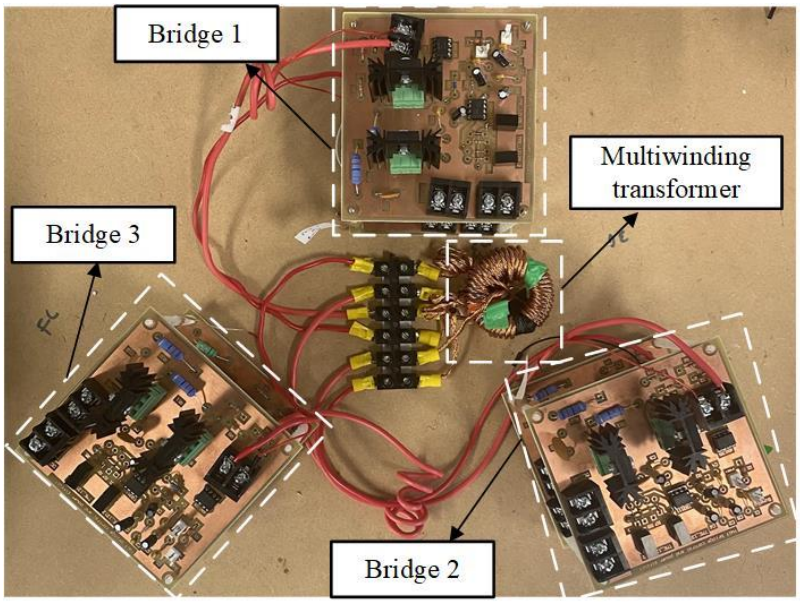

Fig. 4.9: Laboratory proof-of-concept setup for LADRC

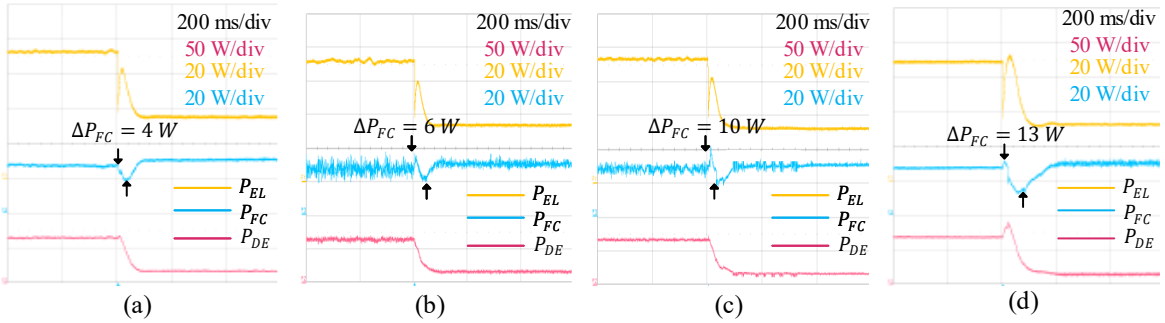

Fig. 4.10: Power supplied by the FC port when step changes are applied to the power absorbed in the EL and WT ports for (a) Optimised gain LADRC decoupling control with PSO, (b) Optimised gain LADRC decoupling control with GA, (c) LADRC with no optimisation and (d) PI without decoupling control.

the WT port is set to 40 V, the FC port to 20 V, and the load connected to the EL port initially has a resistance of 10 Ω, which is later increased to 20 Ω. When a step change is applied to the load at the EL port, the current at the WT port reduces to accommodate the change. The voltage across the load at the EL port remains constant but exhibits disturbances during the load change. The current at the FC port remains nominally unchanged but also experiences disturbances due to cross-coupling effects.

Two controllers, the LADRC and a basic PI controller without any decoupling methodology, are implemented using the same circuit parameters. The gains of the LADRC are optimised offline using the PSO algorithm, which helps reduce design efforts and time, while also concurrently achieving improvements by minimising estimation errors, this is bench marked with the GA algorithm and the LADRC without any optimisation. During the load step change, as seen in Fig. 4.10a-d, The optimised gain LADRC decoupling control with PSO shows a power deviation 16 % from nominal value on the FC port while optimised gain LADRC decoupling control with GA and LADRC with no optimisation gives 25 % and 40 % deviation respectively and the PI without decoupling control shows a deviation of 52 % from nominal value. Hence, the optimised gain LADRC decoupling control with PSO outperforms the other bench marked controllers, demonstrating smaller deviations and faster response from the nominal operating point.

4.6 Comparison Between the Two Proposed Decoupling Control Techniques (Model Reference-Based Hybrid and Optimised LADRC With PSO)

Following from Table 3.2, which compared conventional hardware and software decoupling methods against the proposed model reference–based hybrid decoupling control. Table 4.4 extends the analysis by comparing the model reference–based hybrid decoupling control with the optimised LADRC with PSO under the same evaluation criteria. Both methods are purely software, require no additional hardware, work with asymmetric configurations, scale well, and avoid data storage in LUTs. The model reference–based hybrid decoupling control was able to suppress the cross-coupling effects with a 3 % deviation from nominal value and 1.8 % average percentage deviation at the worst-case. However, it has more gains to tune i.e. the proportional and the integral gains in the PI controller and the proportional and derivative gains in the PD controller. In addition, to

Table 4.4: Overview of multiport-isolated DC-DC converter decoupling techniques (model reference-based and the optimised LADRC with PSO)

Details of operation	Model Reference-based Decoupling Control	Optimised LADRC with PSO
Additional component	None	None
Estimation error	None	Yes (Minimised via PSO)
Ease of implementation	Medium	Medium-High
Extra data storage	Low	Low
Power operational region	Wide	Wide
Hardware Complexity	Low	Low
Converter Configuration	Asymmetric	Asymmetric
Tuning burden	Medium	Low
Scalability	Easy	Easy
Model dependence	Moderate (needs plant matrix)	Low (only order of the system)
Worst case % deviation	3 %	5 %
Average % deviation (worst case scenario)	1.8 %	2.6 %
Average % improvement compared to PI with no decoupling (worst case scenario)	71 %	58 %

supress noise/EMI, a low pass filter is usually implemented with the derivative term. The optimised LADRC achieves a 5 % and 2.6 % average deviation from nominal values at the worst-case, with a much lower tuning burden because PSO automatically selects the observer and controller gains by minimising the LESO estimation error. LADRC does not also need full system model understanding, it relies primarily on plant order.

4.7 Summary

A multiport-isolated DC-DC converter possesses an inherent cross-coupling effect between its ports owing to the multiwinding transformer which makes precise control difficult. In this chapter, LADRC was implemented as decoupling controller where its optimum gains were determined using PSO instead of manual tuning techniques. The optimised gain LADRC with PSO is composed of a controller with high bandwidth LESO and PSO-based gain optimisation. The optimised gain LADRC provides an auto-tuning gain solution by generating an optimised gain through PSO, thus reducing the manual tuning complexities. The objective function for the optimisation was defined to minimise the estimation error of the LESO. Firstly, the converter's control output relationship is

established, and the cross-coupling effect is analysed. Furthermore, the mathematical expressions for the LADRC were derived, with PSO performing the optimisation in each control loop. The optimised gain LADRC with PSO satisfactorily suppresses the cross-coupling effect with the lowest power undershoot of 5 % compared to the power undershoots of 6 % and 9 % observed with the optimised gain LADRC with GA and PI without decoupling control techniques across the two simulation scenarios considered. Experimental validation of the optimised gain LADRC with PSO is conducted with a maximum power deviation of 16 % from nominal value against the 44 % with PI without decoupling techniques The LADRC gains were optimised, resulting in reduced design effort and ensuring satisfactory decoupling control performance, as depicted in the results obtained.

Finally, a comparison of the two proposed decoupling control techniques was carried out using criteria such as tuning burden, model dependency, and percentage deviation under worst-case operating conditions.

Chapter 5

Online Power Loss Minimisation

Previous discussions in Chapters 3 and 4 focused on mitigating cross-coupling effects in multiport-isolated DC-DC converters. As highlighted in Section 2.3, these effects are commonly addressed using SPS modulation techniques. Building on these foundations, this chapter proposes an online adaptive steepest descent-based control technique. The proposed controller leverages a predetermined reference for active inter-port power flow and dynamically adjusts the internal phase shifts in real time to minimise the error between the reference and actual values. The proposed controller is validated using MATLAB/Simulink and an experimental laboratory setup. Its performance is compared with two benchmark controllers to evaluate its effectiveness in terms of loss minimisation and computational efficiency. Both simulation and experimental results demonstrate that the adaptive controller achieves lower computational burden, reduced rms current, and improved efficiency compared with bench marked techniques.

5.1 Background

The SPS technique, which provides only two degrees of freedom, has been shown to have an increased inductor rms current and circulating power, thereby reducing overall system efficiency [68, 92]. To address this, techniques with additional degrees of freedom, resulting in advanced configurations such as dual-phase shift (DPS) and triple-phase shift (TPS) strategies. DPS incorporates either two external phase shifts, equal internal phase shifts, or two external shifts with a single internal phase shift. TPS, on the other hand, utilises two external shifts alongside distinct internal phase shifts [96]However, determining the optimal phase shift values remains critical for maximising efficiency.

In the study in [92], a simplified high-frequency chain current was employed to reduce circulating currents using an additional degree of freedom. Although this approach improved the performance, it resulted in a diminished soft-switching region as the power levels increased. In the study outlined in [93], DPS modulation with a genetic algorithm was used to determine the optimal internal phase shift, with results stored in an online LUT. Similarly, [94] applied generic harmonic approximation (GHA) with an optimisation algorithm to determine the internal phase shift. Although both approaches reduced inductor

RMS currents, LUT implementations increase storage requirements and do not fully exploit the available degrees of freedom, limiting efficiency.

In terms of TPS modulation, [95] employed an offline PSO algorithm while [96] combined PSO with an exponential weighted moving average (EWMA) algorithm, targeting reflux power minimisation. Although this strategy achieved reductions in circulating power, it introduced potential fluctuations in the phase shift ratios during optimisation, which could impact converter stability and performance. Similarly, data-driven techniques have shown promise in this regard. For example, [97, 98] developed artificial neural network (ANN)-based and search algorithm techniques to minimise the rms current. These techniques have achieved notable improvements in efficiency; however, the time-consuming process of generating high-quality datasets poses a significant drawback. In addition, [99] explored offline gradient descent, ripple correlation control, and ANN-based approaches for calculating optimal degrees of freedom. Each technique presents unique challenges: offline gradient descent requires extensive pre-computation and LUTs, ripple correlation control exhibits sensitivity to initial conditions and perturbations, and ANN performance depends heavily on the quality of the training data. In another study, [100] implemented a GHA combined with polynomial regression models to predict internal phase shifts. While effective, the complexity of higher-order polynomials poses challenges in control design and risks suboptimal performance if not carefully examined. To address these issues, in [85], an adaptive perturb-and-observe technique is proposed for tracking minimum rms currents. However, this technique neglects the system model, potentially compromising controller robustness. In addition, [90] introduced an advanced MPC algorithm that integrates DC bus voltage variations into the control framework. This approach successfully suppressed the circulating current and improved the response under various DC bus voltage conditions. However, incorporating an integrator for expanded system control, which is necessary to maintain accurate current tracking, introduced limitations in response speed, particularly during rapid voltage variations. Finally, [101] applied gradient descent optimisation to reduce the rms current's impact on conduction losses, but the challenge of accurately measuring and controlling rms current, especially at high frequencies, persisted.

These methods typically involve complex and computationally intensive calculations[96]. Moreover, most existing approaches focus on rms current optimisation, yet measuring rms current accurately, especially at high switching frequencies, remains

challenging. In addition, these techniques generally rely on static tuning mechanisms and do not adapt effectively to changing operating conditions [101].

Given that deviations in inter-port power flow can lead to suboptimal operating conditions and increased system losses, minimising the error between actual and reference active inter-port power flows offers a focused and effective optimisation method for improving overall system efficiency. Hence, to enhance the overall operational efficiency of the multiport-isolated DC-DC converter by reducing the conduction and switching losses, this chapter proposes an online adaptive control based on the steepest descent method. The adaptive control technique (L-TPS) leverages a predetermined reference active inter-port power flow and dynamically adjusts the internal phase shifts in real time to minimise the net error between the reference and actual values. To ensure the stability of the adaptive controller gains, a Lyapunov direct method is implemented. Furthermore, the adaptive controller gains are automatically tuned online based on the tracking error, to further balance convergence speed and stability, thereby enhancing overall controller performance. This real-time adaptation ensures optimal internal phase shift selection under varying operating conditions without requiring extensive data storage or precomputed LUTs, which are often impractical when considering all three internal phase shifts. By integrating online adaptation, the proposed L-TPS controller dynamically regulates the inter-port power flow, contributing to improved efficiency with minimal computational complexity.

Beyond its application in previous chapters, the multiport-isolated DC-DC converter can be utilised in the marine transportation sector, where hydrogen is gaining traction as a

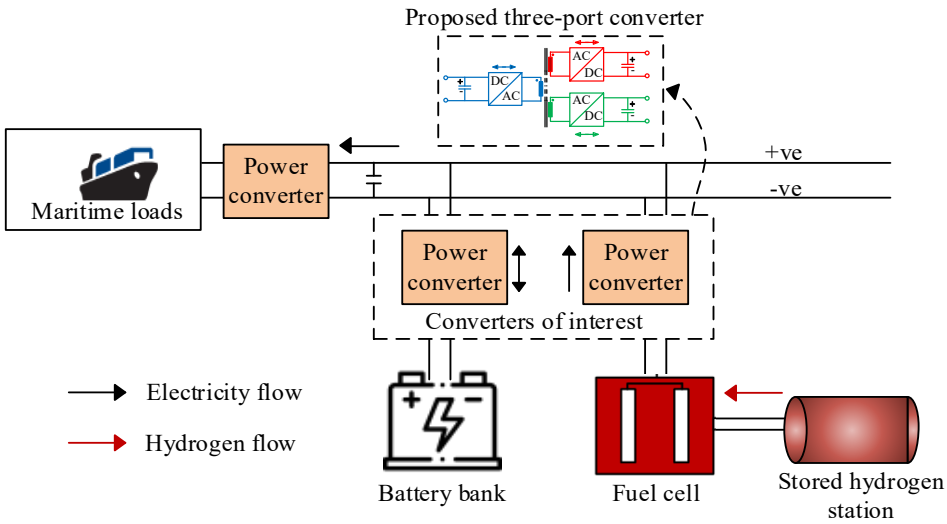

Fig.5.1. Hydrogen Energy Systems Configuration in Marine Sector.

clean and efficient fuel source. Hydrogen-powered FCs can generate electricity for marine propulsion systems and other onboard electrical loads (termed marine loads - ML), with BTs providing short-term energy storage and the heat generated in the process directed for onboard heating [7], [12]. In this chapter, the multiport-isolated DC-DC converter, replaces the "converter of interest" as shown Fig.5.1 in the power management system of the marine transportation sector.

5.2 Operating Principles of Multiport-Isolated DC-DC Converters

The diagram in Fig.5.2 illustrates a single-phase multiport-isolated DC-DC converter, specifically a triple active bridge converter. The BT source in port 1 is the battery model port. Subsequently, the secondary port is labelled as the FC port with a FC model, whereas the tertiary port is identified as the ML port and substituted with a resistive load.

Each port is connected via a full-bridge circuit with a high-frequency leakage integrated multiwinding transformer. The transformer has turn ratios of $1: n_2 : n_3$. Each port includes four switches labelled S_1-S_4 for the primary bridge, S_5-S_8 and S_9-S_{12} for the secondary and tertiary bridges, respectively. Inductors L_1, L_2' and L_3' are the leakage inductances at each port. In addition, i_1, i_2' , and i_3' represent currents through the leakage inductances. The voltages at the midpoint of each full bridge are denoted as u_1, u_2' , and u_3', while V_{BT}, V_{FC}' , and V_{ML}' represent the output voltages of each port. The phase shift angles

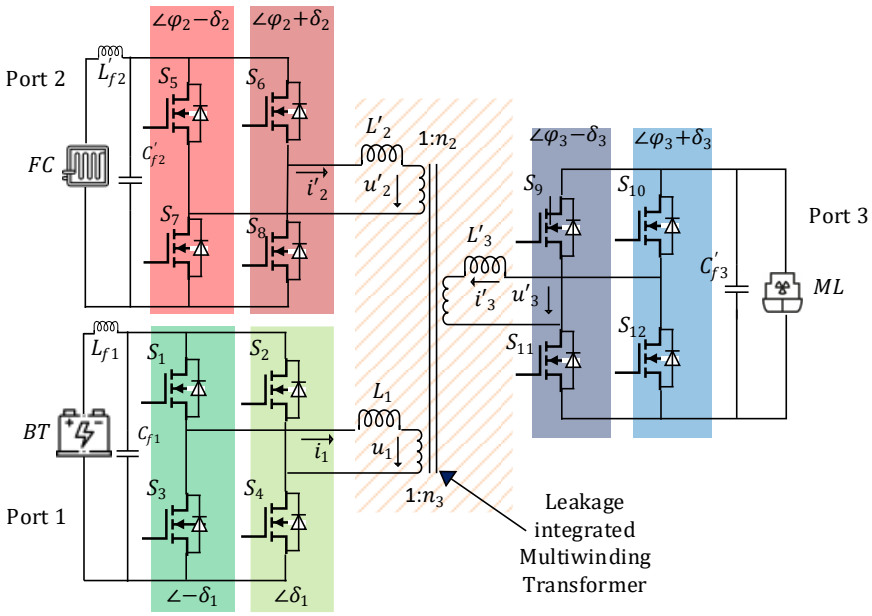

Fig.5.2. Triple active bridge converter.

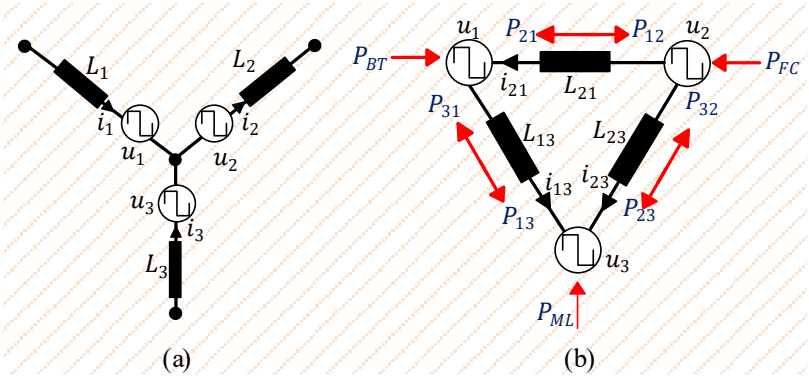

Fig. 5.3. Primary referred TAB equivalent circuit (a) Star connection (b) Delta connection.

φ_2 and φ_3 with control ranges of $\frac{-\pi}{2}$ to $\frac{\pi}{2}$ are adjusted to facilitate power flow between the ports in the circuit, as shown in Fig. 5.3. Thus, the phase shift at the primary port remains zero.

To facilitate the power flow among the three ports, the complete TAB converter can be converted from a star configuration to a delta configuration, as shown in Fig. 5.3, where all elements are referred to the primary side. Subsequently, the leakage inductance in delta transformation is written as expressed in (5.1).

$$L_{12} = \frac{A}{L_3}, L_{13} = \frac{A}{L_2}, L_{23} = \frac{A}{L_1}$$
$$A = L_1L_2 + L_2L_3 + L_1L_3 \tag{5.1}$$

where, L_{12}, L_{13}, L_{23} can be written as L_{xy}

Hence, the inter-port power flow can be represented by a cycle by cycle averaging,

$$P_{xy} = \frac{\varphi(\pi - \varphi)V_xV_y}{2\pi^2 f_s L_{xy}} \tag{5.2}$$

where, x and y represent port numbers 1, 2, or 3, V_x and V_y are the voltages of the two ports, f_s represents the switching frequency, φ is the external phase difference between the bridges, and L_{xy} is the port inductance.

However, (5.2) utilises external phase shifts as control inputs, a method commonly referred to as SPS control. This technique is limited in its ability to independently regulate inter-port power flow, often resulting in cross-coupling effects. While decoupling controllers have been developed to mitigate these effects [116, 143], loss minimisation or the broader

objective of enhancing overall operational efficiency are not considered. Consequently, introducing internal phase shifts within each bridge as an additional degree of freedom is advantageous. As described in [68], to facilitate the full degree of freedom, internal phase shifts that controls the variation in the midpoint voltages is introduced. As shown in Fig.5.2, the range of the internal phase shifts δ_1, δ_2, and δ_3 is 0 to $\frac{\pi}{2}$.

From Fig. 5.3 the fundamental component of the inductor current in any power transfer direction at each port is represented by:

$$|i_{21}| = \sqrt{\frac{|u_1|^2 + |u_2|^2 - 2|u_1||u_2|cos\varphi_2}{(\omega L_{12})^2}}$$
$$|i_{23}| = \sqrt{\frac{|u_2|^2 + |u_3|^2 - 2|u_2||u_3|cos(\varphi_3 - \varphi_2)}{(\omega L_{23})^2}} \quad (5.3)$$
$$|i_{13}| = \sqrt{\frac{|u_1|^2 + |u_3|^2 - 2|u_1||u_3|cos\varphi_3}{(\omega L_{13})^2}}$$

where, $\omega = 2\pi f_s$, $|u_1|$, $|u_2|$ and $|u_3|$ are the peak magnitudes of the fundamental frequency components of the midpoint voltages at each port. Hence, the inductor current in the time domain is given by (5.4), [144]

$$i_2 = i_{23} + i_{21} \ , \ i_3 = -i_{23} - i_{13}, \quad i_3 + i_2 + i_1 = 0 \quad (5.4)$$

Furthermore, the active inter-port power flow (Fig. 5.3), can be explicitly calculated by (5.5).

$$P_{12} = \frac{\sigma_1}{L_{12}} \cos\delta_1 \cos\delta_2 \sin\varphi_2$$
$$P_{23} = \frac{\sigma_2}{L_{23}} \cos\ \delta_2 \cos\ \delta_3 sin(\varphi_3 - \varphi_2) \quad (5.5)$$
$$P_{13} = \frac{\sigma_3}{L_{13}} \cos\delta_1 \cos\delta_3 \sin\varphi_3$$

where, $\sigma_1 = \frac{4V_{FC}V_{BT}}{\pi^3 f}$, $\sigma_2 = \frac{4V_{FC}V_{ML}}{\pi^3 f}$, $\sigma_3 = \frac{4V_{ML}V_{BT}}{\pi^3 f}$

While the active output power flow is given as:

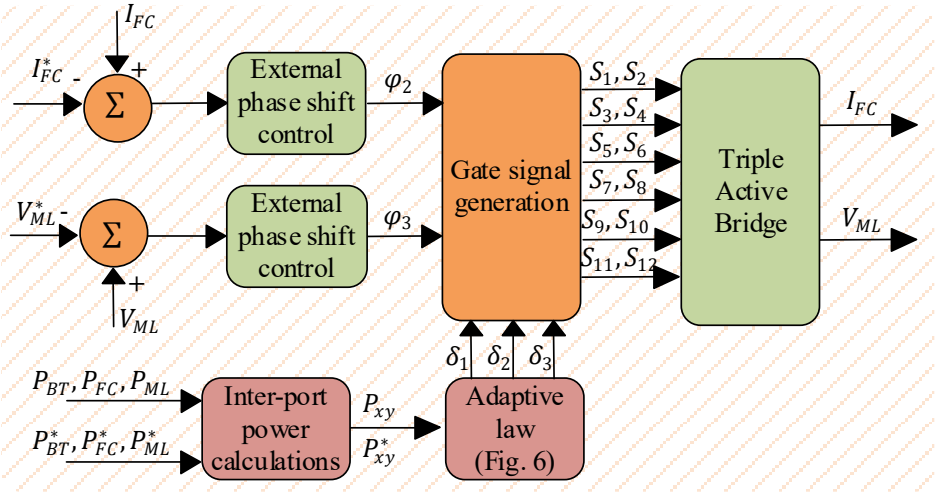

Fig. 5.4.Proposed L-TPS control structure.

$$P_{FC} = P_{23} + P_{21} \ , P_{EL} = -P_{23} - P_{13} \ , \qquad (5.6)$$
$$P_{ML} + P_{FC} + P_{BT} = 0$$

The derived equations (5.3)−(5.6), serve as the core for the analysis of the TAB converter in terms of power loss estimation.

5.3 Proposed L-TPS Control Technique

The diagram in Fig. 5.4 illustrates the control structure employed in the design of the TAB, which is explained in two parts, as detailed in this section. The first part briefly illustrates the external phase shift control, while the second part demonstrates the incorporation of internal phase shifts. The external phase shifts regulate the voltage of ML and the current of the FC, whereas the internal phase shifts are implemented to ensure an optimal flow.

5.3.1 External Phase Shift Control

From the proposed decoupling controls developed in Chapter 3 and Chapter 4, either of the two techniques can be implemented as the external phase-shift control, since cross-coupling issues have been minimised in both techniques.

The model-reference-based hybrid decoupling control described in Section 3.2 utilises the model-reference framework while integrating the best-performing matrix-based technique (the inverse-matrix decoupling control) into the developed decoupling control

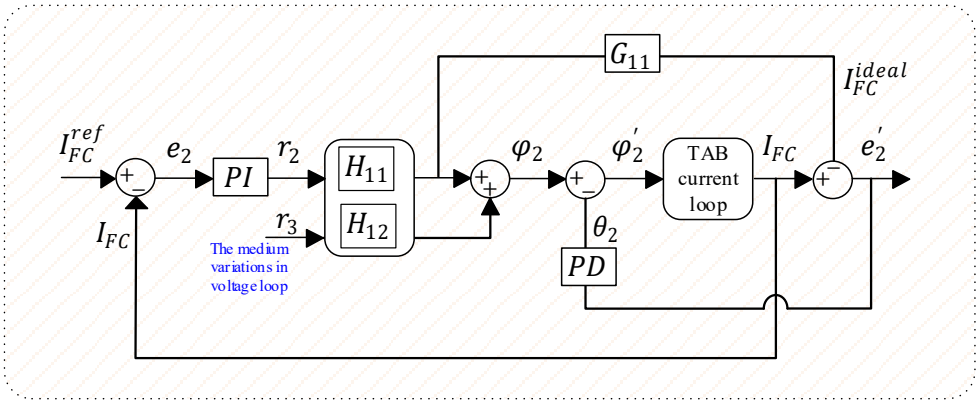

Fig. 5.5. Typical Model reference-based hybrid decoupling control current loop.

structure. The Fig. 5.5 succinctly illustrates the current-control loop of the decoupling controller. Equations (3.26) and (3.27) illustrates the actual control input that achieves set point tracking and minimal cross-coupling effect.

The linear active disturbance rejection control (LADRC) is however utilised in this chapter as the main controller controlling the external phase shifts φ_2 and φ_3. The LADRC is chosen due to its ease of implementation, controller parameter tuned with PSO and requiring minimal knowledge of converter parameters as pointed out in Table 4.4 [120, 132, 145].

From [143], there are two control loops: the voltage and current loops. The current loop is as shown in Fig. 5.6 the observer (with state matrices A, B, C and L) observes the state of the system and provides an estimation for the control objective. However, the voltage loop is without the derivative term k_d.

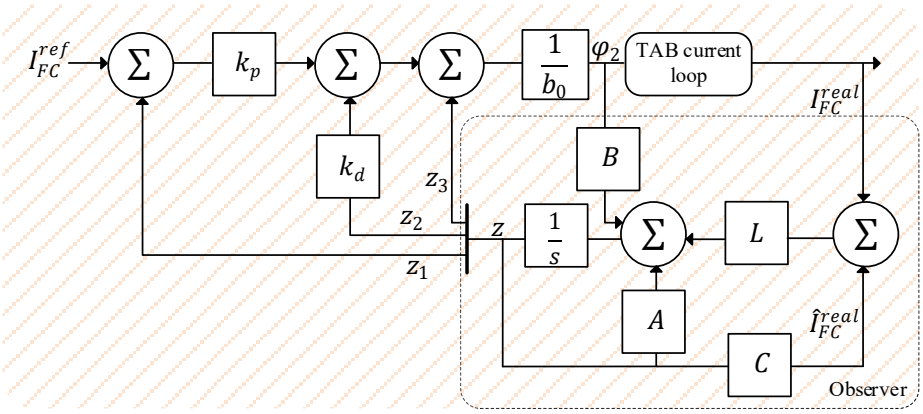

Fig. 5.6. Typical LADRC current loop.

Proportional derivative control is utilised in the current loop, whereas proportional control is sufficient in the voltage loop. Equations (5.7) and (5.8) show the control input in each loop.

$$\varphi_2 = \frac{\left(k_p\left(I_{FC}^{ref} - z_1\right) - k_d z_2\right) - z_3}{b_0} \tag{5.7}$$

$$\varphi_3 = \frac{\left(k_p\left(V_{EL}^{ref} - z_1\right)\right) - z_3}{b_0} \tag{5.8}$$

where, k_p and k_d are the proportional and derivative gains, I_{FC}^{ref} and V_{EL}^{ref} are the reference current and voltage, z_1 and z_2 are the states of the controller, z_3 represents the extended state and, b_0 is the critical gain of the observer, thus, ensuring minimal cross-coupling effect.

5.3.2 Internal Phase Shift Control

To enhance the TAB efficiency, additional degrees of freedom are required. This study employed three internal phase shifts within each bridge as an additional degree of freedom. A precise combination of values for these additional control inputs regardless of operating points is crucial for ensuring an efficient system. To cater for changing operating values and to ensure a stable internal phase shift, an adaptive control law is created which is aimed at minimising the deviation between actual active inter-port power flow and its reference.

5.3.2.1 Problem Formulation

As discussed, minimising system losses requires maintaining optimal power flow within the system. From (5.9), and as expressed in [68], P_{12}, P_{23} and P_{13} are functions of P_{FC} and P_{ML} as shown in (5.9), which are derived expressions from (5.6). These relationships are also used to compute the reference active inter-port power flow.

$$P_{12} = -\frac{2}{3}P_{FC} - \frac{1}{3}P_{ML},\ P_{23} = \frac{1}{3}P_{FC} - \frac{1}{3}P_{ML},$$

$$P_{31} = \frac{1}{3}P_{FC} + \frac{2}{3}P_{ML} \tag{5.9}$$

$$P_{12} + P_{23} + P_{31} = 0$$

Furthermore, the internal phase shifts from (5.10) must be constrained in relation to the system parameters. This is expressed as given in (5.10):

$$\begin{gathered}\delta_1 = cos^{-1}\left(\frac{L_{12}P_{12}}{\sigma_1\, sin\, \varphi_2 cos\, \delta_2}\right) \\ \delta_2 = cos^{-1}\left(\frac{L_{23}P_{23}}{\sigma_2\, sin\, (\varphi_3 - \varphi_2) cos\, \delta_3}\right) \\ \delta_3 = cos^{-1}\left(\frac{L_{13}P_{13}}{\sigma_3\, sin\, \varphi_3 cos\, \delta_1}\right) \\ 0 \leq\ \delta_1, \delta_2, \delta_3 \leq \frac{\pi}{2}\end{gathered} \tag{5.10}$$

Equation (5.9)- (5.10), serves as the basis for the L-TPS control design.

5.3.2.2 Proposed Adaptive Steepest Descent-based Control

The adaptive steepest descent control is employed to determine the internal phase shifts within the system. These internal phase shifts serve as additional degrees of freedom and are leveraged to regulate the active inter-port power flow, aligning with the overall system objective. To facilitate this, the power equation, as presented in (5.10), is discretised using the forward Euler method, with T_s denoting the sampling period. The corresponding discrete-time representations of the state and input vectors are defined as follows in (5.11):

$$x(k+1) = f\left(x(k), u(k)\right) \tag{5.11}$$

Which can be explicitly written as:

$$\begin{gathered}f\left(x(k), u(k)\right) \\ = \begin{bmatrix} P_{12}(k) + \dfrac{T_s\sigma_1\, cos\big(\delta_1(k)\big)\, cos\big(\delta_2(k)\big)\, sin(\varphi_2)}{L_{12}} \\ P_{23}(k) + \dfrac{T_s\sigma_2\, cos\big(\delta_2(k)\big)\, cos\big(\delta_3(k)\big)\, sin(\varphi_2 - \varphi_3)}{L_{23}} \\ P_{13}(k) + \dfrac{T_s\sigma_3\, cos\big(\delta_1(k)\big)\, cos\big(\delta_3(k)\big)\, sin(\varphi_3)}{L_{13}} \end{bmatrix}\end{gathered} \tag{5.12}$$

where, $x(k) = \begin{bmatrix} P_{12} \\ P_{23} \\ P_{13} \end{bmatrix}$ is the actual power measurement and $u(k) = \begin{bmatrix} \delta_1 \\ \delta_2 \\ \delta_3 \end{bmatrix}$ is the internal phase shifts. The reference power flow denoted $x^*(k) = \begin{bmatrix} P_{12}^* \\ P_{23}^* \\ P_{13}^* \end{bmatrix}$ can be computed from (5.12) to satisfy the power dynamics. Hence, the goal is to control the internal phase shifts to minimise the power errors (e_1, e_2, e_3). Therefore, the error equation is given by (5.13) - (5.15):

$$e_1(k) = P_{12}(k) - P_{12}^*(k) \tag{5.13}$$

$$e_2(k) = P_{23}(k) - P_{23}^*(k) \tag{5.14}$$

$$e_3(k) = P_{13}(k) - P_{13}^*(k) \tag{5.15}$$

For simplicity,

$$e_i(k) = P_{ij}(k) - P_{ij}^*(k) \tag{5.16}$$

where, $e_i(k)$ is the error with i =1, 2 and 3, $P_{ij}(k)$ is the measured inter-port power transfer between ports i to port j, where $i, j \in \{1,2,3\}, i \neq j$ and $P_{ij}^*(k)$ is the reference inter-port power.

The adaptive control law is formulated in (5.17) as described in [146].

$$\delta_i(k) = \delta_i(k-1) - \gamma_i \nabla J(k) \tag{5.17}$$

where, $\nabla J(k)$ is the gradient of the cost function $J(k)$ with respect to internal phase shifts and γ_i is a positive adaptive gain.

The quadratic cost function is described as in (5.18).

$$J(k) = \frac{1}{2} e_i^2(k) = \frac{1}{2} \left(P_{ij}(k) - P_{ij}^*(k) \right)^2 \tag{5.18}$$

By taking the gradient of (5.18), the following is obtained:

$$\nabla J = \frac{\partial f(k)}{\partial \delta(k)} = \frac{\partial f(k) \partial P_{ij}^*(k)}{\partial P_{ij}^*(k) \partial \delta(k)} \tag{5.19}$$

For clarity and without loss of generality, further analysis is presented for the first power $P_{12}(k)$. The adaptive control update derived herein can be analogously extended to the

remaining power $P_{23}(k)$ and $P_{31}(k)$ as they follow the same structure. To proceed, the gradient of the cost function is explicitly given as follows:

$$\nabla J(k) = \frac{\partial J(k) \partial P_{ij}^{*}(k)}{\partial P_{ij}^{*}(k) \partial \delta(k)} = \frac{\gamma}{L_{12}^{2}} \left(T_s \sigma_1 A' (L_{12} P_{12}(k) - L_{12} P_{12}^{*}(k) + T_s \sigma_1 A'' - T_s \sigma_1 A''') \right) \tag{5.20}$$

where,

$$A' = cos\delta_2^{*}(k) sin\delta_1^{*}(k) sin\varphi_2(k)$$
$$A'' = cos\delta_1(k) cos\delta_2(k) sin\varphi_2(k)$$
$$A''' = cos\delta_1^{*}(k) cos\delta_2^{*}(k) sin\varphi_2(k)$$

The gradient in (5.20) can be expressed as given in (5.21):

$$\nabla J(k) = \frac{\gamma}{L_{12}^{2}} \left(T_s \sigma_1 A' \left(L_{12} e_1(k) + T_s \sigma_1 (A'' - A''') \right) \right) \tag{5.21}$$

Substitute (5.21) into (5.17) to obtain (5.22):

$$\delta_1(k) = \delta_1(k-1) - \frac{\gamma}{L_{12}^{2}} \left(T_s \sigma_1 A' \left(L_{12} e_1(k) + T_s \sigma_1 (A'' - A''') \right) \right) \tag{5.22}$$

The adaptive gain γ is selected to keep the control system stable and enhance fast convergence. However, there exists a trade-off between a fast convergence and the stability of the system. With Lyapunov direct method, the stability of the adaptive gain selection can be assessed.

5.3.2.3 Stability Analysis

A Lyapunov function $V(k)$ must satisfy the following conditions [147]:

- $V(k)$ is positive definite i.e. $V(k) > 0$
- $\Delta V(k) < 0$, showing the system is asymptotically stable.

To proceed therefore, the chosen Lyapunov function for the system error minimisation is defined as follows:

$$V(k) = e_i^{2}(k) \tag{5.23}$$

The squaring of the error in equation (5.23), satisfies the first condition of Lyapunov stability for all $e(k) > 0$. To satisfy the second criteria, let

$$\Delta V(k) = V(k) - V(k-1) \tag{5.24}$$

As discussed, for simplicity, the first power expression is utilised with all others following the same pattern. Hence, expressing $\Delta V(k)$ in terms of e_1 gives (5.25)

$$\Delta V(k) = \left(e_1^2(k)\right) - \left(e_1^2(k-1)\right) \tag{5.25}$$

This error $e_1(k)$ in the current time step can be expressed in terms of the change in error $\Delta e_1(k)$ as follows:

$$e_1(k) = e_1(k-1) + \Delta e_1(k) \tag{5.26}$$

Substitute (5.26) into (5.25) to get (5.27):

$$\begin{aligned} \Delta V(k) &= \left(e_1(k-1) + \Delta e_1(k)\right)^2 - \left(e_1^2(k-1)\right) \\ &= \Delta e_1^2(k) + 2\Delta e_1(k) e_1(k-1) \end{aligned} \tag{5.27}$$

Based on the definition of $e_1(k)$ in (5.13), the change in error can be expressed as follows:

$$\Delta e_1(k) = (P_{12}(k) - P_{12}(k-1)) + (P_{12}^*(k-1) - P_{12}^*(k)) \tag{5.28}$$

Therefore, the definitions of the actual and reference powers in (5.12) are substituted into (5.28) and the result is expressed using the adaptive update law in (5.22).

$$\Delta e_1(k) = (P_{12}(k) - P_{12}(k-1)) + (P_{12}^*(k-1) - P_{12}^*(k)) \tag{5.29}$$

Furthermore, by substituting (5.29) into (5.27), $\Delta V(k)$, is expressed as:

$$\Delta V(k) = \frac{-\gamma T_s \sigma_1 A'}{L_{12}^4}\left((2L_{12} - \gamma T_s \sigma_1 A')\left(L_{12} e_1(k) + T_s \sigma_1 (A'' - A''')\right)^2\right) \tag{5.30}$$

Focusing on the dominant structural parameters and for analytical simplicity, A' is assumed to be normalised to unity. Additionally, assuming $\delta_1(k) \approx \delta_1^*(k)$ and $\delta_2(k) \approx \delta_2^*(k)$, (5.30) simplifies to:

$$\Delta V(k) = \frac{-\gamma T_s \sigma_1 (2L_{12} - \gamma T_s \sigma_1)}{L_{12}^2} \tag{5.31}$$

Extracting the scalar coefficient of γ in (5.31), gives a constant C:

$$C = \frac{-\gamma T_s \sigma_1}{L_{12}^2} \tag{5.32}$$

With the aid of (5.32), (5.31) can be expressed in the form: $-C \times (2L_{12} - C)$. To guarantee that $\Delta V(k) < 0$, the inequality $0 < C < 2$ needs to be fulfilled. Thus, the range of values of the adaptive gain γ, used to ensure stability satisfies:

$$0 < \gamma < \frac{2L_{12}^2}{T_s \sigma_1} \tag{5.33}$$

In addition, to improve convergence speed dynamically, the adaptive gain can be modified to vary with the system's operating conditions. This adaptive auto tuning is expressed as:

$$\gamma_i = \gamma_0 \frac{1}{1 + \tau e_i} \tag{5.34}$$

where, $\tau > 0$ is constant scaling factor and $\gamma_0 > 0$ is an initial value of the adaptive gain.

The online adaptive process is represented in Fig. 5.7 illustrating the iterative control algorithm used to dynamically adjust the internal phase shifts. The process begins with the reference inputs for current and voltage at each port and parameter initialisation. The system then measures the actual phase shifts, current, and voltage values, which are used to compute the active inter-port power flow. Based on the computed power balance, the control algorithm determines the errors and applies the adaptive control law to update the internal phase shifts. The process iterates continuously, refining the phase shifts in response to system variations through an adaptive gain mechanism.

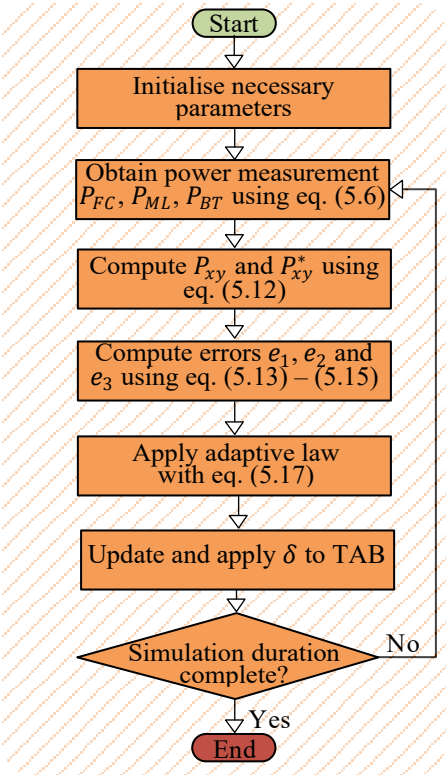

Fig. 5.7: Adaptive control law flow chart.

5.4 Simulation Validations

The The proposed L-TPS control technique is validated through simulations conducted in the MATLAB/Simulink environment, as illustrated in Fig. 5.4. The electrical specifications of the TAB converter and corresponding controller gains, designed for an all-electric vessel rated at 0.5 MW, with a switching frequency of 10 kHz and sampling time of 5e-7 s are listed in Table 5.1. In the proposed TAB system, comprising the BT, FC and ML load, the control technique is employed such that the FC operates as the primary source supplying a constant power output with 60 cells. The battery functions as a bidirectional buffer, which can absorb or supply the power difference based on load variations. This method ensures a steady operation of the FC, thereby enhancing its lifespan and fuel efficiency and leverages the dynamic response capability of the battery. The control technique assumes that the battery's state of charge (SoC) remains within its allowable operational range (SoC =70 %), enabling both charging and discharging actions as required to maintain the system power balance. The rated capacity of the BT is set at 200 Ah.

Table 5.1. Converter Specifications

Description	Symbol	Unit	Ports		
			#1	#2	#3
Voltage rating	V_{BT}, V_{FC}, V_{ML}	kV	0.75	0.75	0.75
Current	I_{BT}, I_{FC}, I_{ML}	kA	0.17	0.50	0.67
Leakage inductance	L_1, L_2, L_3	µH	5.62	5.62	5.62
LC filter inductance	L_{f1}, L_{f2}	µH	680	290	-
LC filter capacitance	C_{f1}, C_{f2}, C_{f3}	µF	330	780	1110
LADRC	k_p	-	-	0.54 e6	0.51 e3
	k_d	-	-	0.31 e3	0.30 e3
	w_o	rad/s	-	1.20 e4	1.10 e4
	b_0	-	-	7.05 e9	1.30 e7

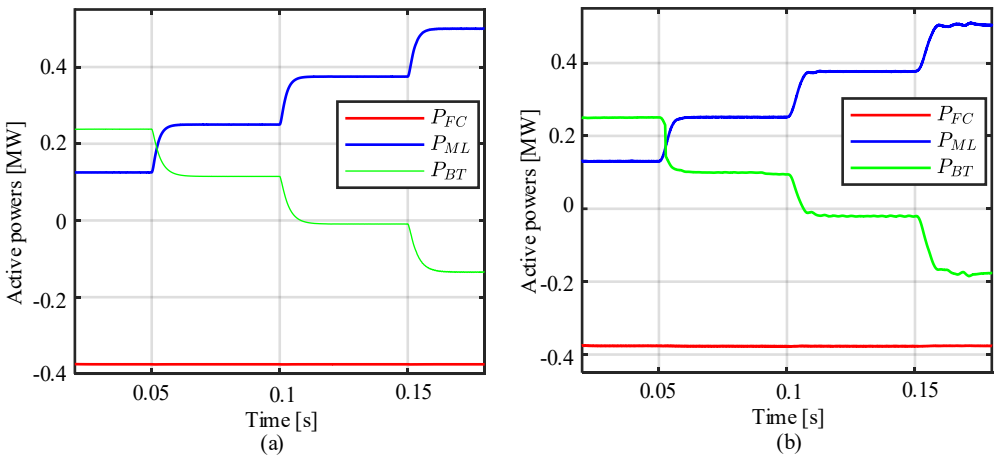

Fig. 5.8.FC supplying constant power under step ML load changes, with BT balancing power using the proposed L-TPS method (a) With optimised LADRC with PSO as external phase shift control (b) With model reference-based hybrid decoupling control as external phase shift control.

5.4.1 Results

The typical power flow among the three ports under the proposed L-TPS control technique is depicted in Fig. 5.8. Negative power values indicate power supply by a port, while positive values represent power absorption. The figure illustrates step changes in the ML load at 25 %, 50 %, 75 %, and 100 % of its rated capacity, with the maximum load set at 0.5 MW. Throughout these step changes, the FC constantly supplies 75 % of the rated power, while the BT charges and discharges, balancing the power mismatch at each load variation.

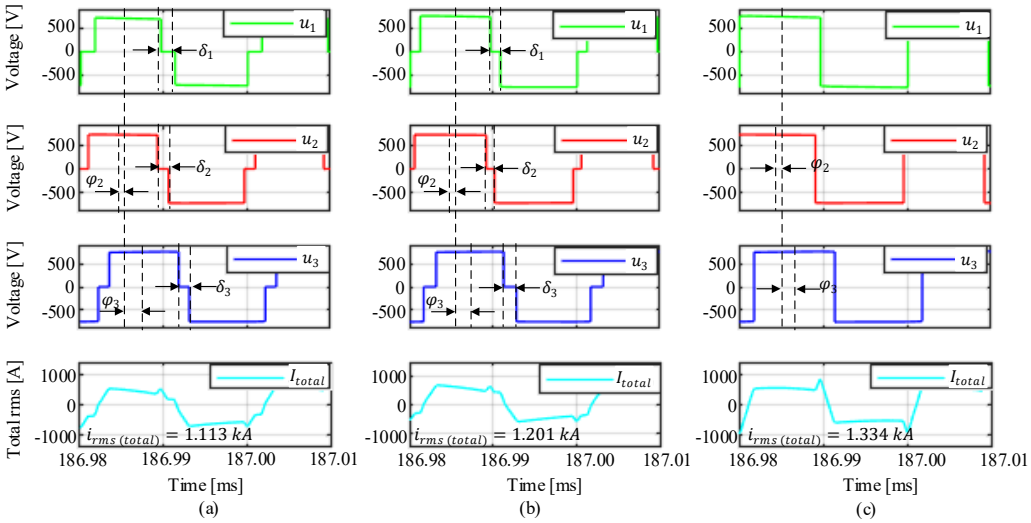

Fig. 5.9. Plot of midpoint voltages and the sum of inductor currents for (a) proposed L-TPS method (b) conventional TPS method (c) SPS control.

Table 5.2. Calculated values of the degree of freedoms

Degrees of freedom		Proposed L-TPS Method	Conventional TPS Method	SPS
External Phase Shifts	φ_2	-8.96 °	-11.76 °	-10.50 °
	φ_3	35.70 °	35.00 °	32.50 °
Internal Phase Shifts	δ_1	23.44 °	20.50 °	–
	δ_2	25.65 °	21.80 °	–
	δ_3	29.55 °	27.40 °	–

Firstly, to demonstrate that either of the two proposed decoupling controllers can be employed as the external phase-shift control, Fig. 5.8 presents the overall power-flow behaviour when using the optimised LADRC (Fig. 5.8a) and the model-reference-based decoupling control (Fig. 5.8b) as the external phase-shift control. In both cases, following each step change, the FC consistently returns to a stable power-supply level after only a negligible transient, indicating that cross-coupling has been effectively minimised. Consequently, variations in the ML load and BT ports do not compromise FC output stability. A slight oscillation observed in Fig. 5.8b may be attributed to PD-arm tuning (derivative gain), which is typically mitigated by appropriate low-pass filtering or conservative derivative gain selection.

Subsequently, the performance of the proposed L-TPS (with optimised LADRC as external phase shift control) method is benchmarked against two existing methods. Firstly, the method outlined in [24], is henceforth referred to as the conventional TPS control technique. This method utilises a decoupling matrix with a proportional integral controller in each external phase shift control loop. Subsequently, partial gradient estimate optimisation is employed to optimise three internal phase shifts, aiming to reduce the inductor rms current and enhance efficiency. The second method is SPS control without the implementation of internal phase shifts as described in [30].

The magnified waveforms of the midpoint voltages and the total rms values of the inductor currents are illustrated in Fig. 5.9. The BT and FC ports exhibit quasi-square voltage waveforms, with peak values corresponding to the input voltage. Similarly, the ML port displays quasi-square waveforms aligned with the load voltage magnitude under both the proposed L-TPS and conventional TPS methods. In contrast, the SPS control technique produces a square waveform at all ports. Across all three control techniques, the sum of inductor rms currents follow a trapezoidal waveform. These observed waveform patterns are consistent with expected behaviours under internal and external phase shift control, with the corresponding calculated phase shift values summarised in Table 5.2 at full load when P_{FC} = 0.75 rated power. The external lagging phase is indicated by the negative sign. Additionally, as shown in Fig. 5.9, the sum of the inductor rms current for the proposed L-TPS control technique is 1.11 kA, whereas the recorded sums for the conventional TPS and SPS control technique are 1.20 kA and 1.33 kA, respectively (Fig. 5.9). Depicting that the proposed L-TPS achieves the lowest rms current.

Furthermore, Fig. 5.10 illustrates how the internal phase shifts of the proposed L-TPS controller dynamically adjust in response to step changes in the power absorbed by the ML port demonstrating the controller adaptive capability. The internal phase shifts corresponding to the specific operating point are calculated to ensure optimal power flow regulation. In addition, to enhance the dynamic response, the adaptive gains are updated online following an initial manual selection. This enables the controller to respond more effectively to varying operating conditions, further balancing speed and stability, as illustrated in Fig. 5.11, which shows the real-time values of the adaptive gains.

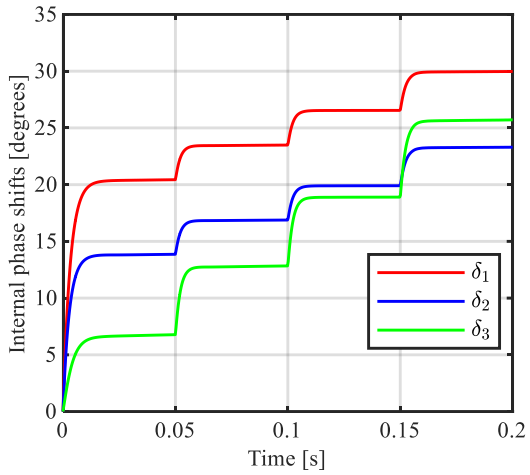

Fig. 5.10. Internal phase shifts at each step change in the power absorbed by the ML load with $\boldsymbol{P_{FC}}$ *= 0.75 rated power*

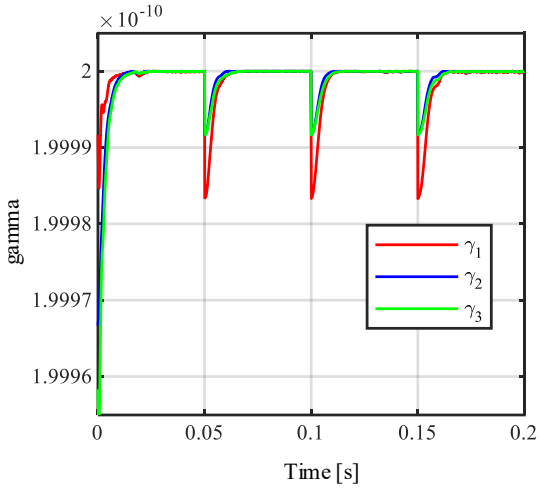

Fig. 5.11. Dynamic behaviour of the adaptive gains when $\boldsymbol{\tau}$ *is 1e-9.*

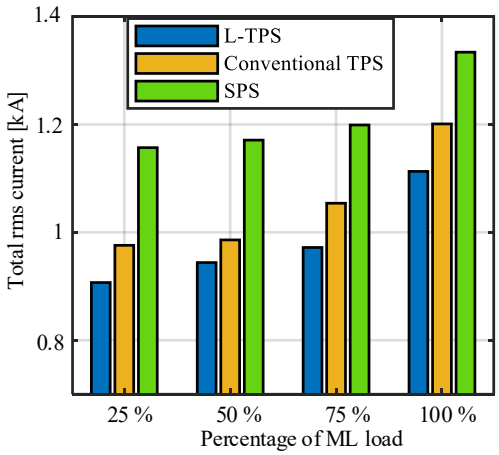

Fig. 5.12. Sum of the rms value of the inductor currents as a function of $\boldsymbol{P_{FC}}$.

5.4.2 Analysis

The total inductor rms current is computed for all controllers under investigation. This is carried out with varying proportions of the ML load as a function of the FC power supply to understand the impact of load variations on the converter loss estimation. The total rms values of the inductor current are as shown in Fig. 5.12. A greater rms value of the inductor current is noted in the SPS control across all ML load cases since it is with a limited degrees of freedom compared to both the conventional TPS and proposed L-TPS control techniques.

Compared to conventional TPS methods for optimising additional degrees of freedom, the proposed L-TPS control technique offers a more efficient solution. As shown in Table 5.3 the execution time measured using tic/toc command in MATLAB was 225 s, which is as expected more than the SPS control but less than the conventional TPS method.

Table 5.3. Execution time

Method	Execution time [s]
SPS	182.00
Conventional TPS	236.00
Proposed L-TPS	225.00

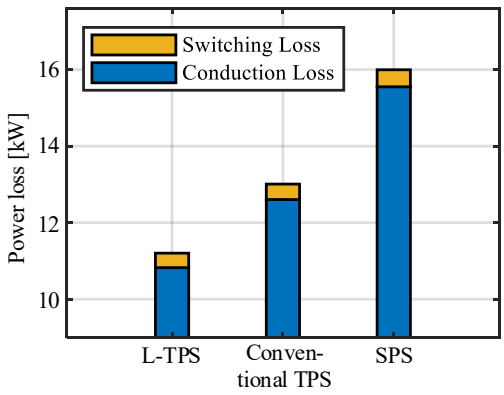

Fig. 5.13. Conduction losses at 100 % ML load.

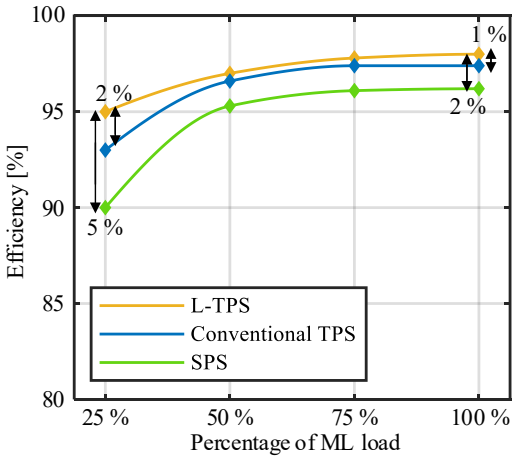

Fig. 5.14. Efficiency plots with percentages of the ML load.

Conduction power loss in the converter is primarily determined by the rms current flowing through the switching devices and is given by $P_c = I_{rms}^2 R_{on}$, where R_{on} is the on-state resistance of the switches. Similarly, the switching loss is calculated from [148]:

$$P_{sw(T)} = f_s * E_{on+off} * \left(\frac{I_{rms}}{I_{ref}}\right)^{k_i} * \left(\frac{V_{rated}}{V_{ref}}\right)^{k_v} * \left(1 + TC_{Esw} * \left(T_j - T_{ref}\right)\right) \quad (5.35)$$

where, E_{on+off} is sum of the turn on and turn off energies, V_{ref} and I_{ref} are the voltage and current reference obtained from data sheet, K_v and k_i are the exponents for the voltage and current dependency of switching losses and TC_{Esw} is the temperature coefficient of switching losses. To estimate the total losses, the cumulative total rms currents are utilised the device parameters obtained from the Wolfspeed SiC module CAB6R0A23GM4 datasheet. Fig. 5.13 illustrates both the conduction and switching losses at maximum ML load conditions for all control techniques. The proposed L-TPS control achieves the lowest losses of 11.20 kW, compared to 13.01 kW for the conventional TPS and 16.00 kW for the SPS control. These results demonstrate the improved loss minimisation performance of the L-TPS control technique.

An efficiency plot for the proposed L-TPS control technique, the conventional TPS control technique, and the SPS control is shown in Fig. 5.14. It can be observed from all the controllers that there is a significant efficiency drop at lighter power loads. However, in all

loading scenarios, the power converter with the proposed L-TPS control technique has a higher efficiency. All controllers performed better at full load with the proposed L-TPS technique exhibiting a 1 % efficiency improvement over the conventional TPS controller and a 2 % efficiency improvement over the SPS control but more significantly a 2 % efficiency increase compared to the conventional TPS technique, and 5 % increase compared to the SPS control at light load (25 % of the load).

To further demonstrate the features and advantages of the proposed L-TPS control technique, a quantitative comparison is presented against the benchmarked control techniques, as summarised in Table 5.4. The comparison focuses on system losses (expressed in percentage loss compared to the SPS method), optimisation objective, controller complexity and efficiencies. A notable observation, typical of isolated converters, is the tendency to exhibit increased losses under light load conditions due to deviation from the designed voltage gain ratio, this effect is less pronounced at full load. From the results in Table 5.4, the proposed L-TPS control technique consistently outperforms its counterparts under both light and full load conditions. Moreover, in terms of control complexity, which includes computational burden and modelling requirements, the proposed L-TPS control technique demonstrates a more efficient implementation. Finally, the proposed L-TPS control technique exhibits enhanced adaptability, responding effectively to changes in operating conditions. This adaptive behaviour enables improved robustness and reduced system losses by dynamically updating control variables in response to real-time system variations.

Table 5.4. Advantages of the proposed L-TPS method over benchmarked control techniques

Criteria	Proposed L-TPS	Conventional TPS	SPS
System loss at full load	30 % lower than SPS	18 % lower than SPS	High
Converter efficiency at full load	98 %	97 %	96 %
Optimisation objective	Minimisation of inter-port power flow tracking error	Inductor rms current reduction	NA
Converter efficiency at light load (25 % of load)	95 %	93 %	90 %
Adaptability to varying load conditions	High	Medium	Low
Controller complexity (Number of offline calculations. modelling etc.)	Low	Medium	Low

5.5 Experimental Validations

To validate the effectiveness of the proposed L-TPS control technique, a 100 W proof-of-concept experimental prototype of the TAB converter is designed, developed, and tested. A scaled-down version of the converter is shown in Fig. 4.9. The experimental evaluation focuses on assessing the loss-minimisation capability of the L-TPS method, using online adaptive internal phase shift calculations. Its performance is compared against benchmark control techniques.

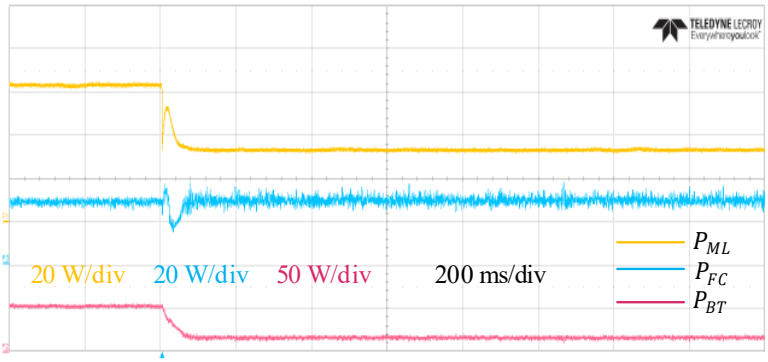

Fig. 5.15. Typical experimental power flow response to a ML load step change, with the corresponding power variation on the BT port, while the FC port maintains a constant power supply.

The voltage sources are configured such that the BT port is set to 40 V, the FC port is set to 20 V, and the load connected to the ML port has a resistance of 10 Ω. Fig. 5.15, shows the active output power flow when the ML load undergoes a step change from 10 Ω to 20 Ω, hence the BT port adjusts its power output accordingly, while the FC port maintains a constant power supply.

During normal operation, before the step change, the midpoint voltages for these three methods are shown in Fig. 5.16. These results validate the quasi-square waveform achieved by both the proposed L-TPS and conventional TPS methods, which incorporate internal phase shifts, in contrast to the square waveforms produced by the SPS control, which lacks internal phase shift. Additionally, before the step change, the current waveforms for these control techniques are shown in Fig. 5.17. It is evident that the total rms current is significantly reduced. Compared to the SPS control technique, the conventional TPS method achieves a 39 % reduction, while the proposed L-TPS method achieves a 49 % reduction.

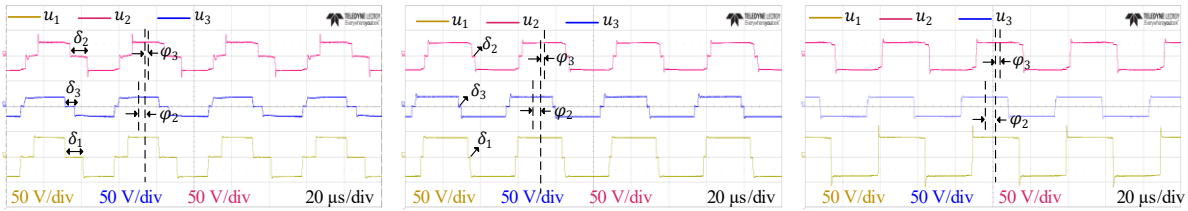

Fig. 5.16. Experimental plots of midpoint voltages for (a) proposed L-TPS technique (b) conventional TPS technique (c) SPS control technique.

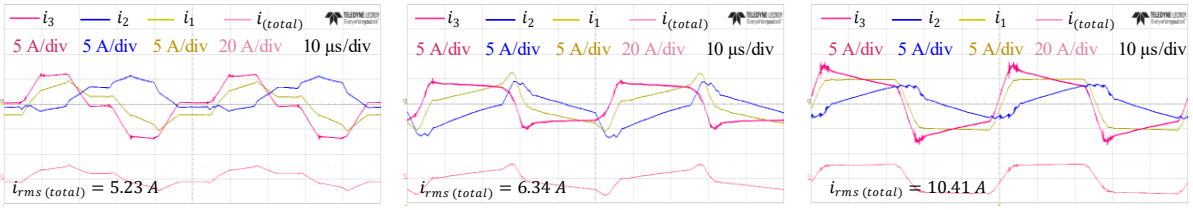

Fig. 5.17. Experimental plots of inductor currents for (a) proposed L-TPS technique (b) conventional TPS technique (c) SPS control technique.

Moreover, the proposed L-TPS method offers a 17 % improvement over the conventional TPS method in terms of rms current reduction. With an efficiency of 83 %, the proposed L-TPS method outperforms the conventional TPS and SPS control techniques, which achieve efficiencies of 81 % and 79 %, respectively, thereby highlighting its improved control performance.

5.6 Summary

To overcome the limitations of conventional SPS control, particularly its limited ability in independently regulating inter-port power flow, which often leads to reduced overall operational system efficiency, this chapter implemented a TPS control through the integration of three internal phase shifts. An online adaptive control based on the steepest descent method, was implemented to achieve this enhancement. The stability of the adaptive gain was analysed using the Lyapunov direct method. The proposed method begins by establishing a predetermined inter-port active power reference, which is continuously compared with the actual measured power. The internal phase shifts were then dynamically adjusted to minimise the error between the reference and actual power values, using an adaptive gain that updates online in response to changing operating conditions. Simulation results demonstrated a significant reduction in the converter losses, achieving a 14 %

reduction compared to conventional TPS and 30 % reduction compared to SPS control, at full load. Experimental validation further confirmed the effectiveness of the proposed L-TPS control technique, showing a 2 % efficiency improvement over conventional TPS and a 4 % improvement over SPS control. These findings highlight the potential of the proposed L-TPS method to significantly enhance the operational efficiency of the multiport isolated DC–DC converter systems.

Chapter 6

Conclusions and Future research

This chapter presents a summary of the research, draws conclusions on the control of multiport-isolated DC-DC converters for hydrogen energy systems, highlights the author's main contributions, and provides insights into future research directions.

6.1 General Conclusions

This thesis has focused on developing control techniques to enhance the performance of multiport-isolated DC-DC converters, particularly the triple active bridge (TAB) converter, for hydrogen energy systems. The research has been applied across three main configurations: offshore wind-based hydrogen energy storage systems, onshore hydrogen production system and hydrogen energy systems for marine applications. The overall aim was to develop an improved power electronic converter (PEC) interface that enhances power flow control and increases its overall efficiency for hydrogen energy systems applications. To achieve this, novel decoupling and advanced control techniques were proposed and evaluated.

In Chapter 3, a novel decoupling control technique, termed the model reference-based hybrid decoupling control, was introduced. This decoupling control technique first utilises an ideal model with zero non-diagonal elements as a reference and forces the converter's matrix model to replicate this behaviour. It further integrates the best-performing matrix-based decoupling control technique, identified from the comparative analysis of three matrix-based decoupling control techniques presented in Chapter 2. A detailed mathematical analysis of the decoupling control design was carried out and validated through MATLAB/Simulink simulations and hardware experimental test rig. The results show a:

- 3 % efficiency compared to the best performing matrix-based decoupling control
- maximum cross-coupling effect of 3 % at the worst case scenario
- displayed ability to perform better in a wider operating region.

In chapter 4, an enhanced linear active disturbance rejection controller (LADRC) was developed and implemented as a decoupling control technique, leveraging the controller's inherent capability to reject both internal and external disturbances. This technique aims to

simplify the controller's design process by automatically determining the controller gains, which are typically tuned manually and often result in suboptimal decoupling performance. The proposed technique employed the particle swarm optimisation (PSO) algorithm to determine the converter gains offline, with the objective of minimising estimation errors within the controller. Simulation and experimental validation of the LARDC was performed. The key findings include:

- A detailed analysis of the LADRC controller gains tailored to the TAB converter was conducted, where minimising the estimation error served as the objective function in the optimisation.
- The PSO-based optimisation slightly outperformed the benchmarked Genetic Algorithm (GA) due to its advantageous convergence characteristics, although either or other optimisation algorithms capable of solving nonlinear problems could be applied.
- A maximum cross-coupling effect of 5 % was observed under the worst case scenario.

Chapter 5 presented the third and final control technique developed to enhance the performance of the multiport-isolated DC-DC converter. The proposed controller employed the triple-phase-shift (TPS) modulation technique to address the limitations of single-phase-shift (SPS) modulation by simultaneously implementing the three internal and two external phase shifts of the converter. Simulation and experimental validations were carried out, with comparisons made against selected benchmark control techniques in terms of convergence speed, system losses, and overall efficiency. Key findings include

- Implementation of an online adaptive steepest descent control technique for determining and dynamically adjusting the three internal phase shifts based on inter-port power flow error.
- Detailed mathematical analysis using the Lyapunov direct method to establish the range of adaptive gains that ensure system stability.
- A comparative study with other benchmarked techniques revealed improvements such as:
    - 30 % system loss reduction
    - 17 % reduction in rms current.
    - 5 % and 2 % efficiency improvement at light load and full load respectively.

In summary, this thesis has made efforts in enhancing the control performance of a suitable candidate topology for hydrogen energy systems. The proposed control techniques addressed the two key identified challenges of conventional multiport-isolated DC-DC converters, thereby contributing to its development and overall performance in hydrogen energy system applications.

6.2 Highlights of Thesis Contributions

The thesis contributions can be summarised into two main areas as follows:

6.2.1 Decoupling control

- Proposed a novel software-based decoupling control technique that eliminates the reliance on look-up tables, thereby significantly reducing memory requirements.
- Introduced a model reference-based decoupling control technique that minimises the error between the output of an ideal decoupling reference model and the actual plant, thereby enhancing the decoupling control accuracy.
- Proposed a hybrid decoupling control structure that integrates a decoupling matrix into the model reference-based framework, synergises their strengths to achieve robust decoupling and mitigates cross-coupling effects across a wider operating region.
- Introduced an offline particle swarm optimisation to determine the optimal gains of LADRC without imposing additional computational burden on the controller. The identified optimal gains simplify the controller design process, bypassing the subjective nature of manual tuning techniques. The determined gains are optimised to minimise the observer's estimation error, ensuring effective decoupling control performance and maintaining minimal estimation inaccuracies.

6.2.2 Loss Minimisation

- Developed an adaptive control technique based on the steepest descent method to minimise the deviation between precalculated and actual inter-port active power flow. Introduced real-time dynamic adjustment of internal phase shifts to improve speed of convergence.

- Ensured adaptive gain stability through the implementation of a Lyapunov direct method, identifying feasible operating regions.

6.3 Future Work

The following areas can be explored as potential future research work

- In offshore wind farm HESS applications, an evaluation of the AC/DC converter's performance is required, focusing on improving efficiency, power factor, and reducing harmonic distortion to achieve better overall performance in offshore wind farm HESS applications.

- Building on the enhanced LADRC control developed, which effectively uses offline PSO-based optimisation to determine controller gains and minimise estimation error, a potential future work is to explore adaptive online gain tuning. The goal would be to maintain the same high decoupling performance and low estimation error while further increasing the controller's adaptability to real-time variations in operating conditions. The study would focus on methods to implement online gain adjustment without adding significant computational burden or compromising stability, thereby extending the capabilities of the current LADRC-based decoupling control.

- To further increase the flexibility of the converter's application, an investigation can be carried out on the configuration of the TAB where one bridge of the multiport converter interfaces with both a FC and a battery, while the other bridges interface with DE and an EL via a Quasi-Z-Source Inverter (QZSI). With a focus on developing a coordinated control technique to mitigate discontinuous and pulsating currents, ensuring stable operation and utilising the battery to compensate for the FC's slow dynamic response, providing faster power support during a dynamic operation.

- A deeper evaluation of switching losses is essential, particularly focusing on Zero-Voltage Switching (ZVS) and Zero-Current Switching (ZCS). This will help optimise the converter efficiency and reduce thermal dissipation.

- It is proposed to investigate an additional loss minimisation technique for the multiport converter, focusing on the reduction of reactive power. Reactive power, which remains within the converter legs without performing useful work, contributes to increased circulating currents and thermal stress in power devices. A mathematical

model of the converter's reactive power can be developed with impacts examined on both device and system level and an advanced control technique can be designed to mitigate this effect, thereby improving overall efficiency and reducing device heating.

- The converter can be tested at the system level with real prototypes of the EL and FC to assess the effectiveness of the enhanced control techniques and communication between all components in the HESS, ensuring smooth operation and integration.

Appendix A

List of Figures

Appendix B

List of Tables

Appendix C

Experimental Test Rig

This appendix presents a description of the experimental setup in the laboratory. The set up is a scaled down version of the TAB converter. The picture in Fig. C.1 shows the experimental set up.

C.1 Half-Bridge Submodule

The Fig. C.2 illustrates the schematic of a half-bridge submodule. This submodule is made of these main components:

- 1 Optocoupler: 6N139
- 1 Gate Drives: IR2111
- 2 Isolated DC-DC Converters: TME 1212S
- 2 MOSFETs: IRFP460APBF

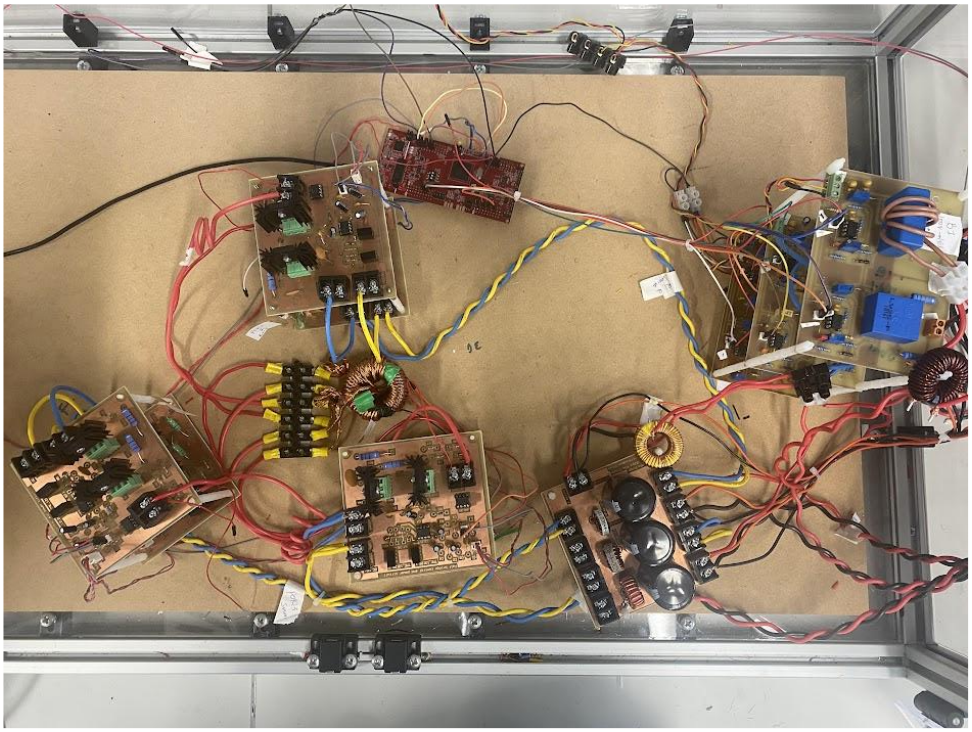

Fig. C.1. Experimental setup

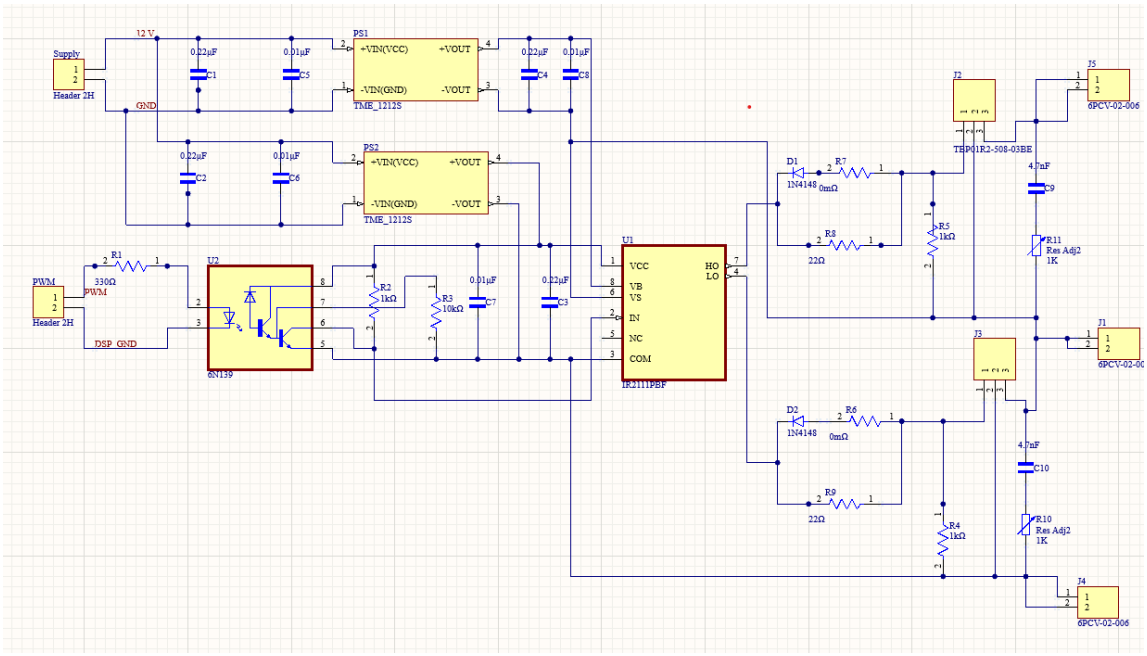

Fig. C.2. A half bridge submodules schematic

Two half-bridges are connected to form a full-bridge such that the high-side switches of both half-bridges are connected to the positive supply, while the low-side switches are connected to ground. The midpoints of the half-bridges (i.e., the nodes between the high-side and low-side switches) are connected to the two end windings of one port of the three-port transformer. In all, six half-bridges are connected to form the TAB.

C.2 Multiwinding transformer

The picture in Fig.C.3 shows the multiwinding transformer:

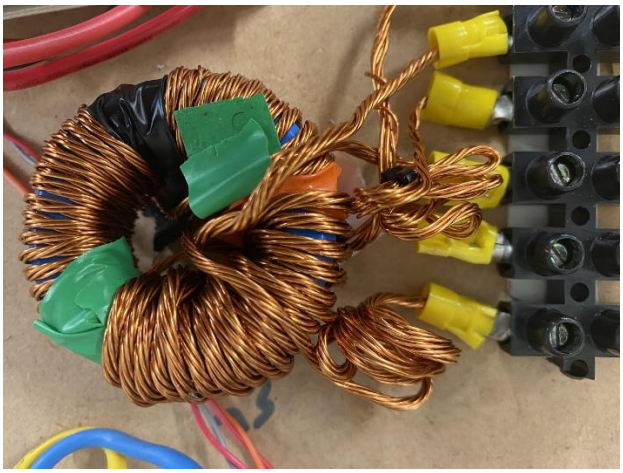

Fig. C.3. Multiwinding transformer

Fig. C.4. DSP

The transformer core as shown in Fig. C.3. is a toroidal ferrite Core R 50/30/20 N87, with a selected turns ratio of 16:10:15. The calculated leakage inductances are L_1 = 11 µH, L_2 = 12 µH and L_3 = 17 µH.

C.3 DSP

In the development of TAB converter prototype, a DSP serves as the central control unit. The DSP used is the TMS320F28379D as shown in Fig C.4. Its main function is to generate precise gating signals for the power switches based on the control law, typically developed and deployed via a Simulink model. Additionally, the DSP performs real-time data acquisition by converting analog feedback signals, such as voltages and currents, into digital form through its onboard ADC. This enables closed-loop control of the converter.

The choice of the DSP is informed by the following attributes

- It has 24 channels of 12-bit / 16-bit analogue to digital converter.
- Up to 24 enhanced PWM.
- It has a seamless integration with MATLAB/Simulink.
- Fast processing speed (200 MHZ).
- High performance 32-bit central processing unit.

C.4 Voltage and Current Sensors

Fig. C.5 shows the pictures of the voltage and current measurement boards used in the experimental setup. The voltage board is implemented to measure the output voltage and

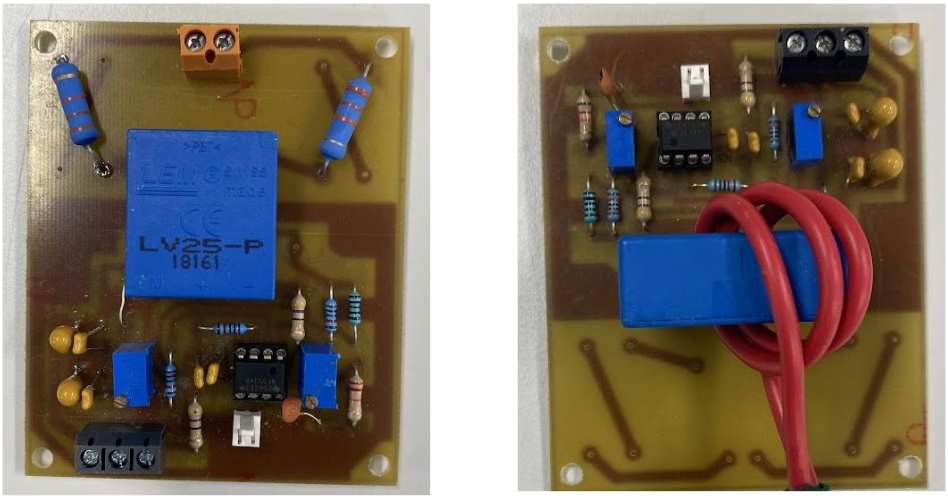

Fig.C.5. Voltage and current measurement boards

feeds the measurement signal to the DSP's ADC module. It typically scales the input voltage and adds a dc-bias to make the output voltage suitable for the ADC signal level. The sensor (LEM LV25-P) is implemented, which can measure up to 500 V with high frequency bandwidth. The LEM25-P data sheets is as shown in Fig.C.6.

LEM

Voltage Transducer LV 25-P

For the electronic measurement of currents: DC, AC, pulsed..., with galvanic isolation between the primary circuit and the secondary circuit.

16084

I_{PN} = 10 mA
V_{PN} = 10 .. 500 V

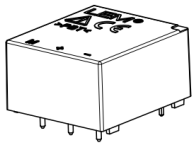

Electrical data

I_{PN}	Primary nominal current rms		10		mA
I_{PM}	Primary current, measuring range		0 .. ± 14		mA
R_M	Measuring resistance		$R_{M\,min}$	$R_{M\,max}$	
	with ± 12 V	@ ± 10 mA $_{max}$	30	190	Ω
		@ ± 14 mA $_{max}$	30	100	Ω
	with ± 15 V	@ ± 10 mA $_{max}$	100	350	Ω
		@ ± 14 mA $_{max}$	100	190	Ω
I_{SN}	Secondary nominal current rms		25		mA
K_N	Conversion ratio		2500 : 1000		
V_C	Supply voltage (± 5 %)		± 12 .. 15		V
I_C	Current consumption		10 (@ ± 15 V) + I_S		mA

Accuracy - Dynamic performance data

X_G	Overall accuracy @ I_{PN}, T_A = 25°C @ ± 12 .. 15 V	± 0.9	%
	@ ± 15 V (± 5 %)	± 0.8	%

Features

- Closed loop (compensated) current transducer using the Hall effect
- Isolated plastic case recognized according to UL 94-V0.

Principle of use

- For voltage measurements, a current proportional to the measured voltage must be passed through an external resistor R_1 which is selected by the user and installed in series with the primary circuit of the transducer.

Fig.C.6. Voltage sensors specification.

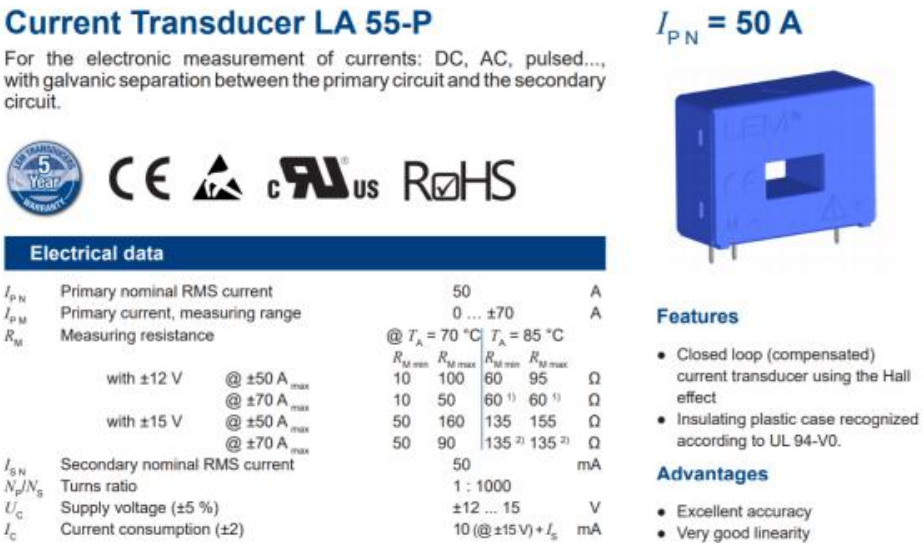

Current Transducer LA 55-P

For the electronic measurement of currents: DC, AC, pulsed..., with galvanic separation between the primary circuit and the secondary circuit.

I_{PN} = 50 A

Electrical data

I_{PN}	Primary nominal RMS current				50			A
I_{PM}	Primary current, measuring range				0 ... ±70			A
R_M	Measuring resistance		@ T_A = 70 °C		T_A = 85 °C			
			$R_{M\,min}$	$R_{M\,max}$	$R_{M\,min}$	$R_{M\,max}$		
	with ±12 V	@ ±50 A$_{max}$	10	100	60	95		Ω
		@ ±70 A$_{max}$	10	50	60 [1]	60 [1]		Ω
	with ±15 V	@ ±50 A$_{max}$	50	160	135	155		Ω
		@ ±70 A$_{max}$	50	90	135 [2]	135 [2]		Ω
I_{SN}	Secondary nominal RMS current				50			mA
N_P/N_S	Turns ratio				1 : 1000			
U_C	Supply voltage (±5 %)				±12 ... 15			V
I_C	Current consumption (±2)				10 (@ ±15 V) + I_S			mA

Features

- Closed loop (compensated) current transducer using the Hall effect
- Insulating plastic case recognized according to UL 94-V0.

Advantages

- Excellent accuracy
- Very good linearity

Fig.C.7. Current sensors specification.

Similarly, the dc-output currents are measured and sent to the DSP. The LEM LA 55-P is implemented to construct the current measurement board. The LEM LA 55-P is sensible within the range 0 A – 50 A, with accuracy bandwidth of 200 kHz, its datasheet is as shown in Fig.C.7.

The sensors are implemented with a conditioning circuit as shown in Fig.C.8. for both voltage and current.

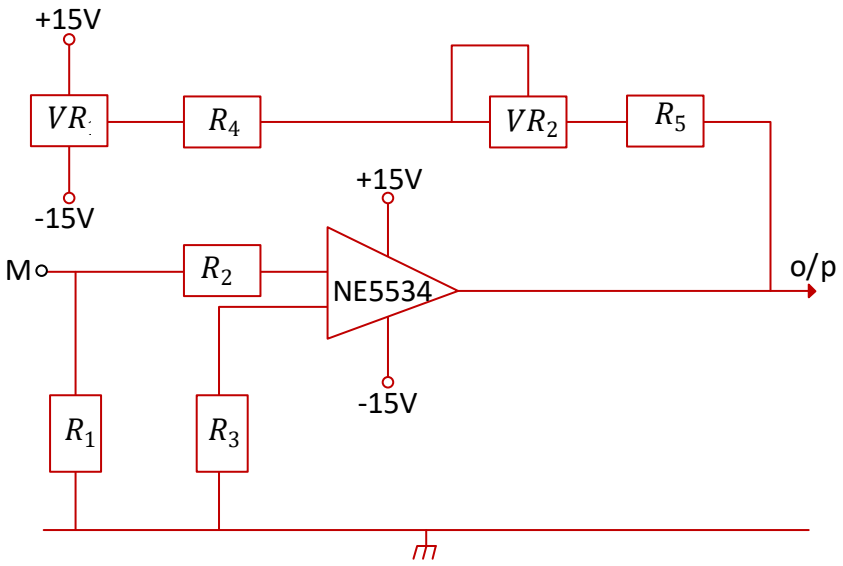

Fig. C.8 Conditioning circuits for voltage and current

For the two circuits, the resistor network is given as

$$R_2 = R_3 = R_4 = 12\ k\Omega$$

$$VR_1 = VR_2 = 10\ k\Omega$$

where, R_2, R_2, R_2 are fixed value and VR_1 used for offset adjustment and VR_2 used for gain adjustment are variable resistors.

$$Gain = \frac{VR_2 + R_5}{R_2}$$

A gain less than one is desirable to minimise noise amplification. Hence, R_5 is chosen as 5 kΩ. For a gain value of 0.6.

For the current sensor specific calculations, to match the ADC 3.3 V range of the ADC

$$\frac{NI}{1000}.R_1.Gain = 3.3\ V$$

with R_1 given from the specification of the sensors to be in the range 135 Ω – 155 Ω, a value of 150 Ω is selected.

For the voltage sensor specific calculations, to match the 3.3 V range of the ADC, with 10 mA being the primary nominal current, the voltage across the burden resistor will be:

$$V = 10\ \times 2.5 \times R_1 \times Gain$$

From the sensor specification, R_1 is in the range of 100 Ω – 350 Ω, hence, 220 Ω is chosen.

References

[1] P. Droege, *Urban energy transition: from fossil fuels to renewable power*. Elsevier, 2011.

[2] M. J. B. Kabeyi and O. A. Olanrewaju, "Sustainable Energy Transition for Renewable and Low Carbon Grid Electricity Generation and Supply," (in English), *Frontiers in Energy Research,* Review vol. 9, 2022-March-24 2022, doi: 10.3389/fenrg.2021.743114.

[3] J. Lee and F. Zhao, "GWEC : Global wind report 2022," April 4 2022. [Online]. Available: www.gwec.net

[4] R. O'Sullivan and WindEurope, "Wind energy in Europe 2022 - Statistics and the outlook for 2023-2027," February 2023.

[5] C. N. Rasmussen, "Improving wind power quality with energy storage," in *2009 IEEE PES/IAS Conference on Sustainable Alternative Energy (SAE)*, 28-30 Sept. 2009 2009, pp. 1-7, doi: 10.1109/SAE.2009.5534860.

[6] M. Awad *et al.*, "A review of water electrolysis for green hydrogen generation considering PV/wind/hybrid/hydropower/geothermal/tidal and wave/biogas energy systems, economic analysis, and its application," *Alexandria Engineering Journal,* vol. 87, pp. 213-239, 2024/01/01/ 2024, doi: https://doi.org/10.1016/j.aej.2023.12.032.

[7] P. Breeze, "Chapter 8 - Hydrogen Energy Storage," in *Power System Energy Storage Technologies*, P. Breeze Ed.: Academic Press, 2018, pp. 69-77.

[8] Q. Jia *et al.*, "Harnessing hydrogen energy storage for renewable energy stability in China: A path to carbon neutrality," *International Journal of Hydrogen Energy,* vol. 118, pp. 93-101, 2025/04/10/ 2025, doi: https://doi.org/10.1016/j.ijhydene.2025.03.213.

[9] Z. Xie, Q. Jin, G. Su, and W. Lu, "A Review of Hydrogen Storage and Transportation: Progresses and Challenges," *Energies,* vol. 17, no. 16, p. 4070, 2024. [Online]. Available: https://www.mdpi.com/1996-1073/17/16/4070.

[10] L. Fernández, "Annual wind power generation for electricity and heat in the United Kingdom (UK) from 2000 to 2022," Nov 22 2023. [Online]. Available: https://www.statista.com/statistics/223328/uk-wind-power-generation/#statisticContainer

[11] V. Stori and C. E. S. Alliance, "Offshore Wind to Green Hydrogen Insights from Europe," October 2021 2021.

[12] S. Government, "Offshore wind to green hydrogen: opportunity assessment," 21 December 2020. [Online]. Available: https://www.gov.scot/publications/scottish-offshore-wind-green-hydrogen-opportunity-assessment/pages/1/

[13] L. Wan, W. Zhang, and Z. Xu, "Overview of Key Technologies and Applications of Hydrogen Energy Storage in Integrated Energy Systems," in *2020 12th IEEE PES Asia-Pacific Power and Energy Engineering Conference (APPEEC)*, 20-23 Sept. 2020 2020, pp. 1-5, doi: 10.1109/APPEEC48164.2020.9220454.

[14] D. hydrogen. "The global opportunity." https://www.dolphynhydrogen.com/where-we-are (accessed July 6, 2024).

[15] Y. D.J., "Fuel Cell Solution for Marine Applications," presented at the International Conference on Hydrogen Safety, Edinburgh, Scotland, 21--24 September 2021, 2021. [Online]. Available: hysafe.info/uploads/papers/2021/31.pdf.

[16] Z. Islam Rony *et al.*, "Alternative fuels to reduce greenhouse gas emissions from marine transport and promote UN sustainable development goals," *Fuel,* vol. 338, p. 127220, 2023/04/15/ 2023, doi: https://doi.org/10.1016/j.fuel.2022.127220.

[17] I. Hussain, H. Wang, M. Safdar, Q. B. Ho, T. D. Wemegah, and S. Noor, "Estimation of Shipping Emissions in Developing Country: A Case Study of Mohammad Bin Qasim Port, Pakistan," *International Journal of Environmental Research and Public Health,* vol. 19, no. 19, p. 11868, 2022. [Online]. Available: https://www.mdpi.com/1660-4601/19/19/11868.

[18] L. E. Klebanof, T. K. Drube, J. M. Gerlach, and T. S. Leach, "Exploring Liquid Hydrogen Tank Technology for Zero-Emission Fuel Cell Vessels," Sandia National Laboratories, Livermore CA, USA, February , 2024 2024.

[19] Windcart, "Windcat delivers the first CTV in its new hydrogen-powered MK5 design," ed, 2024.

[20] B. T. Field, "World's First Hydrogen-based, 1.5 MW Propulsion System for Aeronautical Applications," ed, 2024.

[21] R. Thompson, U. Weichenhain, N. Sachdeva, and M. kaufmann, "Hydrogen | A future fuel for aviation?," Munich, Germany, March 2020 2020. [Online]. Available: rolandberger.com

[22] S. R. Department, "Environmental impact of the aviation industry worldwide - statistics & facts," Staistica, 16 April 2024 2024.

[23] M. Prewitz, J. Schwärzer, and A. Bardenhagen, "Potential analysis of hydrogen storage systems in aircraft design," *International Journal of Hydrogen Energy,* vol. 48, no. 65, pp. 25538-25548, 2023/07/30/ 2023, doi: https://doi.org/10.1016/j.ijhydene.2023.03.266.

[24] Airbus. At Airbus, hydrogen power gathers pace [Online] Available: https://www.airbus.com/en/newsroom/stories/2023-06-at-airbus-hydrogen-power-gathers-pace

[25] A. Andrijanovits, ""New Converter Topologies for Integration of Hydrogen Based Long-Term Energy Storages to Renewable Energy Systems," PhD, Department of Electrical Engineering, Tallinn University of Technology, 2013, 2013.

[26] S. M. Haile, "Fuel cell materials and components☆☆☆The Golden Jubilee Issue—Selected topics in Materials Science and Engineering: Past, Present and Future, edited by S. Suresh," *Acta Materialia,* vol. 51, no. 19, pp. 5981-6000, 2003/11/25/ 2003, doi: https://doi.org/10.1016/j.actamat.2003.08.004.

[27] Y. Oono, T. Fukuda, A. Sounai, and M. Hori, "Influence of operating temperature on cell performance and endurance of high temperature proton exchange membrane fuel cells," *Journal of Power Sources,* vol. 195, no. 4, pp. 1007-1014, 2010/02/15/ 2010, doi: https://doi.org/10.1016/j.jpowsour.2009.08.097.

[28] Y. Hou, J. Schall, S. Dietze, T. Kurz, and D. Gerteisen, "An experimental and numerical study of spatial and temporal catalyst degradation during start-up and shut-down of PEM fuel cells," *Journal of Power Sources,* vol. 591, p. 233780, 2024/01/30/ 2024, doi: https://doi.org/10.1016/j.jpowsour.2023.233780.

[29] F. Gao, M. Kabalo, M. Rylko, B. Blunier, and A. Miraoui, "Fuel Cell System," vol. 59, 2013, pp. 185-234.

[30] A. D. B. E. Frappé, O. Béthoux, C. Marchand, and G. Coquery, "Electrical architecture for high power segmented PEM Fuel Cell in vehicle application," 2013.

[31] A. Kolli, A. Gaillard, A. De Bernardinis, O. Bethoux, D. Hissel, and Z. Khatir, "A review on DC/DC converter architectures for power fuel cell applications," *Energy Conversion and Management,* vol. 105, pp. 716-730, 2015/11/15/ 2015, doi: https://doi.org/10.1016/j.enconman.2015.07.060.

[32] O. Krykunov, "Comparison of the DC/DC-Converters for Fuel Cell Applications," *International Journal of Electrical and Electronics Engineering,* 2007.

[33] Z. Zhang, R. Pittini, M. A. E. Andersen, and O. C. Thomsena, "A Review and Design of Power Electronics Converters for Fuel Cell Hybrid System Applications," *Energy Procedia,* vol. 20, pp. 301-310, 2012, doi: 10.1016/j.egypro.2012.03.030.

[34] D. Guilbert, A. Gaillard, A. Mohammadi, A. N'Diaye, and A. Djerdir, "Investigation of the interactions between proton exchange membrane fuel cell and interleaved DC/DC boost converter in case of power switch faults," *International Journal of Hydrogen Energy,* vol. 40, no. 1, pp. 519-537, 2015, doi: 10.1016/j.ijhydene.2014.10.072.

[35] M. Dhimish and N. Schofield, "Single-switch boost-buck DC-DC converter for industrial fuel cell and photovoltaics applications," *International Journal of Hydrogen Energy,* vol. 47, no. 2, pp. 1241-1255, 2022, doi: 10.1016/j.ijhydene.2021.10.097.

[36] D. Guilbert, A. Mohammadi, A. Gaillard, A. N'Diaye, and A. Djerdir, "Interactions between fuel cell and DC/DC converter for fuel cell electric vehicle applications: Influence of faults," presented at the IECON 2013 - 39th Annual Conference of the IEEE Industrial Electronics Society, 2013.

[37] F. Slah, A. Mansour, M. Hajer, and B. Faouzi, "Analysis, modeling and implementation of an interleaved boost DC-DC converter for fuel cell used in electric vehicle," *International Journal of Hydrogen Energy,* vol. 42, no. 48, pp. 28852-28864, 2017, doi: 10.1016/j.ijhydene.2017.08.068.

[38] X. Hao, I. Salhi, S. Laghrouche, Y. Ait-Amirat, and A. Djerdir, "Robust control of four-phase interleaved boost converter by considering the performance of PEM fuel cell current," *International Journal of Hydrogen Energy,* vol. 46, no. 78, pp. 38827-38840, 2021, doi: 10.1016/j.ijhydene.2021.09.132.

[39] J. C. Rosas-Caro *et al.*, "Fuel-cell energy generation system based on the series-capacitor boost converter," *International Journal of Hydrogen Energy,* vol. 46, no. 51, pp. 26126-26137, 2021, doi: 10.1016/j.ijhydene.2021.04.086.

[40] A. Garrigós, D. Marroquí, A. García, J. M. Blanes, and R. Gutiérrez, "Interleaved, switched-inductor, multi-phase, multi-device DC/DC boost converter for non-

isolated and high conversion ratio fuel cell applications," *International Journal of Hydrogen Energy,* vol. 44, no. 25, pp. 12783-12792, 2019, doi: 10.1016/j.ijhydene.2018.11.094.

[41] S. Furfari and A. Clerici, "Green hydrogen: the crucial performance of electrolysers fed by variable and intermittent renewable electricity," *The European Physical Journal Plus,* vol. 136, no. 5, p. 509, 2021/05/08 2021, doi: 10.1140/epjp/s13360-021-01445-5.

[42] D. Guilbert, S. M. Collura, and A. Scipioni, "DC/DC converter topologies for electrolyzers: State-of-the-art and remaining key issues," *International Journal of Hydrogen Energy,* vol. 42, no. 38, pp. 23966-23985, 2017/09/21/ 2017, doi: https://doi.org/10.1016/j.ijhydene.2017.07.174.

[43] V. A. Martinez Lopez, H. Ziar, J. W. Haverkort, M. Zeman, and O. Isabella, "Dynamic operation of water electrolyzers: A review for applications in photovoltaic systems integration," *Renewable and Sustainable Energy Reviews,* vol. 182, p. 113407, 2023/08/01/ 2023, doi: https://doi.org/10.1016/j.rser.2023.113407.

[44] M. Nasser, T. F. Megahed, S. Ookawara, and H. Hassan, "A review of water electrolysis–based systems for hydrogen production using hybrid/solar/wind energy systems," *Environmental Science and Pollution Research,* vol. 29, no. 58, pp. 86994-87018, 2022/12/01 2022, doi: 10.1007/s11356-022-23323-y.

[45] B. Yodwong, D. Guilbert, M. Phattanasak, W. Kaewmanee, M. Hinaje, and G. Vitale, "Proton Exchange Membrane Electrolyzer Modeling for Power Electronics Control: A Short Review," (in English), *Journal of Carbon Research,* 2020-05-09 2020, doi: 10.3390/c6020029.

[46] D. M. Wu, C. Peng, C. Yin, and H. Tang, "Review of System Integration and Control of Proton Exchange Membrane Fuel Cells," *Electrochemical Energy Reviews,* pp. 1-40, 2020.

[47] D. Guilbert, D. Sorbera, and G. Vitale, "A stacked interleaved DC-DC buck converter for proton exchange membrane electrolyzer applications: Design and experimental validation," *International Journal of Hydrogen Energy,* vol. 45, no. 1, pp. 64-79, 2020/1// 2020, doi: 10.1016/j.ijhydene.2019.10.238.

[48] M. V. Naik and P. Samuel, "Analysis of ripple current, power losses and high efficiency of DC–DC converters for fuel cell power generating systems," *Renewable and Sustainable Energy Reviews,* vol. 59, pp. 1080-1088, 2016/06/01/ 2016, doi: https://doi.org/10.1016/j.rser.2016.01.029.

[49] M. Kabalo, B. Blunier, D. Bouquain, and A. Miraoui, *State-of-the-art of DC-DC converters for fuel cell vehicles*. 2010, pp. 1-6.

[50] J. Yao, S. Wang, and Z. Luo, "Modeling, Analysis, and Reduction of Radiated EMI Due to the Voltage Across Input and Output Cables in an Automotive Non-Isolated Power Converter," *IEEE Transactions on Power Electronics,* vol. 37, no. 5, pp. 5455-5465, 2022, doi: 10.1109/TPEL.2021.3128628.

[51] R. S. Deshmukh, A. Shekhar, and P. Bauer, "Adaptive Modularity for Power Electronics Based Electrolysis Systems for Green Hydrogen," in *2022 IEEE 20th International Power Electronics and Motion Control Conference (PEMC)*, 25-28 Sept. 2022 2022, pp. 508-515, doi: 10.1109/PEMC51159.2022.9962941.

[52] V. Guida, D. Guilbert, and B. Douine, "Literature Survey of Interleaved DC-DC Step-Down Converters for Proton Exchange Membrane Electrolyzer Applications," *Transactions on Environment and Electrical Engineering,* vol. 3, p. 33, 03/01 2019, doi: 10.22149/teee.v3i1.129.

[53] M. E. Şahin, H. İ. Okumuş, and M. T. Aydemir, "Implementation of an electrolysis system with DC/DC synchronous buck converter," *International Journal of Hydrogen Energy,* vol. 39, no. 13, pp. 6802-6812, 2014/04/24/ 2014, doi: https://doi.org/10.1016/j.ijhydene.2014.02.084.

[54] D. Guilbert and G. Vitale, "Optimal Hydrogen Production from Direct Coupled Variable Speed Wind Generator with a Stacked Interleaved Buck converter," in *2019 IEEE International Conference on Environment and Electrical Engineering and 2019 IEEE Industrial and Commercial Power Systems Europe (EEEIC / I&CPS Europe)*, 11-14 June 2019 2019, pp. 1-6, doi: 10.1109/EEEIC.2019.8783715.

[55] A. Alkhaldi, A. Elkhateb, and D. Laverty, "Voltage Lifting Techniques for Non-Isolated DC/DC Converters," *Electronics,* vol. 12, no. 3, p. 718, 2023. [Online]. Available: https://www.mdpi.com/2079-9292/12/3/718.

[56] B. Axelrod, Y. Berkovich, and A. Ioinovici, "Switched-Capacitor/Switched-Inductor Structures for Getting Transformerless Hybrid DC–DC PWM Converters," *IEEE Transactions on Circuits and Systems I: Regular Papers,* vol. 55, no. 2, pp. 687-696, 2008, doi: 10.1109/TCSI.2008.916403.

[57] M. Kabalo, B. Blunier, D. Bouquain, and A. Miraoui, "Comparaison analysis of high voltage ratio low input current ripple floating interleaving boost converters for fuel cell applications," in *2011 IEEE Vehicle Power and Propulsion Conference*, 6-9 Sept. 2011 2011, pp. 1-6, doi: 10.1109/VPPC.2011.6043101.

[58] D. Coutellier, V. G. Agelidis, and S. Choi, "Experimental verification of floating-output interleaved-input DC-DC high-gain transformer-less converter topologies," in *2008 IEEE Power Electronics Specialists Conference*, 15-19 June 2008 2008, pp. 562-568, doi: 10.1109/PESC.2008.4591989.

[59] C.-T. Tsai, T.-C. Liang, Y.-C. Kuo, and Y.-C. Luo, "An improved forward converter with PFC and ZVS features for split-phase charger applications," *Computers & Electrical Engineering,* vol. 51, pp. 291-303, 2016/04/01/ 2016, doi: https://doi.org/10.1016/j.compeleceng.2016.01.010.

[60] M. K. M. T. Inc., "AN 1114 Switch Mode Power Supply (SMPS) Topologies (Part I)," 2007.

[61] A. K. Rathore and S. K. Mazumder, "Novel zero-current switching current-fed half-bridge isolated Dc/Dc converter for fuel cell based applications," in *2010 IEEE Energy Conversion Congress and Exposition*, 12-16 Sept. 2010 2010, pp. 3523-3529, doi: 10.1109/ECCE.2010.5617699.

[62] X. Kong, L. T. Choi, and A. M. Khambadkone, "Analysis and control of isolated current-fed full bridge converter in fuel cell system," in *30th Annual Conference of IEEE Industrial Electronics Society, 2004. IECON 2004*, 2-6 Nov. 2004 2004, vol. 3, pp. 2825-2830 Vol. 3, doi: 10.1109/IECON.2004.1432256.

[63] O. A. Ahmed and J. A. M. Bleijs, "An overview of DC–DC converter topologies for fuel cell-ultracapacitor hybrid distribution system," *Renewable and Sustainable*

Energy Reviews, vol. 42, pp. 609-626, 2015/02/01/ 2015, doi: https://doi.org/10.1016/j.rser.2014.10.067.

[64] P. Purgat, S. Bandyopadhyay, Z. Qin, and P. Bauer, "Zero Voltage Switching Criteria of Triple Active Bridge Converter," *IEEE Transactions on Power Electronics,* vol. 36, no. 5, pp. 5425-5439, 2021, doi: 10.1109/tpel.2020.3027785.

[65] H. Tao, A. Kotsopoulos, J. L. Duarte, and M. A. M. Hendrix, "Triple-Half-Bridge Bidirectional Converter Controlled by Phase Shift and PWM," 2006.

[66] A. Andrijanovits, A. Blinov, D. Vinnikov, and J. Martins, "Magnetically Coupled Multiport Converter with Integrated Energy Storage," *Przeglad Elektrotechniczny,* vol. 88, 01/01 2012.

[67] R. G.-G. Matheepot Phattanasak, J.-P. Martin., S. Pierfederici., and B. Davat, "Flatness Based control of an Isolated Three-port Bidirectional DC-DC converter for a Fuel cell hybrid source," presented at the Groupe de Recherche en Electronique et en Electrotechnique de Nancy (GREEN) Nancy-Université, INPL, 2011.

[68] C. Zhao, S. D. Round, and J. W. Kolar, "An Isolated Three-Port Bidirectional DC-DC Converter With Decoupled Power Flow Management," *IEEE Transactions on Power Electronics,* vol. 23, no. 5, pp. 2443-2453, 2008, doi: 10.1109/tpel.2008.2002056.

[69] P. Wang, X. Lu, W. Wang, and D. Xu, "Hardware Decoupling and Autonomous Control of Series-Resonance-Based Three-Port Converters in DC Microgrids," *IEEE Transactions on Industry Applications,* vol. 55, no. 4, pp. 3901-3914, 2019, doi: 10.1109/TIA.2019.2906112.

[70] P. Koohi *et al.*, "A Hardware-Based Bidirectional Power Flow Decoupling Approach for Multi-Active-Bridge Converters," in *2023 IEEE Int. Conf. Electr. Syst. Aircr. Railw. Sh. Propuls. Road Veh. Int. Transp. Electrif. Conf. ESARS-ITEC*, 29-31 March 2023 2023, pp. 1-7, doi: 10.1109/ESARS-ITEC57127.2023.10114906.

[71] M. A. Dev, K. T. H. Babu, and P. F. Beevi, "Three Mode Three-Port Isolated DC/DC Converter With Dual Fast Charging Port," in *2022 International Conference on Futuristic Technologies in Control Systems & Renewable Energy (ICFCR)*, 21-22 July 2022 2022, pp. 1-6, doi: 10.1109/ICFCR54831.2022.9893609.

[72] T. Pereira, Y. Wei, Y. Pascal, H. A. Mantooth, and M. Liserre, "Self-Tuning Multiport Resonant DC/DC Converter Based on Actively-Controlled Inductors for Hybrid Storage System Integration," *IEEE Transactions on Power Electronics,* vol. 38, no. 4, pp. 4787-4804, 2023, doi: 10.1109/TPEL.2022.3232188.

[73] X. Zhang, H. Liu, P. Wheeler, and F. Wu, "Research on Power Decoupling and Parameter Mismatch of Three-Port Isolated Resonant DC–DC Converter Applied Switch-Controlled Capacitor," *IEEE Transactions on Industrial Electronics,* vol. 70, no. 8, pp. 8098-8107, 2023, doi: 10.1109/TIE.2022.3220895.

[74] S. Dey, C. Reece, O. P. Irabor, and A. Mallik, "Comparative Analysis and Optimization of Triple Active Bridge Transformer Configuration With Integrable Leakage Inductance," *IEEE Journal of Emerging and Selected Topics in Power Electronics,* vol. 11, no. 5, pp. 5102-5119, 2023, doi: 10.1109/JESTPE.2023.3298894.

[75] S. Bandyopadhyay, P. Purgat, Z. Qin, and P. Bauer, "A Multiactive Bridge Converter With Inherently Decoupled Power Flows," *IEEE Transactions on Power Electronics,* vol. 36, no. 2, pp. 2231-2245, 2021, doi: 10.1109/tpel.2020.3006266.

[76] M. Phattanasak, R. Gavagsaz-Ghoachani, j.-p. Martin, s. Pierfederici, and B. Davat, "Flatness Based control of an Isolated Three-port Bidirectional DC-DC converter for a Fuel cell hybrid source," 09/01 2011, doi: 10.1109/ECCE.2011.6063878.

[77] Y. Cai, C. Gu, J. Li, J. Yang, G. Buticchi, and H. Zhang, "Dynamic Performance Enhancement of a Triple Active Bridge With Power Decoupling-Based Configurable Model Predictive Control," *IEEE Transactions on Transportation Electrification,* vol. 9, no. 2, pp. 3338-3349, 2023, doi: 10.1109/TTE.2022.3226471.

[78] Z. Qi, M. A. Rahman, and M. R. Islam, "Model Predictive Control for Magnetic Linked Multiport Converter," in *2022 IEEE Global Conference on Computing, Power and Communication Technologies (GlobConPT)*, 23-25 Sept. 2022 2022, pp. 1-6, doi: 10.1109/GlobConPT57482.2022.9938296.

[79] Y. Ma, K. Wu, Z. Shu, and H. Wang, "An Optimized Neural Network Based Power Decoupling Strategy for Three-Port Isolated Bidirectional DC-DC Converters," in *2023 IEEE 2nd International Power Electronics and Application Symposium (PEAS)*, 10-13 Nov. 2023 2023, pp. 2075-2080, doi: 10.1109/PEAS58692.2023.10395123.

[80] K. Wu, Y. Ma, X. Xiao, and H. Wang, "A Hybrid Power Decoupling Strategy for Triple Active Bridge," in *2024 IEEE 10th International Power Electronics and Motion Control Conference (IPEMC2024-ECCE Asia)*, 17-20 May 2024 2024, pp. 1752-1757, doi: 10.1109/IPEMC-ECCEAsia60879.2024.10567518.

[81] P. Purgat, S. Bandyopadhyay, Z. Qin, and P. Bauer, "Power Flow Decoupling Controller for Triple Active Bridge Based on Fourier Decomposition of Transformer Currents," in *2020 IEEE Applied Power Electronics Conference and Exposition (APEC)*, 15-19 March 2020 2020, pp. 1201-1208, doi: 10.1109/APEC39645.2020.9124006.

[82] V. Repecho, J. M. Olm, R. Griñó, A. Dòria-Cerezo, and E. Fossas, "Modelling and Nonlinear Control of a Magnetically Coupled Multiport DC-DC Converter for Automotive Applications," *IEEE Access,* vol. 9, pp. 63345-63355, 2021, doi: 10.1109/ACCESS.2021.3074696.

[83] S. Okutani, A. Nishi, P. Y. Huang, and Y. Kado, "Polar Coordinate Decoupling Power Flow Control for Triple Active Bridge Converter," in *2019 IEEE Third International Conference on DC Microgrids (ICDCM)*, 20-23 May 2019 2019, pp. 1-5, doi: 10.1109/ICDCM45535.2019.9232720.

[84] S. Gong *et al.*, "Sliding Mode Control-Based Decoupling Scheme for Quad-Active Bridge DC–DC Converter," *IEEE Journal of Emerging and Selected Topics in Power Electronics,* vol. 10, no. 1, pp. 1153-1164, 2022, doi: 10.1109/jestpe.2021.3096228.

[85] O. M. Hebala, A. A. Aboushady, K. H. Ahmed, and I. Abdelsalam, "Generalized Active Power Flow Controller for Multiactive Bridge DC–DC Converters With Minimum-Current-Point-Tracking Algorithm," *IEEE Transactions on Industrial Electronics,* vol. 69, no. 4, pp. 3764-3775, 2022, doi: 10.1109/tie.2021.3071681.

[86] H. Tao, A. Kotsopoulos, J. L. Duarte, and M. A. M. Hendrix, "Transformer-Coupled Multiport ZVS Bidirectional DC–DC Converter With Wide Input Range," *IEEE*

Transactions on Power Electronics, vol. 23, no. 2, pp. 771-781, 2008, doi: 10.1109/TPEL.2007.915129.

[87] K. O. Bempah, K.-W. Heo, and J.-H. Jung, "Power flow decoupling method of triple-active-bridge converter for islanding mode operation in DC microgrid systems," *Journal of Power Electronics,* vol. 23, no. 1, pp. 58-67, 2022, doi: 10.1007/s43236-022-00528-5.

[88] T. Pereira, F. Hoffmann, R. Zhu, and M. Liserre, "A Comprehensive Assessment of Multiwinding Transformer-Based DC–DC Converters," *IEEE Transactions on Power Electronics,* vol. 36, no. 9, pp. 10020-10036, 2021, doi: 10.1109/tpel.2021.3064302.

[89] H. Cao, G. Zhu, X. Li, P. Darvish, and Y. Zhao, "An Isolated Triple-Active-Bridge Converter With Highly Dynamic and Adaptive Power Decoupling Control," *IEEE Transactions on Power Electronics,* vol. 41, no. 4, pp. 5946-5961, 2026, doi: 10.1109/TPEL.2025.3620241.

[90] T. Ohno and N. Hoshi, "Current Tracking Control of Triple Active Bridge DC/DC Converter Under Varying DC-Bus Voltage Conditions," *IEEE Open Journal of Power Electronics,* vol. 3, pp. 834-845, 2022, doi: 10.1109/OJPEL.2022.3218283.

[91] H. Bai and C. Mi, "Eliminate Reactive Power and Increase System Efficiency of Isolated Bidirectional Dual-Active-Bridge DC–DC Converters Using Novel Dual-Phase-Shift Control," *IEEE Transactions on Power Electronics,* vol. 23, no. 6, pp. 2905-2914, 2008, doi: 10.1109/TPEL.2008.2005103.

[92] X. Yu, Z. Lan, J. Zeng, C. Tu, and D. He, "Time-Domain-Based Superposition Analysis for Triple Active Bridge and Its Application for ZVS and Current Stress Optimization," *IEEE Transactions on Power Electronics,* vol. 38, no. 5, pp. 5844-5857, 2023, doi: 10.1109/TPEL.2023.3237963.

[93] X. Meng *et al.*, "An Efficiency Improvement Strategy for Triple-Active-Bridge-Based DC Energy Routers in DC Microgrids," *Electronics,* vol. 13, no. 7, p. 1172, 2024. [Online]. Available: https://www.mdpi.com/2079-9292/13/7/1172.

[94] A. Chandwani and A. Mallik, "Phase-Duty Modulated Loop Decoupling and Design Optimization for a Triple Active Bridge Converter for Light Electric Vehicle Charging," *IEEE Journal of Emerging and Selected Topics in Industrial Electronics,* vol. 4, no. 1, pp. 357-367, 2023, doi: 10.1109/JESTIE.2022.3179942.

[95] J. Li, Q. Luo, T. Luo, D. Mou, and M. Liserre, "Efficiency Optimization Scheme for Isolated Triple Active Bridge DC–DC Converter With Full Soft-Switching and Minimized RMS Current," *IEEE Transactions on Power Electronics,* vol. 37, no. 8, pp. 9114-9128, 2022, doi: 10.1109/tpel.2022.3157443.

[96] Q. Wang, X. Zhao, H. Xi, S. Yan, and G. Buja, "Optimization of Reflux Power in Triple Active Bridge with Online Particle Swarm Optimization and Exponential Weighted Moving Average Algorithm," *IEEE Journal of Emerging and Selected Topics in Power Electronics,* pp. 1-1, 2024, doi: 10.1109/JESTPE.2024.3368445.

[97] A. A. Ibrahim, A. Zilio, T. Younis, D. Biadene, T. Caldognetto, and P. Mattavelli, "Optimal Modulation of Triple Active Bridge Converters by an Artificial-Neural-Network Approach," *IEEE Transactions on Industrial Electronics,* vol. 71, no. 3, pp. 2590-2600, 2024, doi: 10.1109/TIE.2023.3270529.

[98] A. A. Ibrahim, A. Zilio, T. Younis, D. Biadene, T. Caldognetto, and P. Mattavelli, "Artificial Neural Networks Approach for Reduced RMS Currents in Triple Active Bridge Converters," in *IECON 2022 – 48th Annual Conference of the IEEE Industrial Electronics Society*, 17-20 Oct. 2022 2022, pp. 1-6, doi: 10.1109/IECON49645.2022.9968804.

[99] A. A. Ibrahim, A. Zilio, D. Biadene, T. Caldognetto, and P. Mattavelli, "Optimization Approaches for RMS Current Reduction of Triple Active Bridge Converters," in *2023 IEEE Conference on Power Electronics and Renewable Energy (CPERE)*, 19-21 Feb. 2023 2023, pp. 1-7, doi: 10.1109/CPERE56564.2023.10119543.

[100] S. Dey, A. Mallik, C. Darmody, and A. Akturk, "Online Optimization of Decision Control Variables Ensuring Loss-Minima Tracking in a TAB-based DC-AC-DC Switching Network," *IEEE Journal of Emerging and Selected Topics in Industrial Electronics,* vol. PP, pp. 1-14, 01/01 2023, doi: 10.1109/JESTIE.2023.3327050.

[101] S. Rahman, I. Khan, S. Dey, and A. Mallik, "Triple-Active Bridge-based Dynamic Power Balancing Solution for Minimizing Overdesigning in Military Aircraft Power System," *IEEE Transactions on Vehicular Technology,* pp. 1-11, 2023, doi: 10.1109/TVT.2023.3323538.

[102] B. Zhao, Q. Song, W. Liu, and Y. Sun, "Overview of dual-active-bridge isolated bidirectional DC-DC converter for high-frequency-link power-conversion system," *IEEE Transactions on Power Electronics,* vol. 29, no. 8, pp. 4091-4106, 2014, doi: 10.1109/TPEL.2013.2289913.

[103] J.-H. Han and I.-S. Kim, "The Controller Design of the Bi-directional Three Level Converter," presented at the 2022 11th International Conference on Renewable Energy Research and Application (ICRERA), 2022.

[104] B. Zhao, Q. Song, and W. Liu, "Power characterization of isolated bidirectional dual-active-bridge dc-dc converter with dual-phase-shift control," *IEEE Transactions on Power Electronics,* vol. 27, no. 9, pp. 4172-4176, 2012, doi: 10.1109/TPEL.2012.2189586.

[105] R. W. A. A. D. Doncker, D. M. Divan, and M. H. Kheraluwala, "A three-phase soft-switched high-power-density DC/DC converter for high-power applications," *IEEE Transactions on Industry Applications,* vol. 27, no. 1, pp. 63-73, 1991, doi: 10.1109/28.67533.

[106] K. Suzuki, S. Iyasu, Y. Hayashi, and Y. Handa, "Continuous Power Transfer Control of Triple Active Bridge Converter during Magnetic Saturation," presented at the 2022 11th International Conference on Renewable Energy Research and Application (ICRERA), 2022.

[107] K. Nishimoto, Y. Kado, and K. Wada, "Implementation of Decoupling Power Flow Control System in Triple Active Bridge Converter Rated at 400V, 10kW, and 20kHz," *IEEJ Journal of Industry Applications,* vol. 7, no. 5, pp. 410-415, 2018, doi: 10.1541/ieejjia.7.410.

[108] X. Qi and Y. Bai, "Improved Linear Active Disturbance Rejection Control for Microgrid Frequency Regulation," *Energies,* vol. 10, no. 7, p. 1047, 2017. [Online]. Available: https://www.mdpi.com/1996-1073/10/7/1047.

[109] L. Liu, S. Tian, D. Xue, T. Zhang, Y. Chen, and S. Zhang, "A Review of Industrial MIMO Decoupling Control," *International Journal of Control, Automation and Systems,* vol. 17, no. 5, pp. 1246-1254, 2019, doi: 10.1007/s12555-018-0367-4.

[110] H. L. Wade, "Inverted decoupling a neglected technique," *ISA Transactions,* vol. 36, no. 1, pp. 3-10, 1997.

[111] D. Vinnikov, A. Andrijanovitš, I. Roasto, and T. Lehtla, "New integrated converter for hydrogen buffer interfacing in distributed energy systems," *Renewable Energy and Power Quality Journal,* pp. 998-1003, 2011, doi: 10.24084/repqj09.525.

[112] D. U. Kim, B. Byen, B. Jeong, and S. Kim, "Design of Triple-Active Bridge Converter with Inherently Decoupled Power Flows," in *2022 24th European Conference on Power Electronics and Applications (EPE'22 ECCE Europe)*, 5-9 Sept. 2022 2022, pp. 1-9.

[113] G. Buticchi, A. Farjudian, J. Oh, and L. Tarisciotti, "An ANN-Assisted Control for the Power Decoupling of a Multiple Active Bridge DC-DC Converter," in *IECON 2022 – 48th Annual Conference of the IEEE Industrial Electronics Society*, 17-20 Oct. 2022 2022, pp. 1-6, doi: 10.1109/IECON49645.2022.9968534.

[114] J. M. Olm, E. Fossas, V. Repecho, A. Dória-Cerezo, and R. Griñó, "Feedback linearizing control of a magnetically coupled multiport dc-dc converter for automotive applications," in *IECON 2019 - 45th Annual Conference of the IEEE Industrial Electronics Society*, 14-17 Oct. 2019 2019, vol. 1, pp. 2688-2692, doi: 10.1109/IECON.2019.8927831.

[115] I. Biswas, D. Kastha, and P. Bajpai, "Small Signal Modeling and Decoupled Controller Design for a Triple Active Bridge Multiport DC–DC Converter," *IEEE Transactions on Power Electronics,* vol. 36, no. 2, pp. 1856-1869, 2021, doi: 10.1109/tpel.2020.3006782.

[116] O. E. Oyewole and K. H. Ahmed, "Comparative Analysis of Decoupling Control Methods for Multiport-Isolated Bidirectional DC-DC Converter with Hydrogen Storage System Integration," presented at the 2023 11th International Conference on Smart Grid (icSmartGrid), 2023.

[117] A. H. A. Adam *et al.*, "Power Decoupling Enhancement of a Triple Active Bridge Converter With Feedforward Compensation Based on Model Predictive Control and Fuzzy Logic Controller in DC Microgrid Systems," *IEEE Access,* vol. 12, pp. 140310-140328, 2024, doi: 10.1109/ACCESS.2024.3469815.

[118] G. Buticchi, L. F. Costa, D. Barater, M. Liserre, and E. D. Amarillo, "A Quadruple Active Bridge Converter for the Storage Integration on the More Electric Aircraft," *IEEE Transactions on Power Electronics,* vol. 33, no. 9, pp. 8174-8186, 2018, doi: 10.1109/TPEL.2017.2781258.

[119] K. Zhao, J. Zhang, D. Ma, and Y. Xia, "Composite Disturbance Rejection Attitude Control for Quadrotor With Unknown Disturbance," *IEEE Transactions on Industrial Electronics,* vol. 67, no. 8, pp. 6894-6903, 2020, doi: 10.1109/TIE.2019.2937065.

[120] J. Han, "From PID to Active Disturbance Rejection Control," *IEEE Transactions on Industrial Electronics,* vol. 56, no. 3, pp. 900-906, 2009, doi: 10.1109/TIE.2008.2011621.

[121] R. Wang, B. Hu, S. Sun, F. Man, Z. Yu, and Q. Chen, "Linear Active Disturbance Rejection Control for DC Side Voltage of Single-Phase Active Power Filters," *IEEE Access,* vol. 7, pp. 73095-73105, 2019, doi: 10.1109/ACCESS.2019.2920626.

[122] H. He, T. Si, L. Sun, B. Liu, and Z. Li, "Linear Active Disturbance Rejection Control for Three-Phase Voltage-Source PWM Rectifier," *IEEE Access,* vol. 8, pp. 45050-45060, 2020, doi: 10.1109/ACCESS.2020.2978579.

[123] S. Zhou, X. Guo, R. Zhang, R. Wang, and C. Li, "Research on Triple Interleaved Bidirectional DC/DC Converter Based on Second-Order Linear Active Disturbance Rejection," *IEEE Journal of Emerging and Selected Topics in Industrial Electronics,* vol. 4, no. 4, pp. 1074-1083, 2023, doi: 10.1109/JESTIE.2023.3306997.

[124] J. Yang, H. Cui, S. Li, and A. Zolotas, "Optimized Active Disturbance Rejection Control for DC-DC Buck Converters With Uncertainties Using a Reduced-Order GPI Observer," *IEEE Transactions on Circuits and Systems I: Regular Papers,* vol. 65, no. 2, pp. 832-841, 2018, doi: 10.1109/TCSI.2017.2725386.

[125] K. Łakomy *et al.*, "Active Disturbance Rejection Control Design With Suppression of Sensor Noise Effects in Application to DC–DC Buck Power Converter," *IEEE Transactions on Industrial Electronics,* vol. 69, no. 1, pp. 816-824, 2022, doi: 10.1109/TIE.2021.3055187.

[126] H. Bai, D. Yang, J. Song, Q. Su, B. Duan, and C. Zhang, "Linear Active Disturbance Rejection Control of LLC Resonant Converters for EV Chargers," in *2020 Chinese Automation Congress (CAC)*, 6-8 Nov. 2020 2020, pp. 993-998, doi: 10.1109/CAC51589.2020.9327865.

[127] X. Li, S. Zhan, F. Guo, H. Liao, and Z. Zhuang, "Linear Active Disturbance Rejection Control of Dual Active Bridge Converter for Portable Energy Storage System," in *2023 5th International Conference on Power and Energy Technology (ICPET)*, 27-30 July 2023 2023, pp. 35-39, doi: 10.1109/ICPET59380.2023.10367687.

[128] B. V. Martínez, J. Sanchis, S. García-Nieto, and M. Martínez, "Active disturbance rejection control: a guide for design and application," *Ibero-American Magazine of Industrial Automation and Informatics* vol. 18, no. 3, pp. 201-217, 07/01 2021, doi: 10.4995/riai.2020.14058.

[129] W. Tan and C. Fu, "Linear Active Disturbance-Rejection Control: Analysis and Tuning via IMC," *IEEE Transactions on Industrial Electronics,* vol. 63, no. 4, pp. 2350-2359, 2016, doi: 10.1109/TIE.2015.2505668.

[130] T. He, Z. Wu, D. Li, and J. Wang, "A Tuning Method of Active Disturbance Rejection Control for a Class of High-Order Processes," *IEEE Transactions on Industrial Electronics,* vol. PP, 04/12 2019, doi: 10.1109/TIE.2019.2908592.

[131] W. Cui, W. Tan, D. Li, Y. Wang, and S. Wang, "A Relay Feedback Method for the Tuning of Linear Active Disturbance Rejection Controllers," *IEEE Access,* vol. 8, pp. 4542-4550, 2020, doi: 10.1109/ACCESS.2019.2963419.

[132] S. Bandyopadhyay, Z. Qin, and P. Bauer, "Decoupling Control of Multiactive Bridge Converters Using Linear Active Disturbance Rejection," *IEEE Transactions on Industrial Electronics,* vol. 68, no. 11, pp. 10688-10698, 2021, doi: 10.1109/tie.2020.3031531.

[133] Z. Gao, *Scaling and Parameterization Based Controller Tuning*. 2003, pp. 4989-4996.

[134] J. Vincent *et al.*, "On active disturbance rejection based control design for superconducting RF cavities," *Nuclear Instruments and Methods in Physics Research Section A: Accelerators, Spectrometers, Detectors and Associated Equipment,* vol. 643, no. 1, pp. 11-16, 2011/07/01/ 2011, doi: https://doi.org/10.1016/j.nima.2011.04.033.

[135] D. Yoo, S. S. T. Yau, and Z. Gao, "Optimal fast tracking observer bandwidth of the linear extended state observer," *International Journal of Control,* vol. 80, no. 1, pp. 102-111, 2007/01/01 2007, doi: 10.1080/00207170600936555.

[136] B. V. Martínez, J. Sanchis, S. García-Nieto, and M. Martínez, "Tuning Rules for Active Disturbance Rejection Controllers via Multiobjective Optimization—A Guide for Parameters Computation Based on Robustness," *Mathematics,* vol. 9, no. 5, p. 517, 2021. [Online]. Available: https://www.mdpi.com/2227-7390/9/5/517.

[137] B. Ferragud and F. Xavier, "Predictive control based on models using heuristic optimization techniques. Application to nonlinear and multivariable processes," Universitat Politècnica de València, Valencia (Spain), 1999. [Online]. Available: https://riunet.upv.es/handle/10251/15995

[138] H. Rania, "A comparison of particle swarm optimization and the genetic algorithm," in *46th AIAA/ASME/ASCE/AHS/ASC Structure, Structural Dynamics and Materials Conference, Austin, TX, Genetic Algorithm, April 18-21, 2005*, 2005.

[139] F. D. Wihartiko, H. Wijayanti, and F. Virgantari, "Performance comparison of genetic algorithms and particle swarm optimization for model integer programming bus timetabling problem," *IOP Conference Series: Materials Science and Engineering,* vol. 332, no. 1, p. 012020, 2018/03/01 2018, doi: 10.1088/1757-899X/332/1/012020.

[140] R. Eberhart and J. Kennedy, "A new optimizer using particle swarm theory," in *MHS'95. Proceedings of the Sixth International Symposium on Micro Machine and Human Science*, 4-6 Oct. 1995 1995, pp. 39-43, doi: 10.1109/MHS.1995.494215.

[141] Y. d. Valle, G. K. Venayagamoorthy, S. Mohagheghi, J.-C. Hernandez, and R. G. Harley, "Particle Swarm Optimization: Basic Concepts, Variants and Applications in Power Systems," *IEEE Transactions on Evolutionary Computation,* vol. 12, pp. 171-195, 2008.

[142] V. Roberge, M. Tarbouchi, and G. Labonte, "Comparison of Parallel Genetic Algorithm and Particle Swarm Optimization for Real-Time UAV Path Planning," *IEEE Transactions on Industrial Informatics,* vol. 9, no. 1, pp. 132-141, 2013, doi: 10.1109/TII.2012.2198665.

[143] O. E. Oyewole, A. A. Abdelaziz, I. A. Jimoh, E. Bari, and K. H. Ahmed, "Optimised linear active disturbance rejection control of multiport-isolated DC-DC converter for hydrogen energy storage system integration," *Alexandria Engineering Journal,* vol. 102, pp. 159-168, 2024/09/01/ 2024, doi: https://doi.org/10.1016/j.aej.2024.05.107.

[144] S. Zou, Lu, J., & Khaligh, A, "Modelling and control of a triple-active-bridge converter," *IET Power Electronics,* vol. 13, no. 5, pp. 961-969, 2020, doi: doi.org/10.1049/iet-pel.2019.0920.

[145] B. V. Martínez, J. Sanchis, S. García-Nieto, and M. Martínez, "Active disturbance rejection control: a guide for design and application," *Ibero-American Magazine of Industrial Automation and Informatics,* vol. 18, no. 3, pp. 201-217, 07/01 2021, doi: 10.4995/riai.2020.14058.

[146] K. H. Ahmed, A. M. Massoud, S. J. Finney, and B. W. Williams, "A Modified Stationary Reference Frame-Based Predictive Current Control With Zero Steady-State Error for LCL Coupled Inverter-Based Distributed Generation Systems," *IEEE Transactions on Industrial Electronics,* vol. 58, no. 4, pp. 1359-1370, 2011, doi: 10.1109/TIE.2010.2050414.

[147] G. F.Franklin, J. D. Powell, and A. Emami-Naeini, *Feedback Control of Dynamic Systems Sixth Edition Gene*, 6th Edition ed. London: Pearson Higher Education, 2010.

[148] A. Wintrich, U. Nicolai, W. Tursky, and T. Reimann, Eds. *Application Manual Power Semiconductors*. Germany: SEMIKRON International GmbH, 2015, p. 464.